PONTIFICIA UNIVERSIDAD CATOLICA DE CHILE
SCHOOL OF ENGINEERING

EFFECTS OF TOPOGRAPHY AND BASINS ON SEISMIC WAVE AMPLIFICATION: THE NORTHERN CHILE COASTAL CLIFF AND INTRA-MOUNTAINOUS BASINS

TIAREN GARCÍA PÉREZ

Thesis submitted to the Office of Graduate Studies in partial fulfillment of the requirements for the Degree of Doctor in Engineering Sciences

Advisor:
GONZALO YÁÑEZ

Santiago, Chile, December, 2020

PONTIFICIA UNIVERSIDAD CATOLICA DE CHILE
SCHOOL OF ENGINEERING

EFFECTS OF TOPOGRAPHY AND BASINS ON SEISMIC WAVE AMPLIFICATION: THE NORTHERN CHILE COASTAL CLIFF AND INTRA-MOUNTAINOUS BASINS

TIAREN GARCÍA PÉREZ

Members of the Committee:

GONZALO YÁÑEZ

ANA MG FERREIRA

JOSÉ CEMBRANO

FELIPE LEYTON

DANIEL HURTADO

GUSTAVO LAGOS

Thesis submitted to the Office of Graduate Studies in partial fulfillment of the requirements for the Degree Doctor in Engineering Science

Santiago, Chile, December, 2020.

Dedicated to Robin

Ohana

AGRADECIMIENTOS

Esta tesis representa un largo e importante viaje en mi vida, el cual no habría sido posible sin la ayuda, el apoyo y generosidad de muchas personas.

Primero quisiera agradecer a Gonzalo Yáñez, por aceptarme como su estudiante y apoyarme incansablemente durante este trabajo. Gonzalo me enseñó muchas cosas, pero sobre todo me mostró que el trabajo debe ser algo que uno disfruta hacer y que es bueno terminar las cosas que uno empieza. Gonzalo, agradezco infinitamente la paciencia con la cual me guiaste durante esta tesis y la confianza que depositaste en mi trabajo, gracias por permitirme tomarme el tiempo necesario para resolver los desafíos de esta investigación.

I wish to thank Ana MG Ferreira, for receiving me as her student at UCL and welcoming me into her research group. Ana always understood my ever-changing situation, giving me the space to struggle through life challenges and kindly pushing me when I need it. I feel so honored to have the privilege of working with you Ana, you are one of the scientists I admire the most.

Estoy tan agradecida de José Cembrano, no solo por su inmenso aporte a mi trabajo doctoral y por todas sus enseñanzas relacionadas con la geología, la ciencia y la filosofía, si no por ser la persona que me invitó a formar parte del grupo de geociencias. Muchas gracias José por verme, por creer que había algo especial en mí y cambiar mi vida. Estoy segura de que nuestra amistad perdurará a lo largo de nuestras vidas.

Quiero agradecer también a los miembros de la comisión por aceptar ser parte de este trabajo y sus importantes aportes a esta tesis. Muchas gracias a Felipe Leyton por su amabilidad y generosidad al responder cada una de las miles de dudas sobre la red sismológica de Chile que iban surgiendo durante este trabajo y ayudarme a obtener los datos que necesitaba, además por sus cálidas palabras de aliento cada vez que no topábamos en algún congreso. Muchas gracias a Daniel Hurtado por mostrarme el mundo de los elementos finitos, sus clases y enseñanzas fueron muy valiosas,

permitiéndome enfrentar los desafíos de la modelación numérica sin morir en el intento. Muchas gracias a Gustavo Lagos por ser el presidente de esta comisión y por sus aportes a este trabajo.

Es importante para mí agradecer a Gloria Arancibia por su amistad y cariño, por compartir sus conocimientos conmigo cuando las geociencias eran algo nuevo para mí y por mostrarme que las mujeres poderosas existen. Gloria, para mí y estoy segura de que para muchas más, eres un ejemplo a seguir, sobre todo por tu fortaleza, perseverancia, inteligencia y tenacidad. Lamento que nuestras líneas de investigación no hayan interactuado directamente durante mi trabajo de tesis, pero espero que en futuro podamos colaborar más activamente.

Me gustaría agradecer especialmente a Isabel Santibáñez, por ser mi entrañable amiga y compañera durante este largo camino. Muchas gracias por tu amistad, generosidad y alegría. Definitivamente tú hiciste que este doctorado fuera mucho menos difícil, haciendo que desde el inicio, nuestras colaboraciones científicas estuvieran llenas de risas y anécdotas. Soy una afortunada por tenerte en mi vida.

De igual forma, quiero agradecer a Mariel Castillo por compartir conmigo su infinita sabiduría y por ser una guía espiritual en mi vida. Mariel me acogió dentro del grupo de geociencias, ayudándome a no sentirme ajena a esta disciplina cuando recién comenzaban mis estudios de geofísica. Mariel tu eres una persona clave en el grupo de geociencias, manteniéndonos unidos y sosteniendo el espíritu de colaboración que nos caracteriza. Sin ti, nuestro querido grupo de geociencias no sería el espacio de respeto y compañerismo que es y muchas de las cosas que hacemos, no serían posible. Muchas gracias.

Me gustaría agradecer a Carlos Marquardt, Rodrigo Gomila y Pablo Iturrieta por su colaboración en las dos publicaciones que nacieron de este trabajo. Carlos y Rodrigo, muchas gracias por compartir conmigo sus conocimientos de geomorfología y geología estructural y por nuestras fructíferas discusiones sobre la geología de Iquique. Pablo, muchas gracias por ayudarme en la

modelación numérica, la visualización de la propagación de ondas en nuestros modelos y por tu amistad sincera. Ha sido un placer trabajar con ustedes.

También me gustaría agradecer a todos quienes que me acompañaron a terreno durante las campañas de recolección de datos en Iquique: José Maringue, Nicolás Pérez, Elías Lira, Álvaro Muñoz, Luis Astudillo, Camilo Rojas y Víctor Duarte. Las aventuras que vivimos juntos son de los recuerdos más lindos de este doctorado. Además quiero agradecer especialmente a José, Nicolás y Álvaro, por ayudarme en el procesamiento de los datos recolectados. Además quiero agradecer Sergio León Ríos y Pablo Salazar, quienes generosamente compartieron datos geofísicos, los cuales fueron un aporte invaluable en este trabajo.

Quiero agradecer en especial a Tomás Roquer y Pablo Iturrieta, por las innumerables tardes de conversaciones y discusiones sobre ciencia y la vida. Espero que nuestra amistad perdure, sin importar lo lejos que estemos o el tiempo que pase.

Igualmente, me gustaría reconocer la importancia que ha tenido en mi desarrollo como geocientista al grupo de geociencias y a todas las personas que lo componen, con quienes he compartido numerosas charlas, seminarios, congresos e interesantes discusiones, las cuales sin duda han forjado mi pensamiento crítico. El apoyo de este grupo de investigación ha sido fundamental en mi carrera.

I would also like to thank Rebecca Pearson, Antoniette Grima and Elodie Kendall for welcoming me at UCL and being my friends in London, I feel so lucky to meet all of you and I am sure we will always keep on eye on each other lives. Thanks to Michael Frietsch and Lewis Schardong for their invaluable help when I was struggling with SPECFEM (I do not know what would be of me without you guys) and your friendship during my time in London. I wish to thank to Tom Mitchell, John Browning and the Seismological Laboratory group of UCL for the fruitful and joyful conversations at SeismoCoffee and the kindness of everyone in the UCL Earth Science Department. My time at UCL is one of the most wonderful and rewarding experiences of my life.

También, me gustaría agradecer a mis amigos del alma, Víctor Duarte, María Oyarzún, Franco Tapia, Antonella Rescaglio, Mariana Rescaglio, Romina Cataldo y Pamela Pizarro por acompañarme en esta vida, llenándola de risas y alegrías y apoyándome emocionalmente durante este largo proceso. También quiero agradecer a Viviana Zúñiga, Saskia Roels, Carolina Milad, Bárbara Meneses y María-Jesús Fuentes por convertirse en mis amigas durante estos últimos años, mientras trabajamos en SRK, interesándose genuinamente en este trabajo y alentándome diariamente. El apoyo de Beatriz Labarca ha sido fundamental en estos últimos 3 años, quien me ha brindado un sinfín de facilidades para conciliar mi trabajo en SRK con la finalización de mi tesis doctoral y me ha animado a ello.

Por último, quiero agradecer a mi madre y hermana, Carolina Pérez y Vanya García, quienes con su amor y cuidado han apoyado cada una mis decisiones durante toda mi vida. Y por supuesto, agradecer a Robin Wylie, quién ha sido mi infatigable compañero, mi editor soñado y mi fiel aliado.

Este trabajo doctoral ha sido financiado por la Beca de Doctorado Nacional CONICYT 21130082, los trabajos de terreno realizados en Iquique fueron parcialmente financiados por el proyecto Fondef Mas Andes D10I1027 y el Centro para la Gestión Integrada de Desastres, CIGIDEN.

TABLE OF CONTENTS

LIST OF TABLES

LIST OF FIGURES

ABSTRACT

During earthquakes, structural damage is often related to soil conditions. Following the 01 April 2014 Mw 8.1 Iquique earthquake in Northern Chile, damage to infrastructure was reported in the cities of Iquique and Alto Hospicio and clear evidence of site amplification was recorded in various seismic stations located in the area.

In this study, I investigate the causes of site amplification in the Iquique region by numerically analyzing the effects of topography and basins on synthetics waveforms in the frequency range 0.1 – 3.5 Hz using the spectral element method.

The results show that topography produces changes in the amplitude of the seismic waves recorded by stations located in steep areas such as the ca. 1 km-high coastal cliff, a remarkable geomorphological feature that runs north–south, that is, parallel to the coast and the trench. The modeling also shows that secondary waves—probably related to reflected waves produced in the coastal cliff—propagate inland and offshore, augmenting the duration of the ground motion and the energy of the waveforms by up to a factor of three.

Additionally, the results show that, as expected, sedimentary basins have a considerable effect on ground motion amplification at stations located within basins and in the surrounding areas. This can be attributed to the generation of multiple reflected waves in the basins, which increase both the amplitude and the duration of the ground motion, with an amplification factor of up to 3.9 for frequencies between 2 and 3.5 Hz.

Comparisons show a good agreement in the frequency range between 0.1 and 0.5 Hz. However, for frequencies higher than 1 Hz, the fit between real and synthetic seismic waveforms progressively deteriorates, especially for stations located in or near to steep topography and basin areas. The poor data misfit at high frequencies is most likely due to the effects of small-scale 3D velocity heterogeneities, which is not yet resolved in seismic images of our study region.

Finally, the main conclusion of this work is that the interaction between the local basins and topography produces important amplification of seismic ground motion and may be the cause of the site effects observed in the cities of Alto Hospicio and Iquique during the 01 April 2014 Mw 8.1 earthquake.

Keywords: Earthquake, Topography, Basins, Site Effects, Spectral Method, 3D Numerical Computation

RESUMEN

Durante la ocurrencia de terremotos, el daño a las estructuras esta frecuentemente relacionado a las condiciones del suelo de fundación. Luego del terremoto de Iquique del 01 de abril con magnitud de momento Mw 8,1 ocurrido en el Norte de Chile, daños a las infraestructuras fueron reportados en las ciudades de Iquique y Alto Hospicio y claras evidencias de amplificación sísmica fueron observadas en los registros de estaciones sismológicas del área.

En este estudio, se investigan las causas de los efectos de sitio en la región de Iquique mediante el análisis de los efectos de la topografía y cuencas en las formas de ondas sintéticas, para rangos de frecuencias entre 0,1 y 3.5 Hz, utilizando el método de elementos espectrales.

Los resultados de esta investigación muestran que la topografía produce cambios en la amplitud de las ondas sísmicas registradas por estaciones ubicadas en áreas con altas pendientes, tales como el acantilado costero, un importante rasgo geomorfológico de aproximadamente 1 km de altura que corre de norte a sur paralelo a la costa del norte de Chile. Los resultados de la modelación también muestran que ondas secundarias—probablemente relacionadas a ondas reflejadas generadas por el acantilado costero—se propagan hacia ambos lados del acantilado costero, aumentando la duración del movimiento del suelo y la energía de las formas de ondas hasta tres veces.

Adicionalmente, los resultados muestran que las cuencas sedimentarias tienen un efecto considerable en la amplificación del movimiento del suelo para las estaciones ubicadas en la superficie de estas y en áreas adyacentes. Este efecto de amplificación puede ser atribuido a la generación de múltiples ondas reflejas en los bordes de las cuencas, las cuales aumentan tanto la amplitud como la duración del movimiento del suelo, con factores de amplificación de hasta 3,9 veces para rangos de frecuencias entre 2 y 3,5 Hz.

La comparación entre formas de ondas reales y sintéticas muestra buena concordancia para rangos de frecuencias entre 0,1 y 0,5 Hz. Sin embargo, para frecuencias por sobre 1 Hz, el ajuste entre las

formas de ondas reales y sintéticas se deteriora progresivamente, especialmente para aquellas estaciones ubicadas en o cerca de topografías pronunciadas o cuencas. La pobre correspondencia entre los datos sintéticos y reales para altas frecuencias se debe, posiblemente, a heterogeneidades 3D en las velocidades de propagación de onda a pequeñas escalas, las cuales aún no son resueltas por estudios sísmicos en la región de estudios.

Finalmente, en este trabajo se concluye que la interacción entre topografía y cuencas locales produce importante amplificación sísmica y que podría ser la causa de los efectos de sitios observados en las ciudades de Iquique y Alto Hospicio durante el terremoto de magnitud de momento Mw 8,1 ocurrido el 01 de Abril de 2014.

Palabras Claves: Terremotos, Topografía, Cuencas, Efectos de Sitio, Elementos Espectrales, Computación Numérica 3-D.

1. INTRODUCTION

Site effects during earthquakes are widely studied as they often lead to structural damage and casualties in large cities. In recent decades, significant efforts have been made to evaluate site effects through experimental and theoretical methods (e.g., Aki, 1993; Geli et al., 1988b; Sánchez-Sesma et al., 2002). Commonly, experimental studies are based on data from seismometers that are geometrically arranged to investigate a geomorphological feature of interest, such as surface geology, basins, faults, or slopes. Likewise, theoretical studies involving numerical methods have been performed in recent decades as advances in computational power and storage have allowed the calculation of seismic wave propagation using different mathematical approaches (e.g., finite difference, finite element, boundary methods), thereby providing increasingly complex earth models. However, disagreements between experimental and numerical studies are often reported.

For example, several studies have shown that records of severe damage and strong ground motion can match seismic amplification zones near the top and/or the slopes of topographic irregularities or near sedimentary basins (Borcherdt & Glassmoyer, 1992; Bouckovalas & Kouretzis, 2001; Buech et al., 2010; Burjánek et al., 2014; Campillo et al., 1989; Celebi, 1987; Hough et al., 2010; Massa et al., 2010; Singh et al., 1988). In general, these studies observed amplifications in seismic waves whose wavelengths are comparable to the width of mountains and the thickness of basins, and also observed strong frequency dependency in the degree of amplification. Early numerical studies focused on the incidence of plane waves on simple layered features and found that topographic and geological features can have significant frequency-dependent effects on seismic waves, ranging from amplification to deamplification at given sites (Ashford et al., 1997; Bouchon, 1973; Faccioli, 1991; Geli et al., 1988b; Pedersen et al., 1994; Sánchez-Sesma & Campillo, 1993).

However, the numerical calculations performed in these studies typically did not reproduce the full complexity of the real data. This led researchers to turn their attention to the implementation of advanced numerical modeling techniques (Álvarez-Rubio et al., 2004; M Bouchon et al., 1996; Fan et al., 2014; Komatitsch & Vilotte, 1998; Lee et al., 2009; Miksat et al., 2010; Paolucci, 2002; Paolucci & Morstabilini, 2006; Restrepo et al., 2016). In the last 20 years, the spectral element method (SEM) has been widely and successfully implemented to simulate seismic wave propagation in 3-D earth models. It is a highly accurate technique which can account for complex topographic surfaces and internal discontinuities, and sedimentary basin features (e.g., Komatitsch et al., 2004; Komatitsch & Tromp, 1999; Lee et al., 2009). However, despite several studies investigating the effects of topography and complex geology on seismic waves, the poor knowledge of the geometry and mechanical properties of subsoil materials and the lack of extensive comparisons with real data still limit the understanding of site effects.

Due to the convergence between the Nazca and the South American plates, Chile is one of the most seismically active regions in world, capable of produces large magnitudes earthquakes (e.g., Mw 9.5 Valdivia, 1960; Mw 8.8 Maule, 2010) with time recurrence estimated between 80 to 120 years (>Mw 7.5) (Barrientos & Ward, 1990; D. Comte et al., 1986; Lomnitz, 2004). After the 2010 Mw 8.8 Maule earthquake, Chile began an important program for the deployment of modern real-time network of digital broadband, strong-motion and GPS stations to better prepare for future and expected large earthquakes (Barrientos, 2018). In particular the seismic network coverage of Northern Chile has substantially improved in recent decades, with the expansion of both permanent and temporary networks (Barrientos, 2018). Therefore, high-quality seismic data have been available for the last decade, including for the 01 April 2014 Mw 8.1 Iquique earthquake in Northern Chile.

These high-quality seismic data provide an excellent opportunity to investigate the causes of the site effects that were produced by this earthquake in the cities of Iquique and Alto Hospicio, and can notably be used to study the interaction between topography, soil properties, and seismic waves using numerical techniques such as the spectral element method.

The 01 April 2014 Mw 8.1 Iquique earthquake was a megathrust event and its epicenter was located in the widely known Northern Chile seismic gap. This seismic gap covers the area between 19 and 21°S, where the last two major earthquakes occurred in 1868 and 1877, both of which had a magnitude of Mw 8.8 (Diana Comte & Pardo, 1991). Despite the large magnitude of the 2014 Iquique earthquake, its slip was constrained to a relatively small area, and therefore the potential for a large event in the Northern Chile seismic gap still remains, given that over 70% of the length of the gap has not experienced a large earthquake since 1868, as shown in **Figure 1** (Bürgmann, 2014; Gavin P. Hayes et al., 2014; Lay et al., 2014; Ruiz et al., 2014).

Figure 1: Topographic map of Northern Chile showing the Iquique earthquake sequence and the main geomorphological units of the emerged forearc. The red beach balls represent the focal mechanisms of the foreshock, mainshock, and the main aftershock events, as obtained from the Global CMT catalogue (Dziewonski et al., 1981). The red dots are the relocated seismicity from March to July 2014 as obtained from León-Ríos et al. (2016). The black rectangle shows the study area. Dark red shaded polygons represent rupture areas of historical earthquakes.

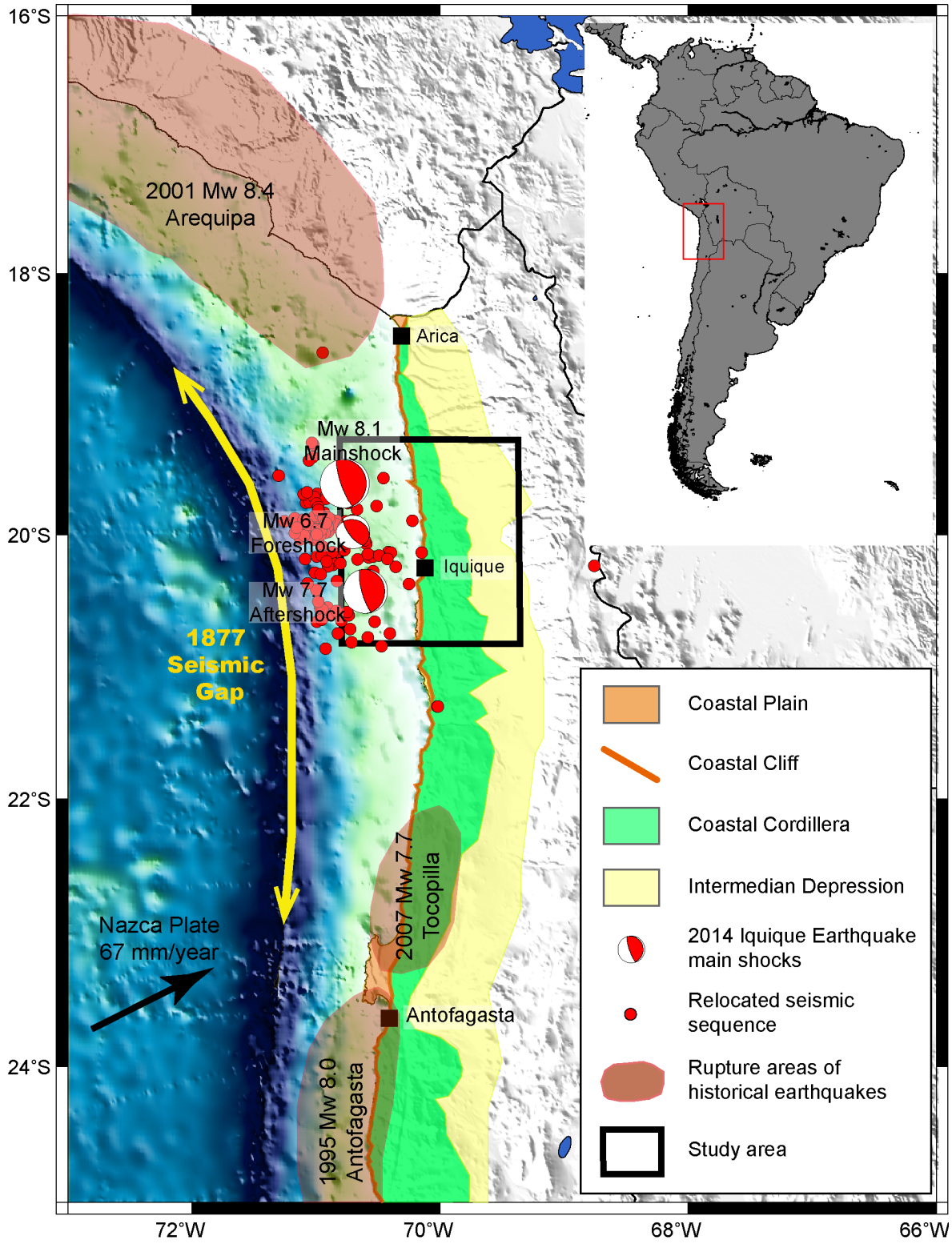
16°S
18°S
20°S
22°S
24°S
72°W
70°W
68°W
66°W
2001 Mw 8.4
Arequipa
Arica
Mw 8.1
Mainshock
Mw 6.7
Foreshock
Mw 7.7
Aftershock
Iquique
1877
Seismic
Gap
Nazca Plate
67 mm/year
2007 Mw 7.7
Tocopilla
Antofagasta
1995 Mw 8.0
Antofagasta
Coastal Plain
Coastal Cliff
Coastal Cordillera
Intermedian Depression
2014 Iquique Earthquake
main shocks
Relocated seismic
sequence
Rupture areas of
historical earthquakes
Study area

Northern Chile presents remarkable geomorphological features in the emerged forearc due to the combined effect of a hyper-arid climate and plate convergence (Allmendinger & González, 2010; González et al., 2003; Niemeyer et al., 1996), as shown in **Figure 1**. These features include several intra-mountainous basins deposited in the Coastal Cordillera—an eroded mountain range with a length of 3000 km—the Coastal Cliff—a steeply sloping cliff with an average height of 1000 m—the Coastal Plains—several marine terraces that extend between the coast line and the Coastal Cliff—and the Central Depression, a large sedimentary basin generated by forearc movements and the uplift of the Andes (Farías et al., 2005; Hartley & Evenstar, 2010; Jordan et al., 2010; Marquardt et al., 2004; Martinod et al., 2016; Paskoff, 1978; Tolorza et al., 2009). Several works suggest that Neogene activity of forearc crustal faults, linked to the local subduction seismic cycle, controls the geomorphology of the Coastal Plain, the Costal Cordillera, and the western limit of the Central Depression in Northern Chile (Allmendinger et al., 2005; Allmendinger & González, 2010; Cembrano et al., 2005; González et al., 2003, 2008, 2015).

Iquique and the neighboring city of Alto Hospicio, are both located in this geomorphologically extraordinary region and presented extensive damage on buildings and structures during the 2014 Iquique earthquake (Becerra et al., 2015, 2016). The observed damage in Iquique was mostly distributed in poor quality soil, agreeing with previous local soils geophysical characterization, although the damage occurred in Alto Hospicio cannot be explained by the aforementioned classification (Becerra et al., 2016). Therefore, considering the geomorphological conditions given in the region, the initial hypothesis for this study is that the Coastal Cliff, with remarkable characteristics in the Iquique area, played an important role in the observed site effects, representing a major seismic hazard in the region.

Given the potential of a large-magnitude earthquake occurring in Northern Chile in the next decades, as well as the particular geomorphological features present in the area and the high-

quality seismic data that were recorded during the Iquique earthquake, in this study, I analyzed the potential causes of the site effects that were observed at Iquique and Alto Hospicio during the Iquique earthquake by simulating seismic wave propagation using the spectral element method (SEM). In this way, I first investigate the geological, geometrical, and physical properties of the Alto Hospicio and Pampa del Tamarugal basins, and then explore the effects of topography and sedimentary basins on the waveforms by using a 3-D numerical model of the region, performing comparisons of the simulated and observed waveforms. This allowed me to identify the likely causes of the observed seismic amplifications in the region during the 2014 Iquique earthquake, as well as the wider implications of the results.

As part of this investigation, two publications were written. The published article *"Insights on the structural control of a Neogene forearc basin in Northern Chile: A geophysical approach"* (García-Pérez et al., 2018), shows a comprehensive study of the Alto Hospicio basin through the analyses of geophysical and geological data, defining the geometry of the basin and discussing the nature and evolution of the upper crustal deformation during Neogene and Quaternary. The article in revision *"Effects of topography and basins on seismic wave amplification: the Northern Chile Coastal Cliff and Intra-mountainous basins"*, shows the numerical study that analyses the effects of topography and basins on seismic waves propagation in the frequency range 0.1 – 3.5 Hz using the spectral element method, comparing synthetic and observed data for two earthquakes of the Mw 8.1 Iquique earthquake sequence.

This thesis is organized as follows: Section 2 describes the tectonic, geological, and geomorphological framework of the study region, as well as the Iquique earthquake and the evidence of site effects; Section 3 presents the geophysical and geological constraints of the study area, in which the section 3.1 synthesized the main findings of the first published article of this work; Section 4 describes the implementation of the SEM model; Section 5 describes the

results of the modeling; Section 6 presents a comparison of the synthetic (modeled) seismic waveforms and the real data; Section 7 presents a discussion; and Section 8 presents the conclusions. Sections 4, 5, 6, 7 and 8 correspond to the detailed investigation presented in the second article.

1.1. OBJECTIVES

The main objective of this work is to understand the effects of the topography and basins on the amplification of seismic waves during an earthquake in order to offer possible explanations for the site affects observed in Iquique and Alto Hospicio during the 2014 Iquique earthquake.

The specific objectives of this work are:

- To understand the contribution of the topography in the amplification of seismic waves compared with a flat earth.
- To understand the effects produced by different size basins and the basin's edges on the seismic wave's propagation.
- To quantify the amplification in the seismic waves produced by the combination of topography and basin effects.
- To observe the effects on the seismic wave propagation produced by the Coastal Cliff and the Alto Hospicio and Pampa del Tamarugal basins during earthquakes.

1.2. METODOLOGIES

In order to accomplish the main objective proposed, simulations of the seismic waveforms assuming known earthquakes using the Spectral Element Method (SEM) were computed, by using the next methodologies:

- To determine the physical properties of the medium in which the simulated waves propagate that properly represent the crustal and subsurface materials in the study area, such as the crustal velocity structure, topography and basins geometries, geophysical surveys, geological studies and an extensive literature review were performed.

- To understand the effects produced by extreme topographies and different size basins on the propagation of seismic waves during an earthquake, a numerical modeling using the spectral element method was implemented.

- To analyze the effects on the synthetic waveforms produced by the topography and basins four numerical models were built: flat 1D velocity model, 1D velocity model with topography, 1D velocity model with topography and basins and 2D velocity model with topography.

- The comparison of the numerical models allowed quantifying the amplification due to topography and basins and observing the effects of the Coastal Cliff and the Alto Hospicio and Pampa del Tamarugal basins.

2. TECTONIC AND GEOLOGICAL FRAMEWORK

The convergence between the Nazca and South American plates is characterized by the subduction of the oceanic Nazca plate beneath the continental South American plate at a velocity of approximately ~65 mm/year (Kendrick et al., 2003). This convergence has produced one of the largest positive topographic features on earth, namely the Andes mountain belt. The Andes were built by complex processes associated with magmatic and tectonic activity since the Oligocene (e.g. Hervé et al., 1987; Oncken et al., 2006; Ramos, 2009). The northern section of the Central Andes, defined as the section between 15 and 23°S and described as the Altiplano segment by Tassara & Yáñez (2003), is limited to the north by the Nazca Ridge and to the south by the Mejillones Peninsula, and is characterized by a subduction angle of ~30° with a slab length of 550 km (Allmendinger et al., 2005). This segment, together with the Puna segment to the south, constitute the Altiplano-Puna region (15–28°S), which covers an area with a width of 400 km and a length of 1800 km, has elevations above ~3000 m and peaks that rise to ~6000 m, and where the uplift of the topographic highlands and the forearc are produced by the interplay between the hyper-arid climate and first-order processes such as the erosive margin, the seismic cycle, and the construction of volcanic edifices (e.g. Allmendinger & González, 2010; Garzione et al., 2008; Jordan et al., 2010; Lamb & Davis, 2003).

The forearc in the Altiplano segment is characterized by deformation induced by the plate convergence, in which a strong plate-coupling, probably related to the lack of sediments in the trench due to the hyper-arid climate, extends from depths of 20 to ~50 km (Allmendinger & González, 2010). The maximum depth of the seismic coupling is located below the coastline, implying that the coastal uplift is probably connected to the crustal shortening and thickening driven by thrusting along the plate boundary (Allmendinger et al., 2005a; González et al., 2003). Therefore, the Coastal Cordillera of Northern Chile emerges in the study area, as a long-term

preserved feature in which geological evidences of the tectonic process generated by the convergence between the Nazca and the South American plates are preserved due to the hyper-arid climate of the region (Allmendinger & González, 2010; Cembrano et al., 2005; González et al., 2003).

2.1. GEOMORPHOLOGICAL AND GEOLOGICAL SETTINGS

The major geomorphological features present in the study area are the Coastal Cordillera, the Coastal Cliff, the Coastal Plain, and the Central Depression (**Figure 1**). The Coastal Cordillera is an eroded Jurassic–Early Cretaceous volcanic arc with altitudes between 1000 and 2000 m a.s.l. and an average width of 30 km. This feature runs parallel to the trench and is limited to the west by the Coastal Cliff and to the east by the Central Depression (Scheuber and González, 1999; González et al., 2003). Within the Coastal Cordillera, alluvial sediments cover half-graben basins formed by N to NE-striking extensional crustal faults which were developed by Late Cenozoic deformation parallel to the continental margin and younger alluvial drainages preserved as pediment surfaces (García-Pérez et al., 2018; Marquardt et al., 2008).

The Coastal Cliff is an abrupt scarp, with slopes of about ~45°, descending directly into the sea or to the Coastal Plain. The origin of the Coastal Cliff remains controversial, however, available hypotheses suggest that it was developed by a combination of two main processes: (1) the action of vertical west-dipping normal faults with changing dip along the subduction interface, that lift the Coastal Cordillera due to inverse stack duplex; and (2) marine erosion produced by sea-level changes during the Pliocene (Mortimer and Rendic, 1975; Paskoff, 1978; Armijo and Thiele, 1990; Von Huene et al., 1999; Quezada et al., 2010; Contreras-Reyes et al., 2012; Armijo et al., 2015). In the Iquique area, the age of ashes ($^{40}Ar/^{39}Ar$) located at the upper levels of the Coastal Cliff is estimated at 2.77±0.03 and 5.8±0.16 Ma, representing the minimum age of the Coastal Cliff uplift (Tolorza et al., 2009).

The Coastal Plain is a narrow flat surface composed of a series of marine abrasion terraces located between the coastline and the Coastal Cliff, and has an average lateral extension of 3 km. The Coastal Plain has been preserved by the extremely arid climate of the region. These marine abrasion terraces have emerged from the Middle Pleistocene to the present as a result of sea-level changes and tectonic uplift linked to the seismic cycle (Ortlieb et al., 1996; Marquardt et al., 2004).

The Central Depression of Northern Chile is a N-S trending topographic low located between the Coastal Cordillera and the Precordillera. This feature has a width of 25 to 100 km and extends between ~18° and 22°S, with average elevations of 1000 and 2000 m in the west and east, respectively. The Central Depression was formed as a basin due to transtensional and extensional faulting during the Cenozoic and is filled with more than 1000 m of Tertiary–Quaternary alluvial fan and fluvial and lacustrine deposits with inter-bedded volcanic ash (Jordan et al., 2001, 2010).

The geological units that form the geomorphological features in the study area **(Figure 2)** are diverse and have a wide range of ages from Jurassic to Quaternary. The rock units that compose the Coastal Cordillera are stratified rocks, including Cretaceous and Jurassic volcano-sedimentary rocks and Jurassic marine sedimentary rocks, and intrusive rocks emplaced during the Jurassic and Early Cretaceous, mainly granites, granodiorites, and andesitic porphyry (Marquardt et al., 2008; Vásquez & Sepúlveda, 2013). Oligocene–Miocene deposits related to sequences of consolidated sandstones and gravels with inter-bedded volcanic ash are deposited in structural basins in the Coastal Cordillera and Central Depression formed by Cenozoic faulting (García-Pérez et al., 2018; Jordan et al., 2001; Vásquez & Sepúlveda, 2013). Lastly, Pliocene–Holocene deposits composed of eolian, colluvial, and littoral and alluvial non-consolidated sediments (gravels, sands, and silts) are accumulated in marine terraces (Marquardt et al., 2004). These marine deposits are emplaced at the feet of the abrupt slopes formed by the Coastal Cliff,

interspersed and covering the rocks in the Coastal Plain, the Coastal Cordillera, and the Central Depression.

Further details regarding the geomorphology and geology at the specific study areas are presented in the forthcoming sections.

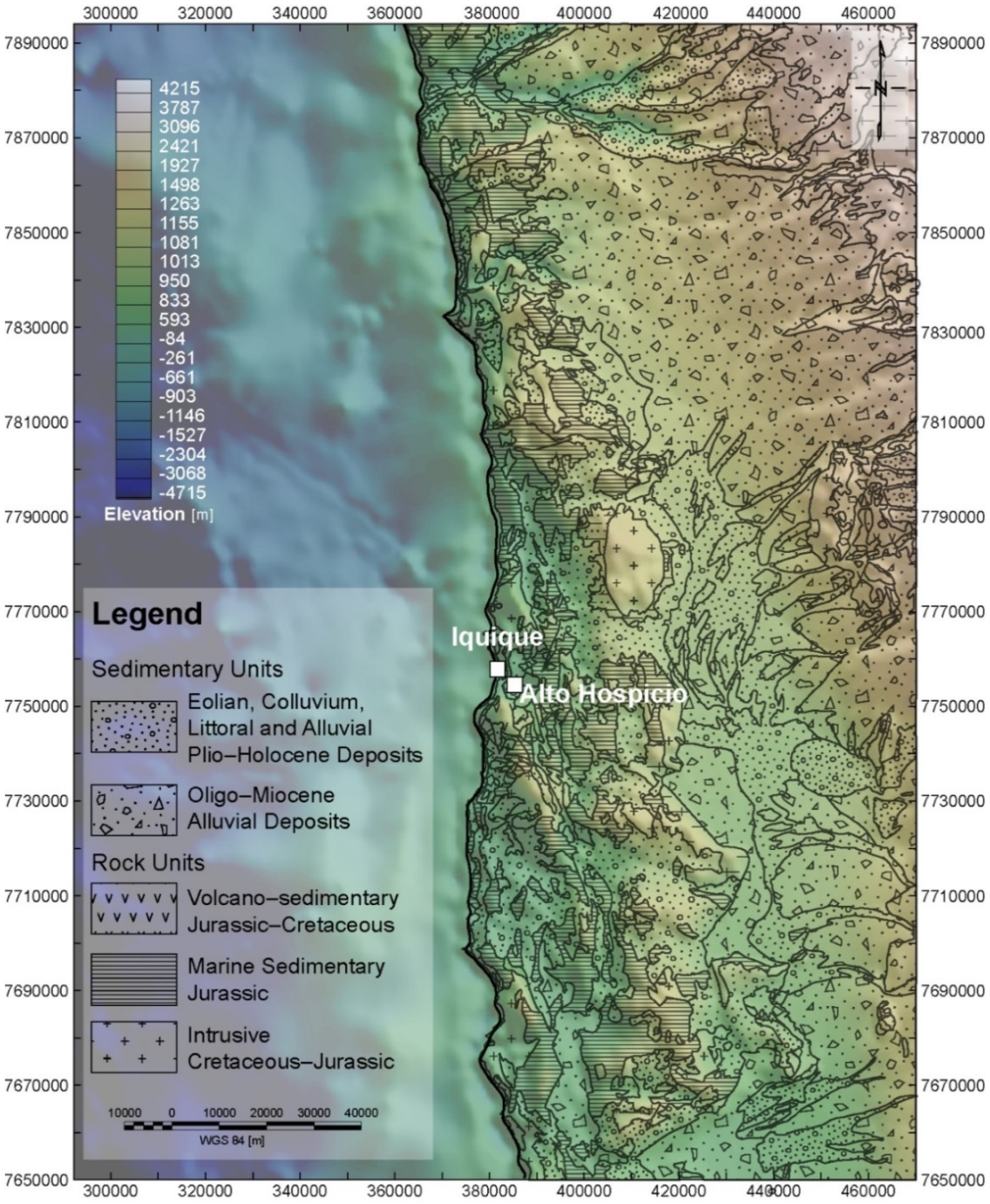

Figure 2: Geological map of the study area, modified from SERNAGEOMIN (2003), over a topography color grid Datum WGS 84, UTM 19S. The map shows the sedimentary and rocks unit's distribution and in white squares the location of Iquique and Alto Hospicio cities.

2.2. THE IQUIQUE EARTHQUAKE

As shown in **Figure 1**, the 01 April 2014 Iquique earthquake occurred in part of the well-known Northern Chile seismic gap, an extensive area where the last reported megathrust earthquakes took place in 1877 for which cumulative energy and coupling has been reported by several works (Chlieh et al., 2004, 2011; Métois et al., 2013), which indicates potential seismic hazard in the area. The Iquique earthquake was an Mw 8.1 thrust event that included intense foreshock and aftershock activity, with over 150 earthquakes larger than Mw 4.0, distributed in an area of approximately 150 by 50 km^2 between Pisagua and Punta Patache **(Figure 3)**.

A major Mw 6.7 crustal foreshock earthquake occurred on 16 March 2014 on a reverse fault located in the upper South American Plate oriented 128°/68°W. This foreshock triggered two weeks of migrating activity of 3.5 km/day toward the hypocenter of the Iquique earthquake (González et al., 2015). Studies suggest that such margin-oblique reverse faults accommodate N-S shortening resulting from the convergence vector angle and the curvature of the margin at the Arica bend (Allmendinger et al., 2005a; Carrizo et al., 2008), and the slip on one of these structures may have unclamped the subduction interface, and probably triggered the Iquique earthquake itself (Bouchon et al., 2016; González et al., 2015; Hayes et al., 2014).

The vigorous and long sequence of aftershocks lasted for over three months and included the Mw 7.7 event on 03 April 2018. The analysis of the regional moment tensors of the aftershock sequence indicate that many of the aftershock earthquakes had shallow hypocenters and focal mechanisms that are inconsistent with thrust faulting or nodal planes that were severely rotated with respect to the local slab structure, these results reflects the seismic interaction between plate interface earthquakes and upper-plate earthquakes (Hayes et al., 2014; León-Ríos et al., 2016).

The finite fault-plane solution for the mainshock indicates a rupture area in the deeper part of the seismogenic zone, with the hypocenter at depths of ~30–40 km and a slip of up to 8 m, with the

slip extending only ~50 km along the interface from the hypocenter, describing a very compact rupture area considering the size of the earthquake (Hayes et al., 2014) and the extent of the seismic gap in this tectonic segment.

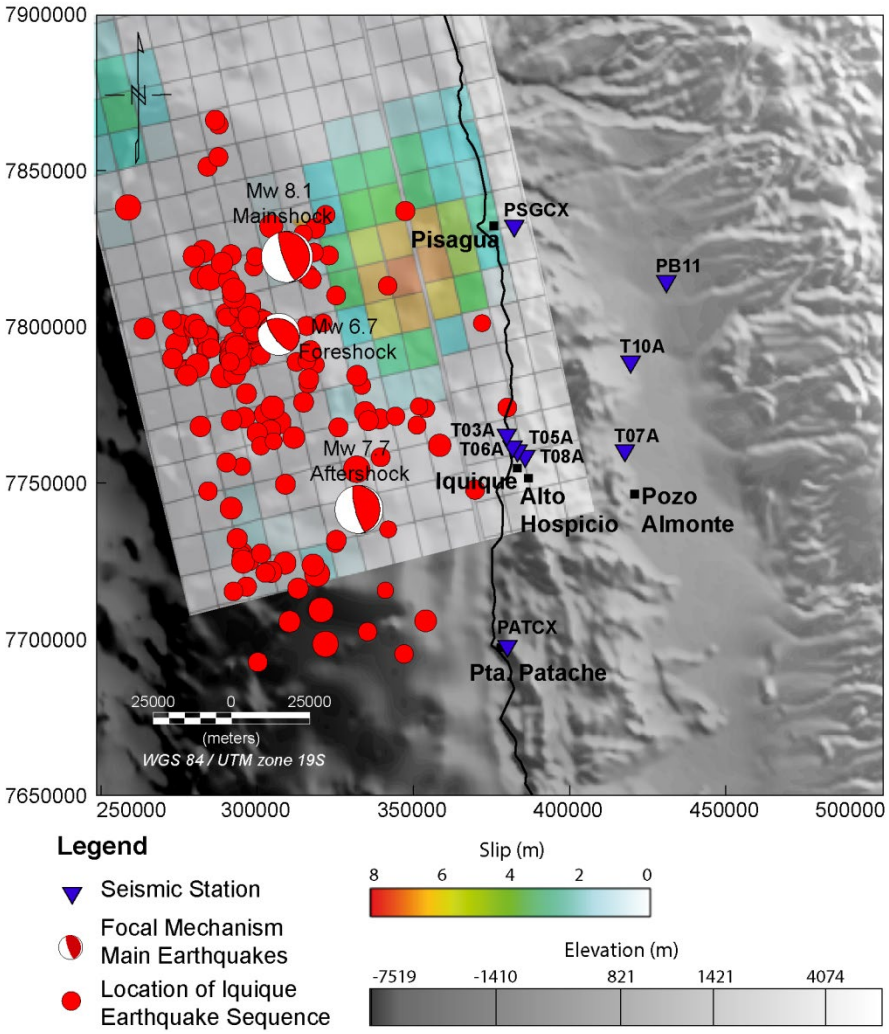

Figure 3: Locations of events in the Iquique earthquake sequence (red circles; León-Ríos et al., 2016) and focal mechanisms of the foreshock, aftershock, and mainshock sized by magnitude, and the surface projection of the slip distribution (Hayes et al., 2017) over a gray shaded topographic grid Datum WGS 84, UTM 19S. Blue inverted triangles indicate the locations of the seismic stations used in this study and black squares indicate the main locations in the study area.

2.2.1. EVIDENCE OF SITE EFFECTS

Before the Iquique earthquake, due to the existing extensive seismic gap in Northern Chile, various efforts were made to prepare for an expected large damaging earthquake. The identification of the seismic hazards in urban domains and the deployment of a large number of seismic stations represent important attempts to better estimate the seismic risk in this area.

Seismic microzonation is a commonly used tool for the assessment of potential ground motion amplification effects during earthquakes. Therefore, studies involving the identification of areas with high potential seismic hazard using geophysical techniques were conducted in several cities in Northern Chile, including Iquique and Alto Hospicio. The studies performed in these two cities, the results of which were reported by Becerra et al. (2015), analyzed the mechanical behavior of soils using surface wave methods, classifying the soils into zones with similar mechanical properties based on the geophysical survey, borehole information, and the geological background.

During the last decade, the Chilean National Seismological Center (CSN in Spanish), has installed a large number (65) of permanent real-time broadband and strong motion seismic stations in the Chilean territory (Barrientos, 2018). Additionally, the Integrated Plate Boundary Observatory of Chile (IPOC), which is dedicated to studying the seismic cycle and associated deformation in the continental margin, has deployed a distributed system of instruments (Geosciences & CNRS-INSU, 2006) which is operated by a consortium of academic institutions (GFZ German Research Centre for Geosciences, the Institute de Physique du Globe de Paris (IPGP), the CSN, the Universidad de Chile (UCH), and the Universidad Católica del Norte (UCN)). Both of these networks registered the Iquique earthquake sequence, providing an excellent opportunity for the study of site effects through the analysis of the available data. The

details of the seismic stations in the CSN and IPOC networks located in the study area that were used for this work are presented in **Table 1**, and their locations are shown in **Figure 3.**

Table 1: Details of the seismic stations used in this study.

Station Id	Lat (°S)	Lon (°W)	Elevation (m a.s.l.)	Instrument type	Sampling rate (s^{-1})
T01A	20.273	70.122	223	Kinemetrics Episensor FBA	200
T03A	20.230	70.146	11	Kinemetrics Episensor FBA	200
T05A	20.210	70.150	31	Kinemetrics Episensor FBA	200
T06A	20.214	70.138	33	Kinemetrics Episensor FBA	200
T07A	20.256	69.786	1049	Kinemetrics Episensor FBA	200
T08A	20.270	70.094	536	Kinemetrics Episensor FBA	200
T10A	19.995	69.767	1007	Kinemetrics Episensor FBA	200
PSGCX	19.600	70.120	970	Streckeisen STS2	100
PB11	19.760	69.990	1400	Streckeisen STS2	100
PATCX	20.820	70.150	805	Streckeisen STS2	100

According to Becerra et al. (2016), the damage observed during the Iquique earthquake in urban areas mainly affected low masonry structures, with the spatial distribution of the damage agreeing relatively well with the expected local soil behavior determined from geophysical characterization. However, some site effects cannot be directly related to the soil condition (Becerra et al., 2016). To fully address this situation, in the following sub-sections, detailed evidence of the site effects produced during the Iquique earthquake is provided.

2.2.1.1. DAMAGE DISTRIBUTION AND SEISMIC MICROZONATION

A seismic microzonation study was conducted in the cities of Iquique and Alto Hospicio to identify the seismic hazard related to the soil conditions, whose accuracy was soon tested when the Iquique earthquake occurred (Becerra et al., 2015). These adjacent cities (Iquique is located in the Coastal Plain between the coastline and the Coastal Cliff, and Alto Hospicio is located in the Coastal Cordillera next to the Coastal Cliff; **Figure 4**) were the locations that were most affected by the earthquake.

The seismic microzonation reported by Becerra et al. (2015) was developed by the evaluation of the dynamic properties of soils using standard geophysical and geological surveys, including the harmonic average of the shear wave velocity for a depth of 30 m (V_s^{30}) (Humire et al., 2015; Park et al., 1999; Park & Miller, 2008) and the predominant frequency F_0 obtained from the horizontal-to-vertical spectral ratio HVSR analysis (Lermo & Chávez-García, 1993; F. Leyton et al., 2013), and well as by the analysis of borehole logs and the surface geology. Overall, the results of the geophysical and geological analysis show that the soil conditions in Iquique present considerable variations, while those of Alto Hospicio are quite homogeneous. The seismic microzonation of Becerra et al. (2015), shown in **Figure 4**, is a subdivision of areas with similar dynamic soil properties; the colors represent the expected ground motion amplification, with green indicating low expected amplification and red indicating high expected amplification.

According to the data reported by Becerra et al. (2016), significant damage, shown by black circles in **Figure 4**, was produced during the Iquique earthquake in low-period structures such as houses and warehouses. As shown in **Figure 4**, in Iquique City, the damage mainly occurred in the northern and eastern zones, approximately coinciding with the areas of moderately-high to high expected amplification defined in the seismic microzonation, while in Alto Hospicio,

the damage was evenly distributed, showing no correlation with the soil classification obtained in the seismic microzonation.

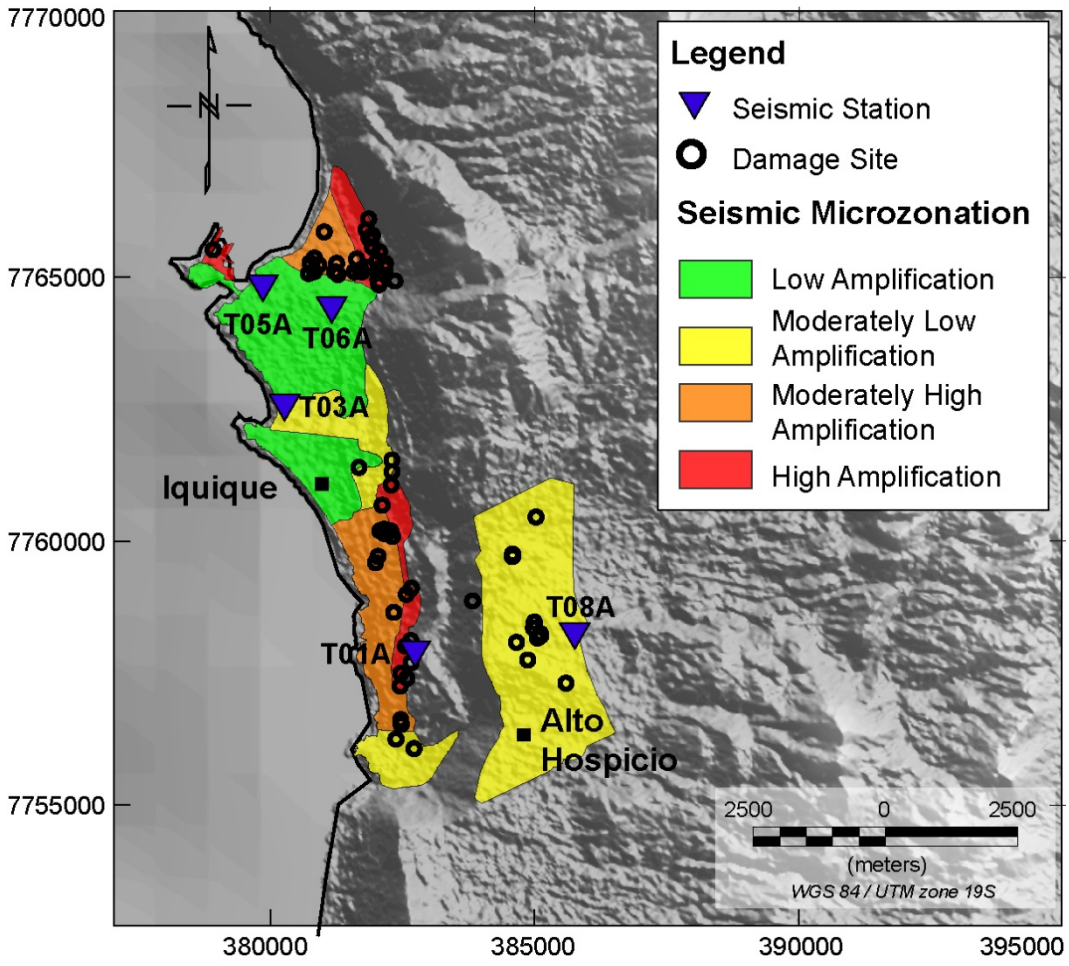

Figure 4: Seismic microzonation and the distribution of damage produced by the Iquique earthquake in the cities of Iquique and Alto Hospicio, over a gray shaded topographic grid map datum WGS 84, UTM 19S (Modified from Becerra et al., 2015, 2016). Colored areas indicate the expected ground motion amplification, with green representing low expected amplifications and red high expected amplification and black circle indicating the damage occurred during the 2014 Iquique earthquake and the blue triangles indicate the location of the available seismic stations.

It is important to remark that both the damage distribution and the areas of moderately-high to high expected amplification are restricted to narrow zones in the Coastal Plain where the soils

are composed of sediments associated with the abrupt slopes formed by the Coastal Cliff. This observation highlights the role of the Coastal Cliff as a geomorphological agent, and its possible influence on the damage observed in Iquique and Alto Hospicio cannot be neglected. However, the existence of cavities and saline soils which were not detected by the geophysical techniques may also represent a possible source of the non-expected damage in Alto Hospicio.

2.2.1.2. SEISMIC DATA

A complementary way to observe site effects is through the examination of seismic data. In this section, an analysis of the three-component waveforms generated by the 2014 Iquique earthquake, as recorded by the CSN and IPOC seismic networks, is presented. The CSN data are local accelerations recorded by triaxial surface accelerometers located in Iquique and Alto Hospicio, while the IPOC data were obtained from broadband triaxial seismometers widely distributed along the Coastal Cordillera, as detailed in **Table 1**. The two types of waveforms were corrected for the instrument response and the mean and trend were removed. The horizontal component waveforms were rotated into longitudinal (R) and transverse (T) directions to allow amplitude comparison between the different stations. The data were filtered using a Butterworth bandpass filter of order 2 with four poles from 0.1 to 20 Hz.

The lower panel of **Figure 5** shows the processed acceleration waveforms for the stations T03A, T05A, T06, T08A, and T07A, as well as the respective epicentral distances, whereas the upper panel shows the locations of the seismic stations and the Iquique earthquake. Stations T03A, T05A, and T06 are located in Iquique City in the coastal plain, while station T08A is located in Alto Hospicio City in the Coastal Cordillera, approximately 500 m from the coastal cliff. Finally, station T07A is located close to Pozo Almonte Town in the Pampa del Tamarugal basin at the limit between the Coastal Cordillera and the Central Depression.

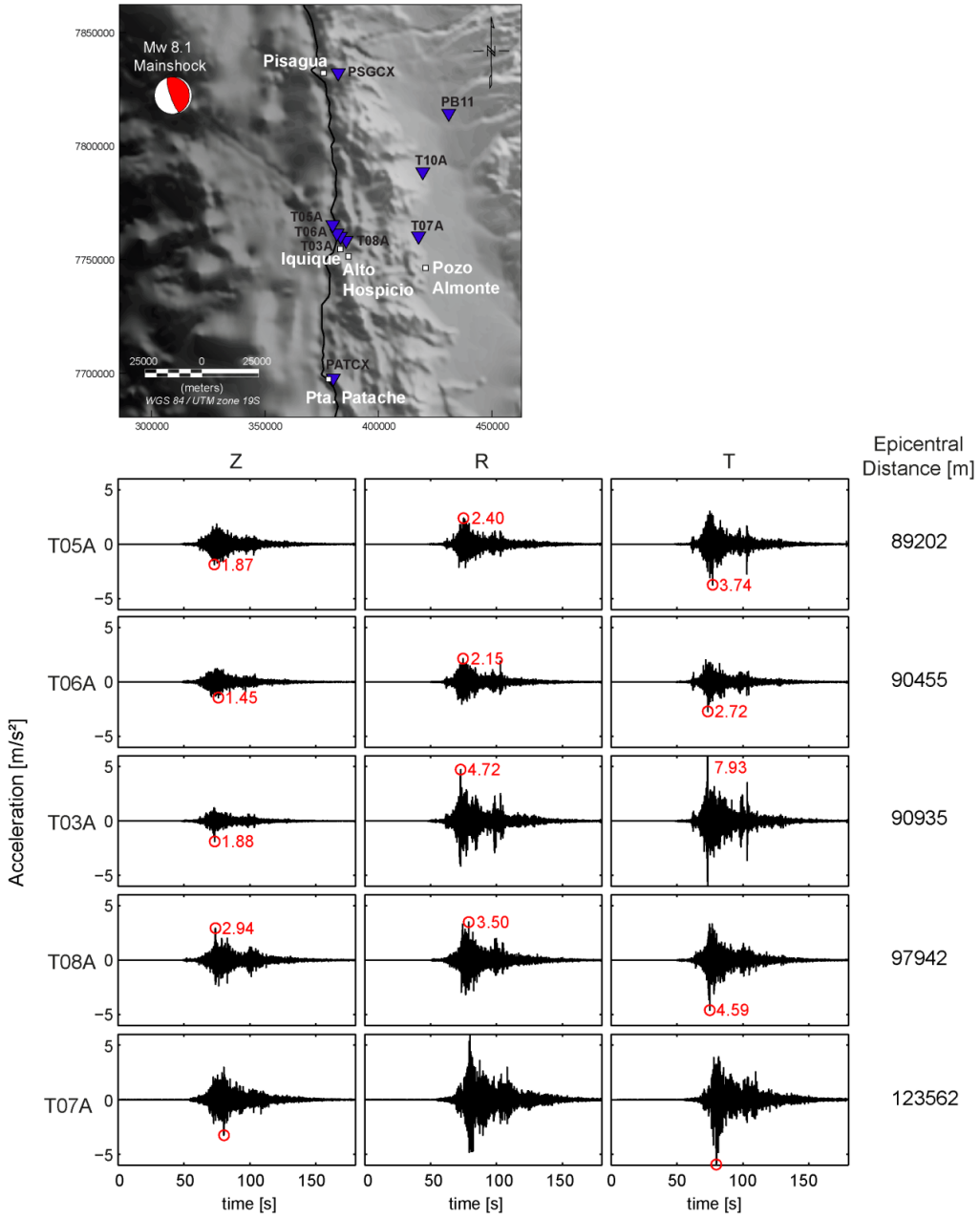

Figure 5: Upper Panel: Locations of the April 2014 Mw 8.1 Iquique earthquake and seismic stations. Lower Panel: Local three-component acceleration waveforms for the Iquique earthquake showing evidence for site effects at five seismic stations (the locations of the stations are shown in Figures 3 and 4). The waveforms are filtered using a Butterworth bandpass filter of order 2 with four poles from 0.1 to 20 Hz. The vertical (Z, left), radial (R, middle), and transverse (T, right) components for the five stations are shown using the same horizontal and vertical scales. The red circles represent the maximum peak value for each trace, whose magnitude is also annotated in red.

The waveforms at stations T03A, T08A, and T07A present larger peaks compared to stations T05A and T06A, notably in the horizontal component (T & R components), the latter two of which have the shortest epicentral distances from the earthquake. Given that these stations are located either in sedimentary soils (T03A), the vicinity of the coastal cliff (T08A), or in a basin (T08A and T07A); this indicates that the ground motion amplification observed during the Iquique earthquake may be related to the soil conditions and/or to the presence of the coastal cliff.

In the same way, **Figure 6** shows the processed displacement waveforms for stations PSGCX, PB11, and PATCX in the lower panel, and the locations of the seismic stations and the Iquique earthquake in the upper panel. Stations PSGCX and PATCX are both located in the Coastal Cordillera, although station PATCX is closer to the coastal cliff. Meanwhile, station PB11 is located in the Pampa del Tamarugal basin in the Central Depression.

The waveforms at station PATCX present the largest peaks in the vertical (Z) and transverse (T) components despite this station being the farthest station from the earthquake and extremely close to the coastal cliff. Station PB11 also shows slight amplification in the radial (R) component; this may be related to the Pampa del Tamarugal basin, since this station is the only one that is located in the interior of this basin. Although other factors, such as source and directivity effects (which are outside of the scope of this thesis), may produce differences in the amplitudes of the seismic waves at different stations, the fact that a clear correlation is observed between seismic amplification and soil condition, proximity to the coastal cliff, and location within basins, suggests that these three factors are major contributors to the observed seismic amplification.

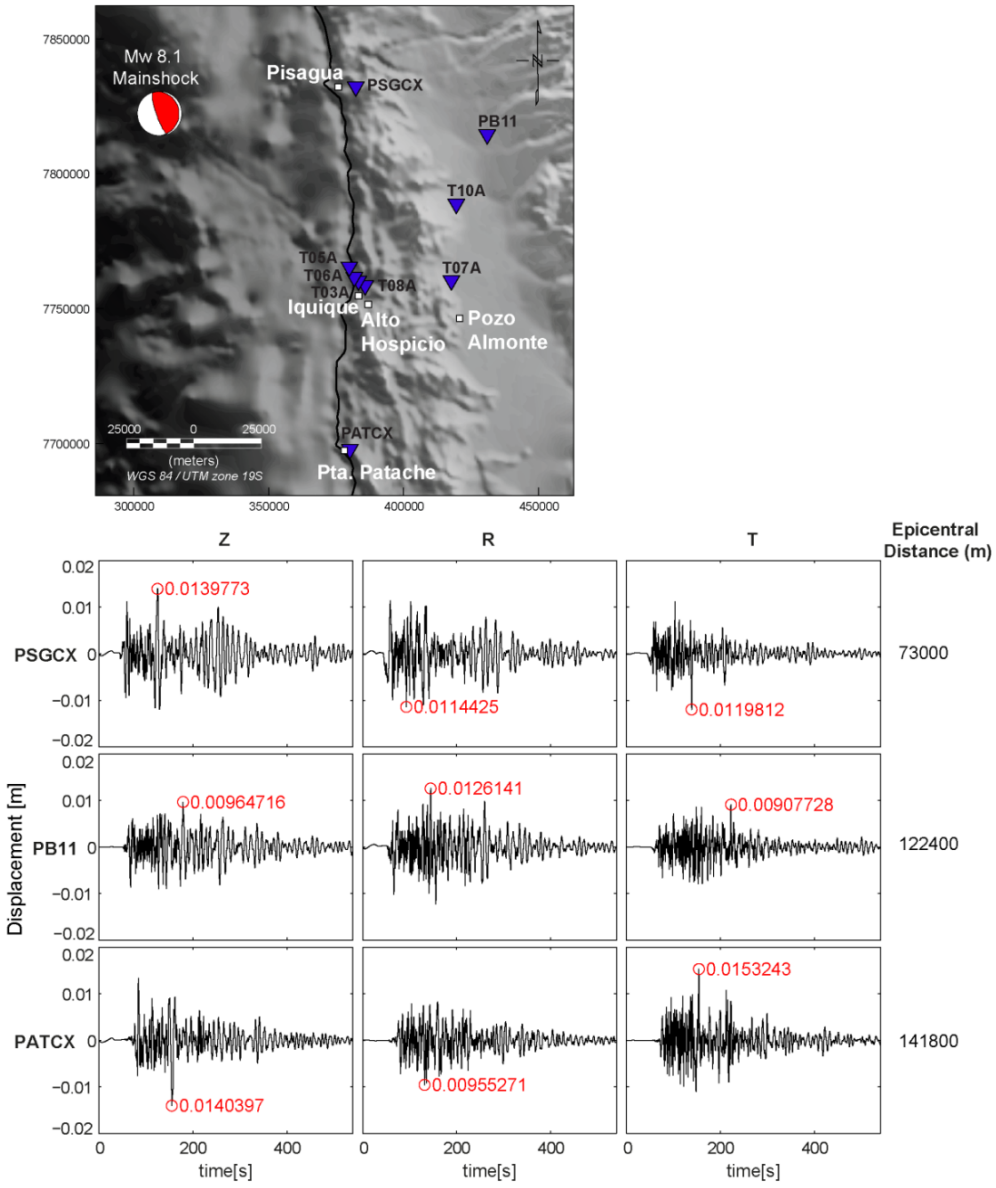

Figure 6: Upper Panel: Locations of the April 2014 Mw 8.1 Iquique earthquake and seismic stations. Lower Panel: Local three-component broadband displacement waveforms for the Iquique earthquake for three seismic stations showing evidence for site effects (the locations of the stations are shown in Figure 3). The waveforms are filtered using a Butterworth bandpass filter of order 2 with four poles from 0.1 to 20 Hz. The vertical (Z, left), radial (R, middle), and transverse (T, right) components are shown using the same horizontal and vertical scales. The red circles represent the maximum peak value for each trace, whose magnitude is also annotated in red.

3. GEOPHYSICAL AND GEOLOGICAL CONSTRAINTS OF THE STUDY AREA

In order to establish the geometrical and physical parameters for the construction of the numerical mesh, geophysical and geological studies are presented in this section.

As the damage distribution and important seismic amplification at the seismometers located in the cities of Iquique and Alto Hospicio were observed after the Iquique earthquake, a detailed geological and geophysical study was performed for the Iquique area, in which a complete geological revision and geophysical surveys, including gravity and transient electromagnetic (TEM), were carried out to assess the nature, geometry, and physical properties of the geomorphological units in these two cities, whose results are including in the numerical mesh. The results of this study are also showed in the published article *"Insights on the structural control of a Neogene forearc basin in Northern Chile: A geophysical approach"* (García-Pérez et al., 2018).

The Pampa del Tamarugal basin, located in the Central Depression, is a well-known sedimentary basin, and the evidence of amplification observed at seismometers PB11 and T07A during the Iquique earthquake is probably related to the effect of this basin. Hence, in this work, a comprehensive examination of the geology and the geophysical studies carried out in the Pampa del Tamarugal area by different authors was made, allowing the parameterization of the big basin in the numerical mesh (Farías et al., 2005; Jordan et al., 2010; Nester & Jordan, 2012; Viguier et al., 2018).

Finally, two seismic velocity models are revised (ANCORP & Oncken, 2006; Bloch et al., 2014; Husen et al., 1999; León-Ríos, 2015), as they were necessary to build the crustal velocity model used in the simulations.

3.1. IQUIQUE AREA

The Iquique area includes the geomorphological features of the Coastal Plain, the Coastal Cliff, and the western part of the Coastal Cordillera, and covers an area of approximately 680 km^2 (**Figure 7**). In this area, the Coastal Plain is represented by a series of emerged marine terraces with variable widths (reaching a maximum width of 3 km) which are limited in the east by the Coastal Cliff, a steep relief with a height of over 800 m. The Coastal Cliff also represents the western limit of the Coastal Cordillera, which in the study area is characterized by sequences of hills, and alluvial pediplains such as the Alto Hospicio basin, which corresponds to an intramountainous basin produced by displacements in forearc crustal faults. The following sections present details regarding the geology and geophysical surveys performed in the area.

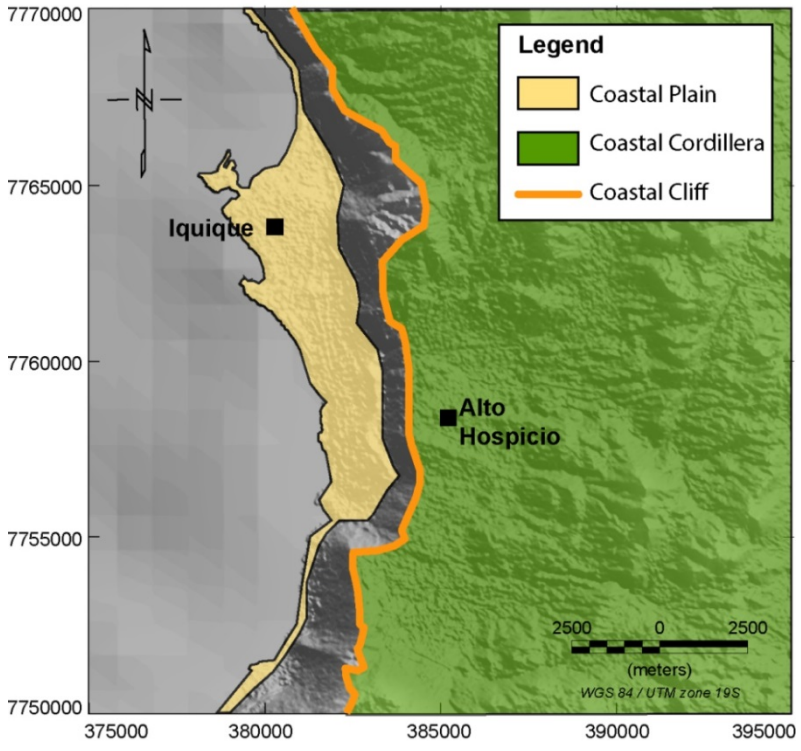

Figure 7: Geomorphological map of the Iquique area. Yellow area represents the Coastal Plain; green area represents the Coastal Cordillera and orange line the Coastal Cliff.

3.1.1.GEOLOGY OF THE IQUIQUE AREA

The geology of the Iquique area, presented in **Figure 8**, can be classified into five main units: (1) Middle–Upper Jurassic marine sedimentary rocks in the Huantajaya Group; (2) Early Cretaceous volcanic and sedimentary rocks in the Punta Barranco Formation; (3) Lower Jurassic–Lower Cretaceous intrusive rocks; (4) Miocene–Pliocene continental gravels; and (5) Quaternary sedimentary deposits (Marquardt et al., 2008; Vásquez & Sepúlveda, 2013). The oldest unit is the Jurassic marine sedimentary sequence included in the Huantajaya Group, which is composed of limestone, sandstones, and shale that were deposited during marine sedimentation in a volcanic back-arc basin (Sepúlveda & Vásquez, 2015). Later, during the Cretaceous, the continental volcanic sedimentary sequence of Punta Barranco was deposited. The volcanic facies is characterized by the alternation of brecciated lavas and andesites, whereas the sedimentary facies consists of successions of sandstone and conglomerates developed in a continental arc environment. Both the Punta Barranco Formation and the Huantajaya Group were intruded by subvolcanic intrusive rocks composed of monzodiorite, diorite, granodiorite, granite, and porphyritic diorite (Marquardt et al., 2008; Vásquez & Sepúlveda, 2013). After an extensive Paleogene hiatus, a sequence of gravels was deposited in an extensional intramountainous basin in the Coastal Cordillera. This unit, denominated the Alto Hospicio gravels, is mainly a coarse sand-matrix-supported gravel sequence cemented by halite with interbedded silts, clays, and some ash deposits. The documented ages ($^{40}Ar/^{39}Ar$) for this unit in the Alto Hospicio locality from ash deposits are ~14.58±0.12 Ma for the base sequence and 5.8±0.16 and 2.77±0.03 Ma for an upper level sequence (Marquardt et al., 2008). However, ash ages of ~22–23 Ma were reported in the bases of similar intramountainous basin deposits to the north and south of the study area (Vásquez & Sepúlveda, 2013). Lastly, Quaternary colluvium and alluvial deposits were attached to the coastal cliff and the slopes of some mountain fronts of the Coastal Cordillera and over marine terraces at the coast. Eolian deposits build stellar

dunes and sand sheets, both in the Coastal Cordillera and in the Coastal Plain, with Cerro Dragon (c.a. 200 m. a.s.l.) being the highest dune in the Chilean coast (Marquardt et al., 2008; Vásquez and Sepúlveda, 2013; Sepúlveda and Vásquez, 2015).

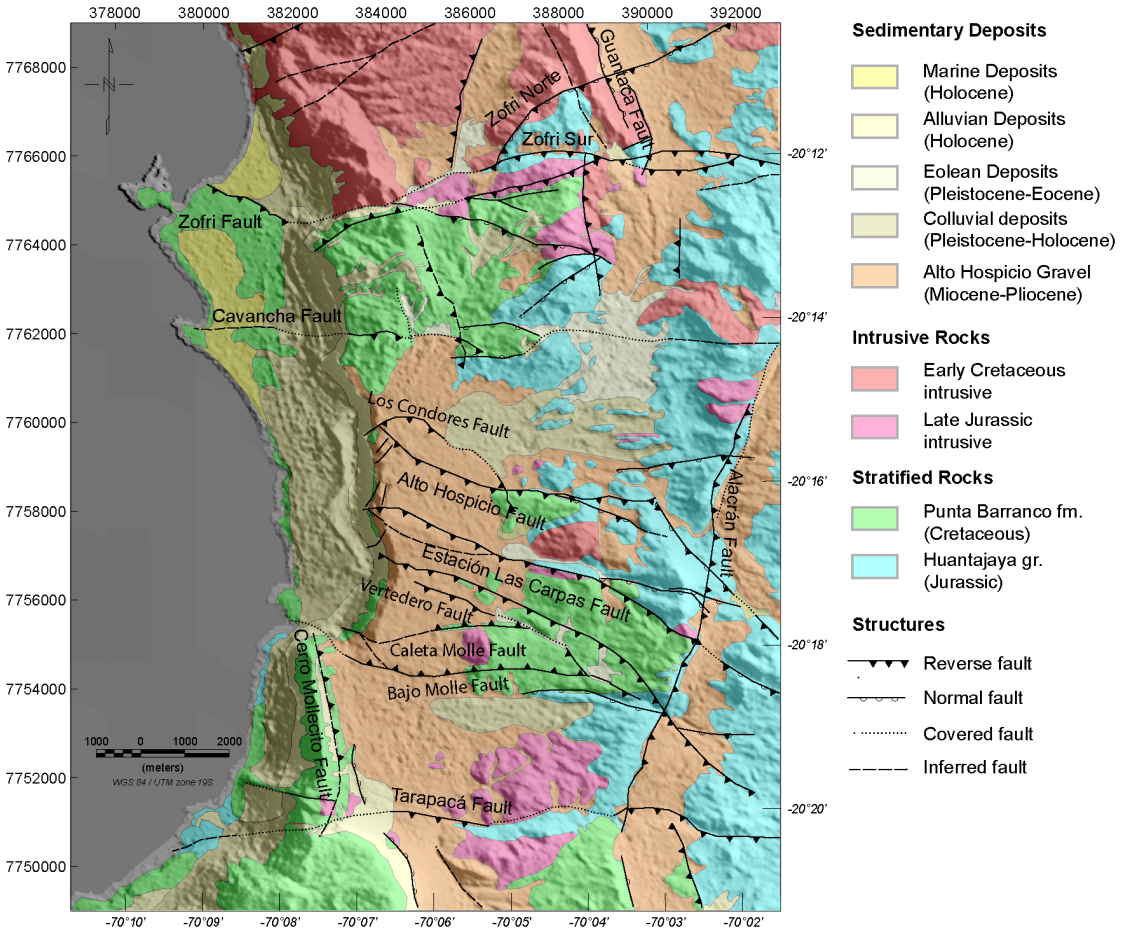

Figure 8: Local geological map of the Iquique area (modified from Marquardt et al. (2008) and Vásquez & Sepúlveda (2013)).

The structural geology in the study area is characterized by two main fault systems: N-striking normal faults and E/NW -striking thrust faults, as shown in **Figure 8**. The N-striking faults constitute scarps and limits of intramountainous basins but present poor exposures of their main

fault planes. Three large-scale sub-vertical faults (the Alacrán, Guantaca, and Cerro Mollecito faults) are observed in the area, having strikes between N10°–15°E and N0°–20°W and a maximum length of 28 km (Sepúlveda, 2014). These faults are genetically associated with the Atacama Fault System (AFS), which has a long-term deformation history since the Mesozoic (Armijo and Thiele, 1990; Cembrano et al., 2005; Armijo et al., 2015). The Cerro Mollecito N-striking fault represents one of the multiple traces of the Iquique Fault System, which is considered to be the northern segment of the AFS (González et al., 2008). During the Miocene, these structures acted as normal faults in an EW-extensional regime, developing half-graben basins which were later filled by colluvium and alluvial sediments of the Alto Hospicio gravels. Normal-fault kinematics continued to a lesser extent in the Pliocene. However, evidence of inverse reactivation on these faults has been reported by Vásquez and Sepúlveda (2013), who concluded that this reactivation uplifted sedimentary basins and affected Quaternary alluvial sediments.

Nine EW-striking steeply-dipping faults are present in the area, forming fault-propagated fold scarps, some of which have no clear fault surface exposure (the Zofri, Cavancha, Bajo Molle, Tarapacá, Estación Las Carpas, Vertedero, Caleta Molle, Los Condores, and Alto Hospicio faults). These scarps have strikes of N75°–105°E, lengths between 5 and 32 km, and heights of up to 160 m. These faults have acted with reverse kinematics since the Late Miocene, cutting Holocene sediments in the Coastal Plain (Vásquez and Sepúlveda, 2013; Sepúlveda, 2014). This local fault system evidences a NS-compressional regime (Allmendinger et al., 2005; Carrizo et al., 2008; Allmendinger and González, 2010).

3.1.2. GEOPHYSICS OF THE IQUIQUE AREA

Detailed gravity and TEM surveys have been conducted in the Iquique area, since both are traditional geophysical techniques widely used for basin-and-range studies and shallow stratigraphic applications (Thompson, 1959; Paterson and Reeves, 1985; Fitterman and Stewartj, 1986; Spies, 1989; Yáñez et al., 2015).

The gravity survey consisted of 425 measurement points, with an average spacing of 300 m, distributed in the Coastal Plain and the Coastal Cordillera, collected using a Scintrex CG5 relative gravity meter. Station elevations were measured using a differential GPS TRIMBLE C5. The TEM survey consisted of 12 sites located in the Alto Hospicio basin in the Coastal Cordillera, and used the FastSnap TEM equipment (Sharlov et al., 2010, 2017). The station arrangement for the gravity and TEM measurements, shown in **Figure 9**, was chosen to primarily identify the stratigraphic relationship between the geological units in the area and to establish the geometry of the Alto Hospicio basin.

Additionally, a total of 48 rock samples were collected from surface outcrops of the Jurassic Huantajaya Fm. (marine sedimentary), the Cretaceous Punta Barranco Fm. (volcano-sedimentary), and Jurassic–Cretaceous Intrusive rock units, and their densities were measured through the ratio of the rock weight in air and following immersion in water (e.g., Yáñez et al., 2015):

$$\boldsymbol{\rho} = \frac{\mathbf{Wair}}{\mathbf{Wair - Wwater}} \qquad \text{(Equation 3.1.2-1)}$$

This simple procedure gives an overall idea of the weathering and consolidation state of the rocks units.

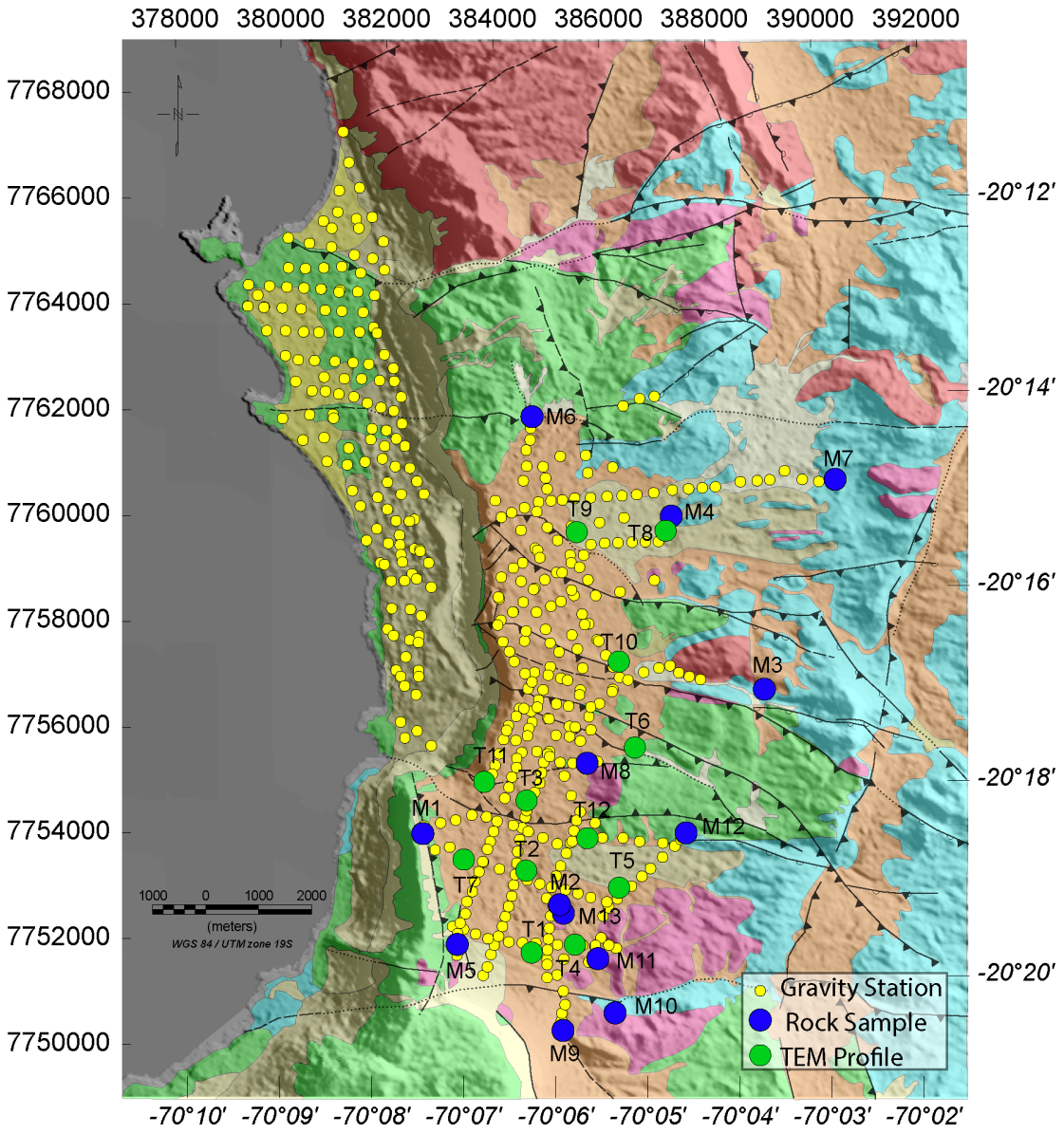

Figure 9: Locations of the stations for the geophysical surveys in the Iquique area over a modified local geological map. Yellow circles show the gravity stations, blue circles show the locations of the rock samples, and green circles show the location of the TEM sites (obtained from García-Pérez et al., 2018).

3.1.2.1. GRAVITY

The gravity data acquisition and reduction followed standard procedures (e.g., Teldford et al., 1990); the accuracy of the relative gravity data was better than 0.1 mGal, elevation errors were less than 30 cm, and a daily gravity base station was used to correct the instrumental drift. The tidal variation was continuously recorded using the Scintrex instrument and the latitude correction was made using the WGS84 reference ellipsoid. The absolute gravity value was obtained from the absolute base station located at the Physics Department in Arturo Prat University (CL-UAPF: 978663.2 [mGal]), Iquique, Chile. Free-air and Bouguer corrections were calculated following standard formulas using GPS-measured elevations (e.g. Teldford et al., 1990). An average crustal density of 2.67 g/cc was assumed for Bouguer and Terrain corrections, with a 50 km^2 SRTM90 local DEM being used to calculate the Terrain correction. The residual gravity anomaly was calculated after removing the regional first-order trend from the standard Bouguer anomaly grid to correct for the gravitational influence of the subducting Nazca Plate. The final residual gravity anomaly at a resolution of 100 m was obtained with gravity anomaly values ranging between –4.5 and +3.8 mGal, as in shown in **Figure 10**.

When linking the gravity anomaly grid with surface geology, the first-order gravity feature is represented by an elongated NS negative anomaly (between approximately –4.5 and 0 mGal). This anomaly is located between approximately 70°07'S and 70 ° 06’S longitudes, and is spatially associated with the Alto Hospicio gravels unit. The largest positive gravity anomalies (~1.0–4.0 mGal) are related to the Punta Barranco Fm., the Huantajaya Fm., and Jurassic and Cretaceous intrusive rocks located in both the coastal plain and coastal cordillera. The lowest gravity anomaly values observed in the coastal plain (~–2.0 to 0 mGal) is interpreted as the gravity response of Pleistocene–Holocene deposits and the Cerro Dragon stellar dune next to the coastal cliff.

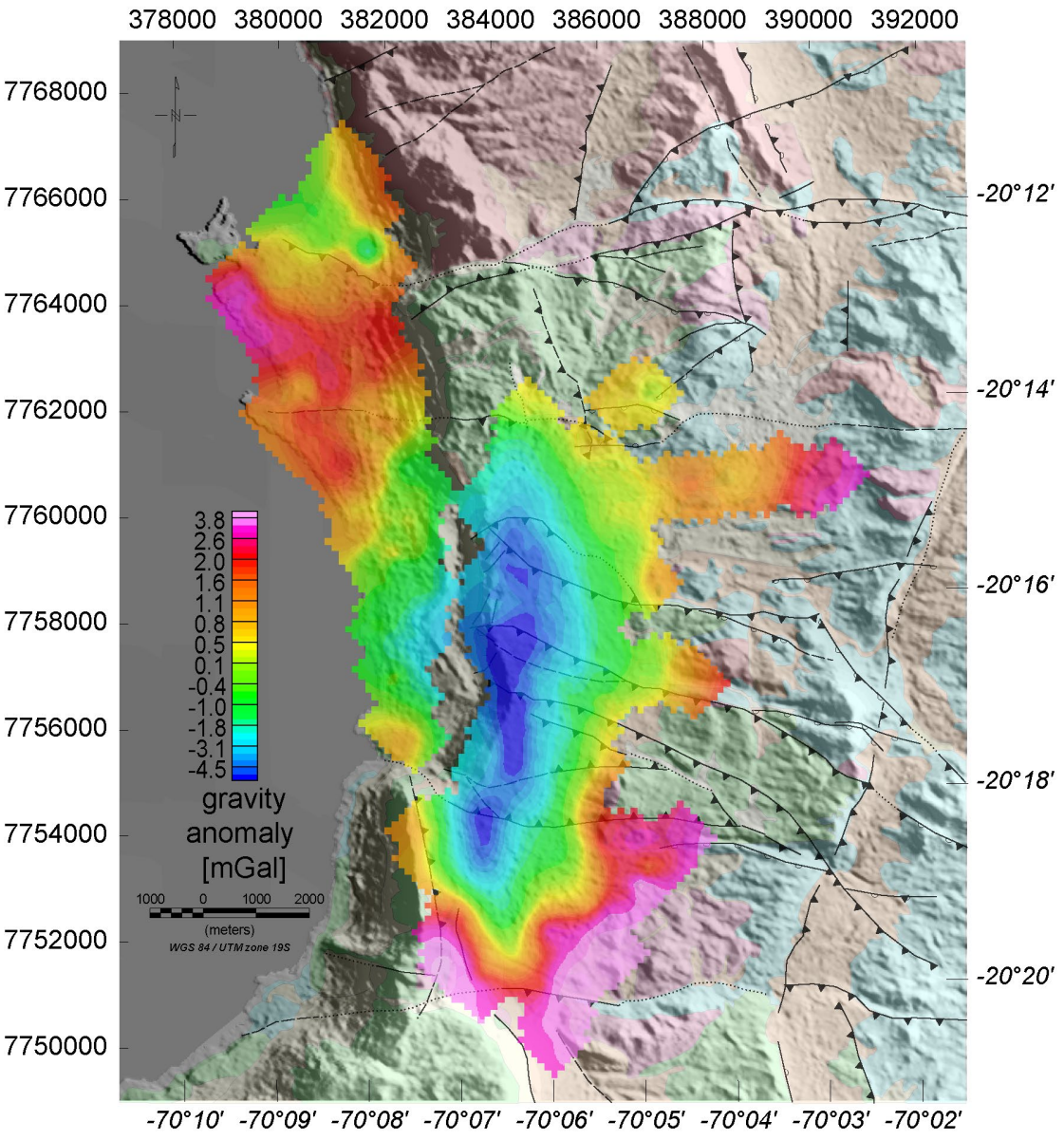

Figure 10: Bouguer gravity anomaly (colored grid) over a faded modified local geological map for the Iquique area. The Bouguer gravity anomaly ranges from –4.5 mGal to 3.8 mGal (obtained from García-Pérez et al., 2018).

3.1.2.2. ELECTROMAGNETIC TRANSIENT

The TEM measurements were realized using a central rectangular loop configuration of a 200 x 200 m^2 transmitter coil and a 50 x 50 m^2 receiver coil, which under mid-to-high resistivity values (above 100–200 ohm-m) enables observation depths down to several hundred meters (Kozhevnikov et al., 2016). However, this geometrical configuration gives rise to a blind region in the upper 20–40 m. From the observation of voltage decay, the apparent resistivity curve was calculated with accuracies better than 10% using standard 1-D inversion models with four layers and a semi-space (Spies, 1989; Sharlov, 2017). The apparent resistivities versus depth profiles obtained for each TEM station are shown in **Figure 11**.

The inverted resistivity values obtained via TEM can be linked to the lithological units present in the study area based on the electrical behavior of various rock types compiled from worldwide studies (Teldford et al., 1990; Dentith and Mudge, 2014). Low values of resistivity (17–72 ohm-m) observed at shallow depths were related to sedimentary sequences of gravels; low resistivity values (5–90 ohm-m) located at medium depths were associated with volcanic rocks that are highly fractured and percolated by water; high resistivity values (230–2100 ohm-m) at medium depths were interpreted as intrusive rocks; and high resistivity values (700–1200 ohm-m) located at large depths (>400 m) were assumed to be consolidated marine sedimentary rocks. These resistivity values and the respective geological units are summarized in **Table 2**.

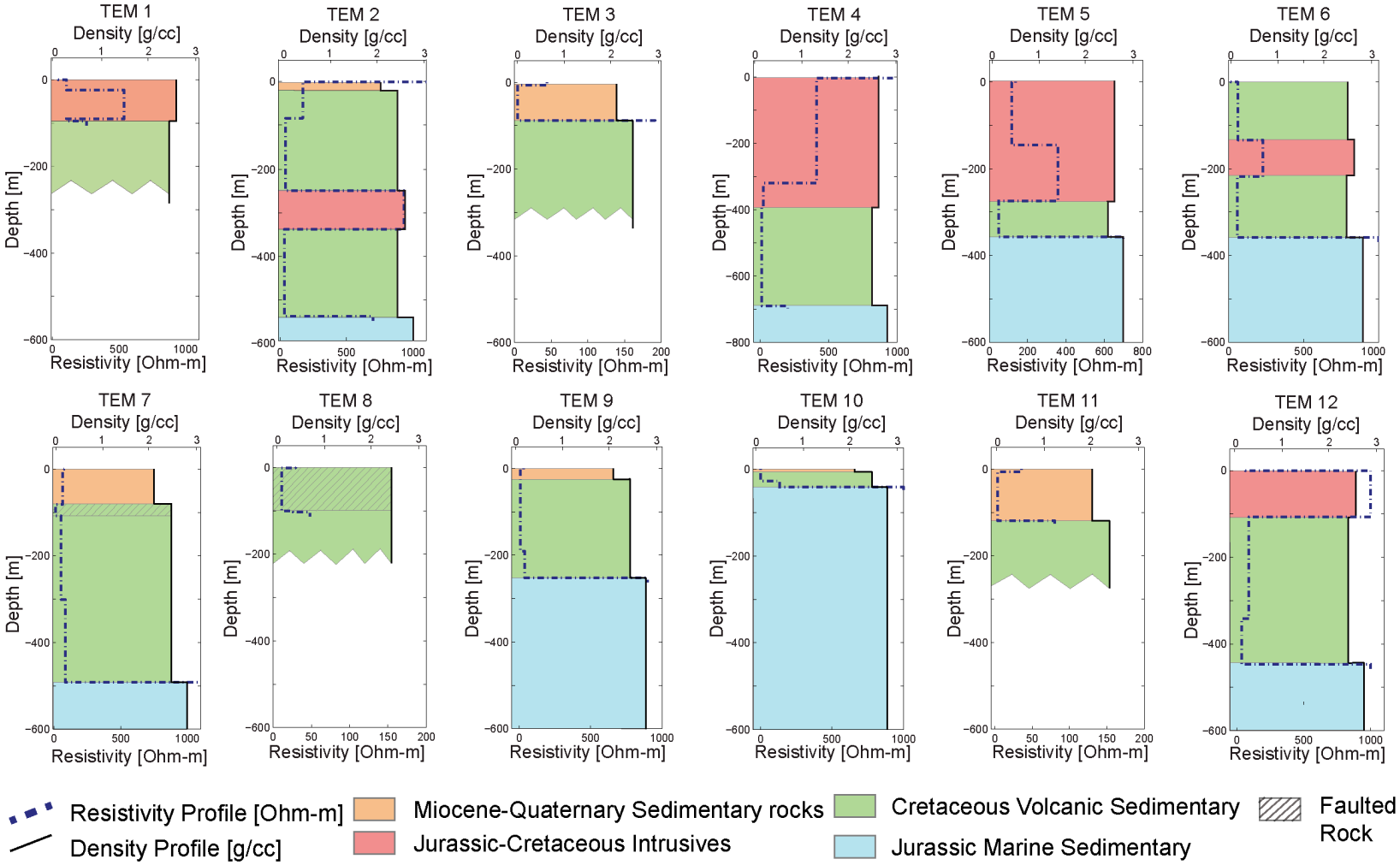

Figure 11: Resistivity and density vs depth profiles for TEM stations (locations shown in Figure 9). Blue dashed lines show resistivity profiles, black dashed lines show density profiles, colored blocks show the lithological interpretation, and dashed blocks represent faulted rocks (modified from García-Pérez et al., 2018).

3.1.3. INTEGRATED GEOLOGICAL–GEOPHYSICAL ANALYSIS

For density analysis, the 48 rock outcrop samples were identified and classified into three main geological units: jurassic–cretaceous intrusive, cretaceous volcano-sedimentary and jurassic marine sedimentary rocks. The results are shown in **Table 2**, presenting the minimum and maximum density value measured for each geological unit. For the miocene–quaternary sedimentary unit, density was estimated by a gravity anomaly inversion, which is explained later in this section.

Table 2: Resistivity and density values for geological units obtained from the geophysical surveys.

Geological Unit	**Density [g/cc]**	**Resistivity [Ohm-m]**
Miocene–Quaternary Sedimentary	1.95	17–72
Jurassic–Cretaceous Intrusive	2.64–2.67	230–2100
Cretaceous volcano-sedimentary	2.39–2.65	5–171
Jurassic marine sedimentary	2.72–2.89	700–1200

For each individual rock unit, a range of resistivity values was designated based on the assumed mineral composition and potential for water retention, as inferred from the local geology and the rock density analysis. The miocene–quaternary sedimentary unit (Alto Hospicio gravels) have high halite, silt, and clay content, all of which can be expected to retain groundwater, if present, and can thus explain the low resistivity values (4–72 ohm-m) observed at shallow depths (upper ~100 m) at stations TEM 3, TEM 7, and TEM 11 (**Figure 11**). Based on correlations between site surface geology and gravity modeling, the cretaceous volcano-sedimentary sequence (brecciated lavas and conglomerates) is assumed to be associated with low-to-moderate resistivity values (5–171 ohm-m). Geological observations and the density results obtained in this study (2.39–2.65 g/cc) indicate that this sequence is highly fractured, and

accordingly the presence of infiltrated groundwater in this rock can explain the observed resistivity values. It is possible to interpret that the extremely low resistivity values (5–10 ohm-m) which are observed at stations TEM 7 and TEM 8 are related to fault damage zones, which in previous studies have been shown to exhibit similar values of resistivity (e.g., Roquer et al., 2016). The medium-to-high resistivity values (230–2100 ohm-m) observed at stations TEM 1, TEM 2, TEM 4, TEM 5, TEM 6, and TEM 12 are interpreted as Jurassic–Cretaceous intrusive units, since their values are consistent with standard resistivity values for intrusive rocks (e.g., Teldford et al., 1990; Dentith and Mudge, 2014). The wide range of resistivity values for this layer is attributed to a variable degree of rock weathering, with medium resistivities identifiable as highly weathered rock near the surface and high resistivities as fresh rock at depth. Lastly, the high values of resistivity (700–1200 ohm-m) presented at eight TEM stations are related to the Jurassic marine sedimentary unit. The measured density for this rock unit ranges between 2.72 and 2.89 g/cc, which are high values for shale, sandstone, and limestone. However, these high values of resistivity and density can be explained by an impermeable old consolidated marine-continental sedimentary rock which has been slightly metamorphosed by local intrusive rocks. Four stations (TEM 1, TEM 3, TEM 8, and TEM 11) do not reach this high resistivity layer as the penetration depth is less than 200 m in these cases.

A 3-D depth-to-basement model was computed applying a prismatic algorithm to invert the residual gravity and using the information obtained from the TEM profiles and the density results (e.g., Plouff, 1976; Yáñez et al., 2015). Stations TEM 3 and TEM 11 were used as control points for the depth to basement based on the thickness of the first low resistivity domain, and the average density of the basement rock was obtained from the petrophysical data (2.62 g/cc). Both the density of the miocene–quaternary sedimentary unit (1.95 g/cc) and the 3-D basement depth grid were estimated from the gravity inversion algorithm.

The results of the 3-D depth-to-basement model are shown in **Figure 12**, where the basement depth surface grid (yellow–red color) shows a north–south, 9200 m long, 2500 m wide, NS elongated basin with a maximum depth of 300 m, related to the Alto Hospicio basin infill. The deepest part of the basin is located in the west, next to the Coastal Cliff. The basin is limited by the Cavancha Fault to the north and the extension of the Iquique Fault to the south. Short-wavelength features in the grid are interpreted as an uneven basement surface which is cut and displaced by the EW/NW-SE fault system that deforms the surface of the Alto Hospicio gravels.

By integrating the information obtained from TEM profiles, basement depth gravity inversion, and surface geology, four geologically interpreted basement-TEM cross-sections are presented, showing the stratigraphic relationships among the four main geological units down to 600 m. Details of these sections are presented in **Table 3** and their locations are given in **Figure 12**.

Table 3: Basement-TEM cross-section information.

	Orientation	**Length (m)**	**TEM station**
Section 1	EW	6000	TEM 7, TEM 2, TEM 5
Section 2	NNW-SSE	10,500	TEM 11, TEM 3, TEM 12
Section 3	NS	11,000	TEM 3, TEM 2, TEM 1
Section 4	NS	11,000	TEM 9, TEM 10, TEM 6, TEM 12, TEM 4

In the Basement-TEM cross-section, the main geological units are illustrated according to their physical properties and the surface geology. The miocene–quaternary sedimentary unit is represented by the rock volume above the basement depth gravity inversion, whereas the other three units (jurassic–cretaceous intrusive, cretaceous volcano-sedimentary, and jurassic marine sedimentary) are identified from the TEM resistivity layers. The cross-sections also show Quaternary and Neogene faults as uniform or discontinuous lines (**Figure 13**).

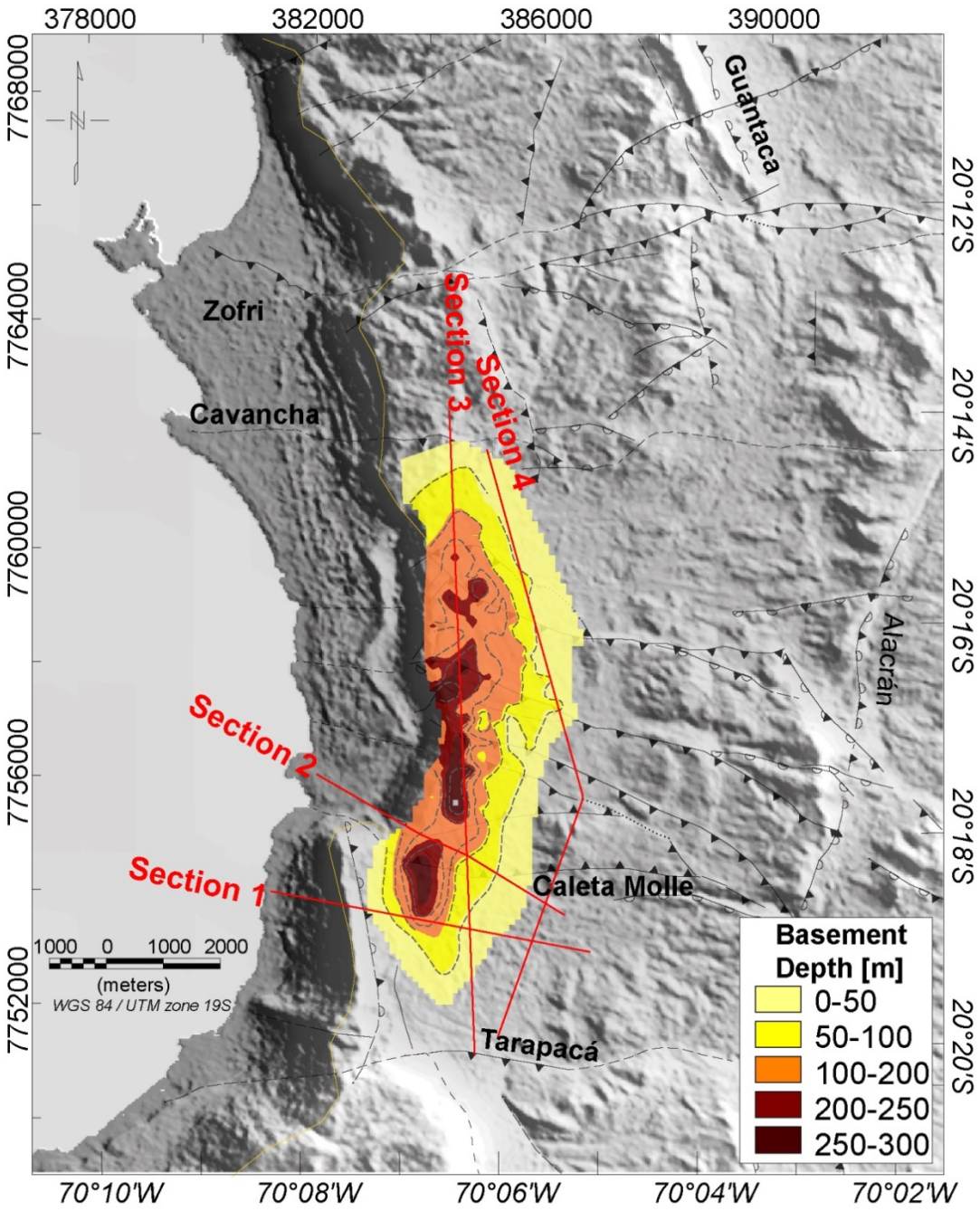

Figure 12: Basement depth 3-D gravity inversion (dark red to yellow iso-thickness grid) over a grey shaded relief map and structural fault systems. Red lines show the basement-TEM cross-sections presented in Figure 13 (obtained from García-Pérez et al., 2018).

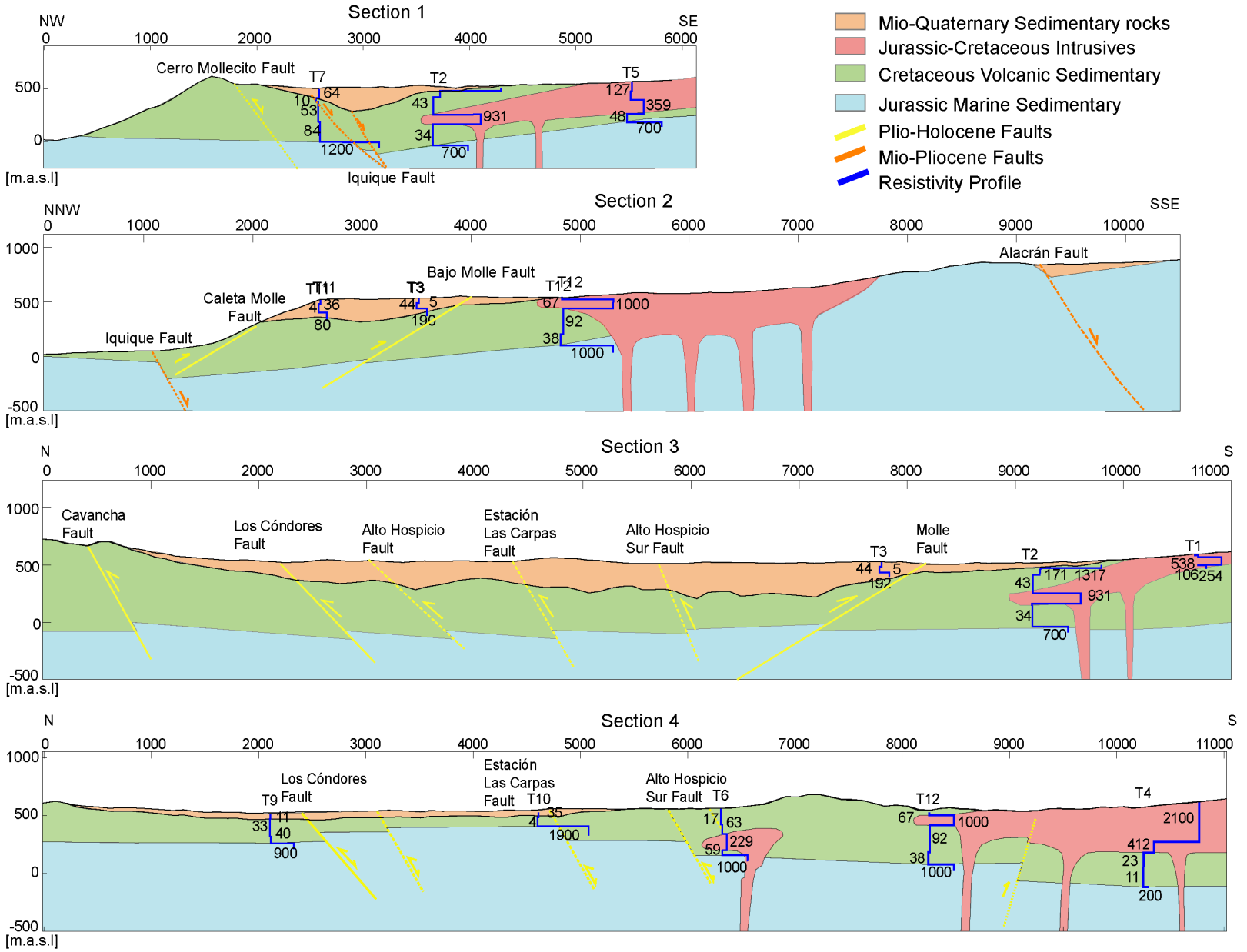
Section 1
NW
SE
Cerro Mollecito Fault
Iquique Fault
[m.a.s.l]
Section 2
NNW
SSE
Alacrán Fault
Bajo Molle Fault
Caleta Molle Fault
Iquique Fault
Section 3
N
S
Cavancha Fault
Los Cóndores Fault
Alto Hospicio Fault
Estación Las Carpas Fault
Alto Hospicio Sur Fault
Molle Fault
Section 4
Mio-Quaternary Sedimentary rocks
Jurassic-Cretaceous Intrusives
Cretaceous Volcanic Sedimentary
Jurassic Marine Sedimentary
Plio-Holocene Faults
Mio-Pliocene Faults
Resistivity Profile

Figure 13: Integrated geological and geophysical interpretation. Section locations are shown in Figure 12. Lithological units are represented by colored blocks. Faults are presented as colored lines, solid lines for documented dip faults and segmented lines for inferred dip faults. Blue lines represent resistivity profiles showing resistivity values in ohm-m (obtained from García-Pérez et al., 2018).

One of the main results of this study is the definition of the geometry of the Alto Hospicio basin interpreted from the basement depth gravity inversion as a NS elongated feature with an estimated area of 23 km^2 and a maximum depth of 300 m (**Figure 12**). This geophysical approach to estimate basin thickness is unprecedented in the area, and the obtained depth values agreed with the estimate of basin thickness obtained from geological observations for the Alto Hospicio basin (Marquardt et al., 2008) and for other tectonically controlled basins in Northern Chile (González et al., 2006). As the amplification of seismic waves during an earthquake related to sedimentary basins has been widely reported and studied (Çelebi, 1987; Sánchez-Sesma and Luzon, 1990; Frankel et al., 2002; Graves, 1993; Parolai et al., 2002; Sánchez-Sesma et al., 2002), the characterization of the Alto Hospicio basin is important to determine a causal relationship between the basin and site effects. In the following sections, this characterization will be used in the implementation of the model.

From the TEM profiles, the very low values of resistivity were associated with water hosted in the Alto Hospicio gravels and the Cretaceous volcano-sedimentary unit, whose presence is extremely important for this study as it allows the distinction of the different types of rock units and undergirds the stratigraphic model suggested in **Figure 13**. Although the existence of groundwater in this hyperarid desert is controversial as current recharge mechanisms are unknown, the aquifer located in the Pampa del Tamarugal basin, to the east of the study area, is a good example of groundwater hosted in a sedimentary basin (Houston, 2002; Magaritz et al., 1990; Viguier et al., 2018).

3.2. PAMPA DEL TAMARUGAL BASIN AREA

The Pampa del Tamarugal basin is a 400 km long basin filled with sediments with ages from the late Oligocene to the present and extending from 18–22°S (Nester & Jordan, 2012) and including the eastern part of the Coastal Cordillera, the Central Depression, the Andes Precordillera, and the eastern part of the Andes Cordillera **(Figure 14)**.

As explained before, the Coastal Cordillera is a Jurassic–Cretaceous mountain range that exhibits a smooth relief up to 1200 m in altitude that uniformly declines in its eastern part. The Central Depression is a nearly flat N-S trending elongated tectonic basin with a variable width between 30 and 40 km and a mean altitude of 1000 m, filled with sediments derived from the erosion of the Andes and eruptions of volcanoes in the western Cordillera. The Precordillera is a gentle west-sloping surface crossed by W-E trending narrow deep valleys; it has altitudes between 1500 and 3600 m, marks the western edge of the Altiplano-Puna Plateau, and is constituted by alluvial and pyroclastic flows units. The western part of the Main Cordillera has an irregular topography, with heights between 3800 and 4700 m a.s.l., crowned by Neogene to present-day stratovolcanoes with heights of 5000 to 6900 m a.s.l. (e.g., Farías et al., 2005; Jordan et al., 2010; Nester & Jordan, 2012; Victor et al., 2004).

In this work, the northern part of the Pampa del Tamarugal basin is studied, covering approximately 4000 km^2 (blue rectangle in **Figure 14**) corresponding to the area in which the seismometers are located and including the geomorphological features of the eastern part of the Coastal Cordillera and the Central Depression.

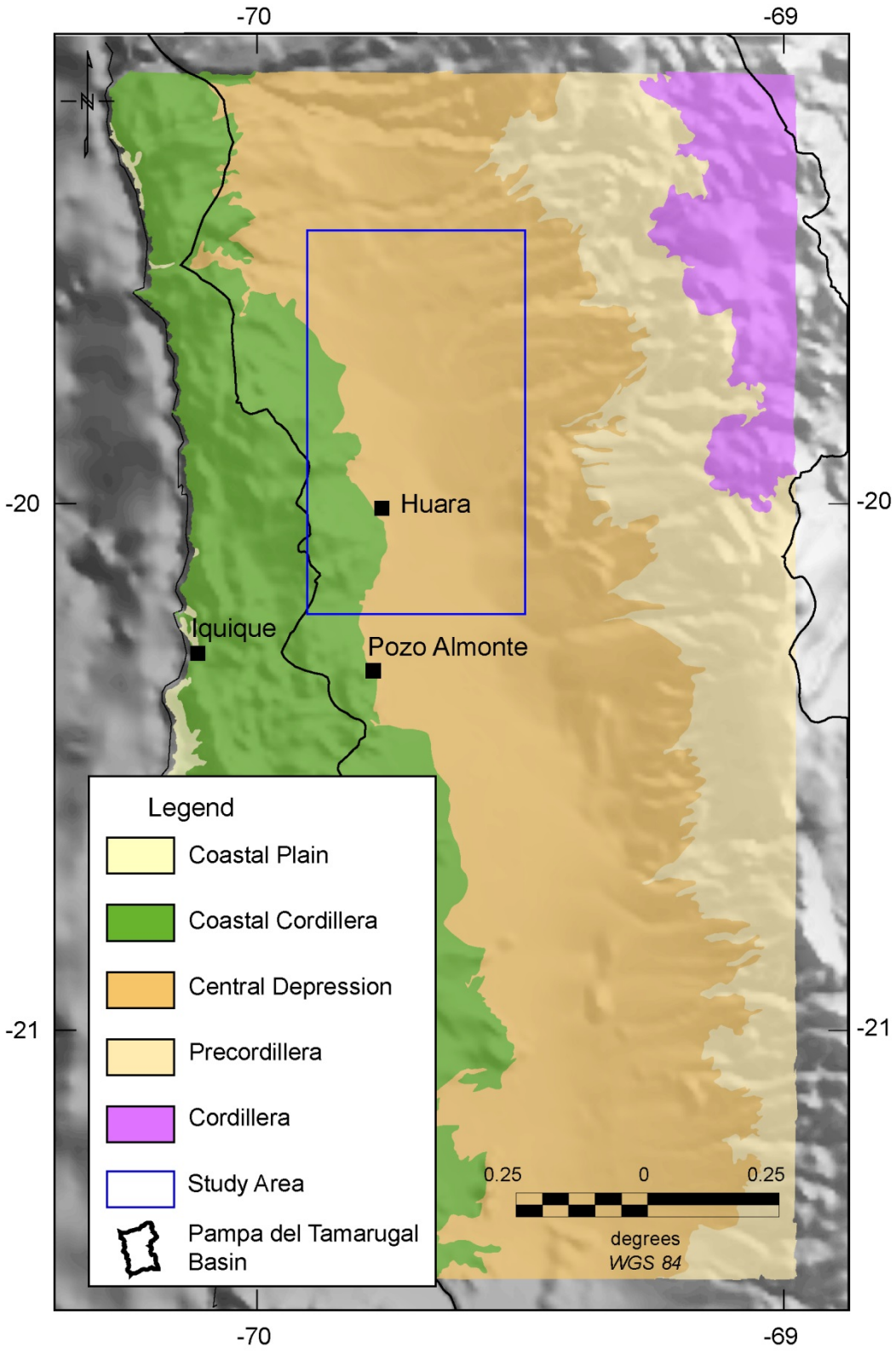

Figure 14: Geomorphological map of the Pampa del Tamarugal basin area.
Tiaren García Pérez

3.2.1. GEOLOGY OF THE PAMPA DEL TAMARUGAL AREA

The surface geology of the Pampa del Tamarugal basin, presented in **Figure 15**, can be classified into five main units (López et al., 2017): (1) Quaternary sedimentary deposits; (2) Oligocene–Pliocene sedimentary deposits; (3) Cenozoic volcanic rocks; (4) Mesozoic rocks; and (5) Paleozoic rocks. The Quaternary sedimentary deposits correspond to (a) saline evaporite sediments composed of sulfides, carbonites, nitrates, silt, clay, and sand that emerge in the western part of the Central Depression, and (b) Holocene and Pleistocene non-consolidated clastic deposits composed of gravel, sand, silt, and clay extended widely along the Central Depression, the Coastal Cordillera, and the Precordillera, filling valleys and creeks. In the Oligocene–Pliocene sedimentary deposit unit, the following can be found: (a) alluvial gravels and coarse sand, interspersed by eolian sand from the Upper Miocene and Pliocene extended in the western part of the Precordillera, in the central and southern part of the map; b) welded tuff composed of lapilli and ashes of rhyolitic and dacitic composition widely extended in the Precordillera, at the central and northern part of the map; (c) the Alto Hospicio gravels, distributed over the Coastal Cordillera; and (d) Oligocene–Miocene volcanic and clastic sedimentary deposits constituted mainly by conglomerates and sandstones which are semi-consolidated and interbedded with ignimbrites, pumice, and lavas (López et al., 2017; Vásquez & Sepúlveda, 2013). The Cenozoic volcanic rock unit corresponds to basaltic, andesitic, dacitic, and rhyolitic lavas and volcanic edifices (Blanco et al., 2012; López et al., 2017) associated with the volcanic activity developed from the Miocene to the present, extended in the northern part of the Precordillera. The Mesozoic rock unit corresponds to the Jurassic–Cretaceous volcano-sedimentary and marine sedimentary rocks located in the Coastal Cordillera and Jurassic–Cretaceous continental sedimentary rocks in the Precordillera (Blanco et al., 2012; López et al., 2017). Finally, the Paleozoic rocks correspond to metamorphic, marine sedimentary, igneous,

and volcanoclastic outcrops that emerge in the Precordillera and represent the basement of the area.

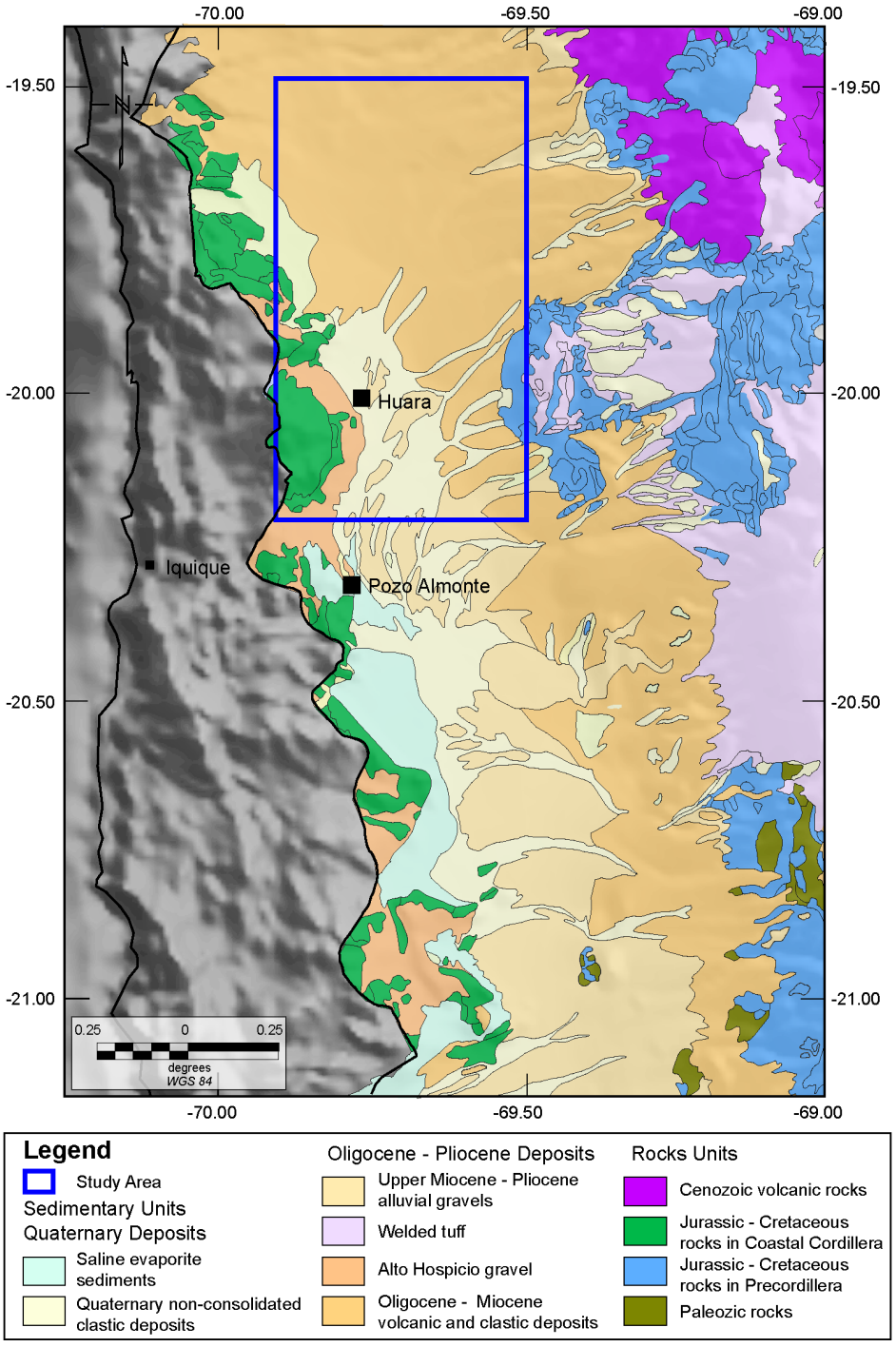

Figure 15: Geological map of the Pampa del Tamarugal basin area (modified from Sernageomin, 2003).

The geological evolution of the emerged forearc has been governed by the eastward migration of the volcanic front from its Jurassic position in the Coastal Cordillera to its present position in the Western Cordillera (outside of the study area map). Most of the deformation of the Precordillera and the forearc is Paleogene, probably related to major subvertical strike-slip fault systems that originally acted as oblique contractional structures in the various magmatic arc segments such as the Western Thrust System (WTS) (Farías et al., 2005; Herrera et al., 2017; Muñoz & Charrier, 1996; Victor et al., 2004) and the AFS (Scheuber & González, 1999). The record of these deformation processes is poor in the Pampa del Tamarugal due to the thick (1000–1500 m) sequence of Cenozoic non-marine siliciclastic deposits that covers the area (Jordan et al., 2010; Victor et al., 2004).

According to stratigraphic studies carried out in the area (Farías et al., 2005; Nester, 2008; Nester & Jordan, 2012; Victor et al., 2004), the Cenozoic sedimentary sequence is variable along the Pampa del Tamarugal. Nevertheless, with the corresponding correlations of sedimentary sequences, Victor et al. (2004) defined five main units in the Altos de Pica Region. The sedimentary units include three sedimentary members and two ignimbrite units. The basal unit (APF1) consists of fanglomerate, immature sandstone, and polymictic conglomerate derived from the erosion of the underlying pre-Neogene basement, with an estimated average thickness of 300 m, correlated with the Azapa Formation. The ignimbrite unit (APF2) conformably overlies the APF1 unit with an average thickness of 20 m. The APF3 unit is composed of sandstones and conglomerates that conformably cover the ignimbrite member APF2, with an estimated average thickness of 200–300 m and a maximum thickness of 500 m in some areas, correlated with the Oxaya formation. The second ignimbrite unit (APF4) has a thickness up to 150 m and conformably overlies the APF3 unit. With a minor unconformity, the superficial unit APF5 is constituted by medium-to-fine grained sandstone and thin conglomeratic beds that cover the older units with an average thickness of 200 m and a thickness of up to 550 m is some

areas; this unit can be correlated to the El Diablo Formation. **Figure 16** shows a simplified stratigraphic log of the Cenozoic cover in the Central Depression in the Altos de Pica Region.

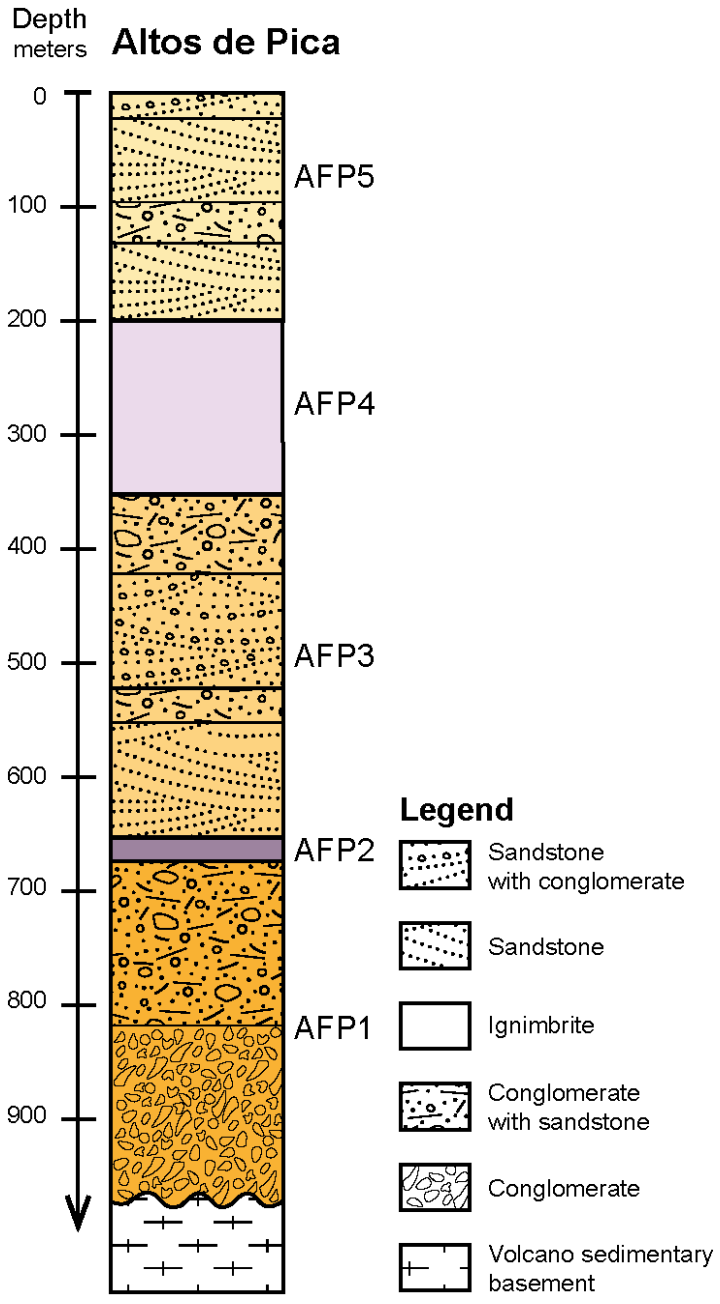

Figure 16: Simplified stratigraphic sequence of the sedimentary deposits in the Central Depression in the Altos de Pica Region (modified from Victor et al., 2004).

3.2.2. GEOPHYSICS OF THE PAMPA DEL TAMARUGAL AREA

In general, the geophysical studies performed in the Pampa del Tamarugal area mainly focused on the characterization of the groundwater availability and recharge, as the aquifer hosted in the basin represents an important resource for human activity in this hyperarid environment. Therefore, these works are concentrated mostly in the determination of the aquifer geometry, the water table level, and the basement shape by using TEM and gravity techniques. Although the purposes of these studies, the information related to the basement shape is useful for the geometrical characterization of the Pampa del Tamarugal needed for the construction of the mesh.

Figure 17 shows the station locations of the main geophysical studies carried out in the area performed by the General Water Direction (DGA) (Arenas et al., 2013), Nester (2008) and Viguier et al. (2018), as well as the basin depth grid obtained from the hydrogeological study of López et al. (2017). From **Figure 17**, it can be seen that the majority of the geophysical studies are located in the Altos de Pica area, in the east part of the Pampa del Tamarugal basin, as the water demand in this area has increased in recent decades due to agricultural demand; therefore, the evaluation of the basin depth is extremely important. Meanwhile, the study performed by Viguier et al. (2018) in the northern part of the Pampa del Tamarugal basin contributes to the understanding of water recharge of the Pampa del Tamarugal aquifer in the northern area.

The geophysical surveys in the Altos de Pica area (Arenas et al., 2013) consisted of 218 gravity stations and 91 TEM stations, covering an area of approximately 1200 km^2. In this study, the gravity analysis found basement at depths between 300 and 1000 m, interrupted by some hills in the western and northern part of the study area. Meanwhile, the TEM analysis observed the groundwater level at depth between 25 and 75 m below the surface. These results agree with the seismic study performed by Nester (2008), in which the maximum thickness of the basin fill is

found in the eastern and southern parts of the study area, with thicknesses between 1500 and 1700 m; in the west-central portion, the sediment thickness exceeds 200 meters and the western section shows a sub-basin filled with 600–1000 m of sediments. These results were compiled in the hydrogeological study presented in López et al. (2017).

In the northern part of the study area, the geophysical survey presented by Viguier et al. (2018) consisted of 92 TEM stations, whose analyses showed groundwater levels between 1000 and 1160 m below the surface, confined in the lower part of the basin. Notwithstanding the scarcity of geophysical information in the Pampa del Tamarugal area, for the purpose of this work, the results obtained by Viguier et al. (2018) constitute valuable information in the definition of the geometry of the modeled northern part of the Pampa del Tamarugal basin.

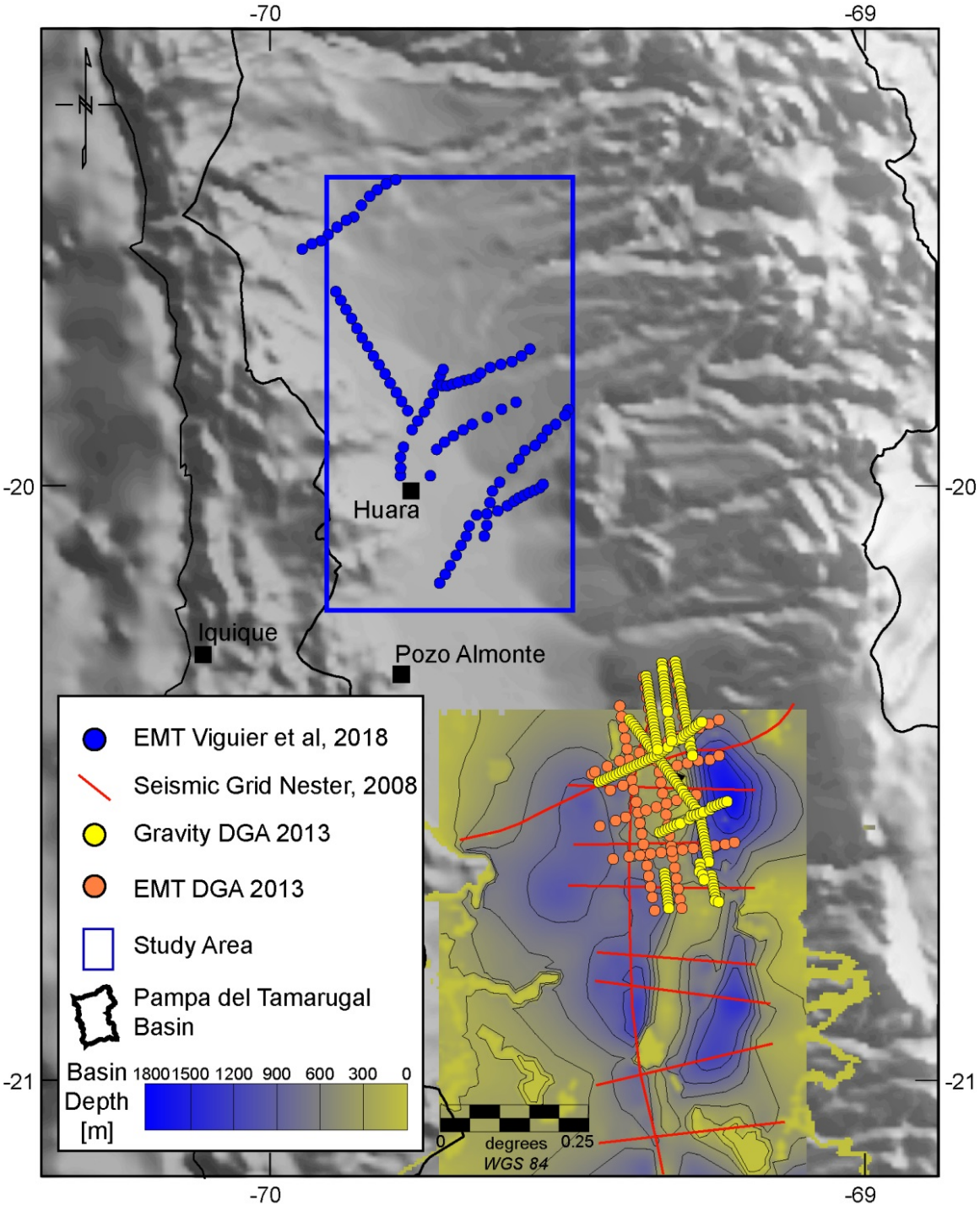

Figure 17: Map showing the locations of the geophysical survey stations in the Pampa del Tamarugal basin. Yellow and orange circles show the gravity and TEM stations for the 2013 DGA study (Arenas et al., 2013), blue circles show the TEM stations from the study of Viguier et al. (2018), red lines show the seismic profiles obtained by Nester (2008), and the colored grid represents the basin depth obtained by López et al. (2017).

3.3. CRUSTAL VELOCITY MODELS

Crustal velocity models are representations of the dynamic nature of the materials that comprise the earth's crust, defined by the seismic wave propagation velocities. Typically, velocity models are built from the inversion of the motion registered at seismic stations produced by earthquakes, as the travel time of a seismic wave depends on the hypocentral parameters and the seismic velocities along the ray paths between the stations and the hypocenter. Therefore, by solving the coupled hypocenter-velocity model problem, it is possible to obtain the velocity structure and the hypocenter locations.

In the Iquique region between 20 and 22°S, seismological studies conducted prior to the Iquique earthquake focused on slab-related seismicity and intermediate-depth earthquakes, as the seismicity was mainly located at depths of 80–130 km (Diana Comte & Suárez, 1995; Rietbrock & Waldhauser, 2004). The Andean Continental Research Project 1996 (ANCORP & Oncken, 2006) studied a 400-km-long seismic reflection profile integrating various geophysical experiments across the Central Andes at 21°S, obtaining a seismic imaging of the continental margin that was later combined with crustal seismicity obtained from two local seismic networks to build a high-resolution image of the subduction zone (Bloch et al., 2014).

After the Iquique earthquake, several works studied the nature of the entire seismic sequence, focusing on the determination of hypocentral locations, focal mechanisms, and the rupture processes of the foreshocks, mainshock, and aftershocks. Generally, standard inversion methods using 1-D velocity models were used in these studies as they usually achieve reliable and precise hypocenter locations (Husen et al., 1999; León-Ríos et al., 2016).

For the numerical modeling presented in this work, a crustal velocity model was needed. Therefore, in the following sections, the 1-D and 2-D velocity models used in this study are explained in detail.

3.3.1. 1-D VELOCITY MODEL

The 1-D velocity model obtained by Husen et al. (1999) for the Antofagasta region, located 200 km south of the Iquique region, was developed by applying the minimum 1-D model by incorporating the iterative simultaneous inversion of velocity and hypocenter parameters for the sequence of the Mw 8.0 Antofagasta earthquake of 30 July 1995.

Figure 18 shows the Vp, Vs, and density profiles up to a depth of 70 km depth used by León-Ríos (2015) for the location and computation of the centroid and the moment tensor for the Iquique earthquake sequence, modified from the original values obtained for Northern Chile by Husen et al. (1999). These velocities and density values were used in this work to construct the 1-D velocity model.

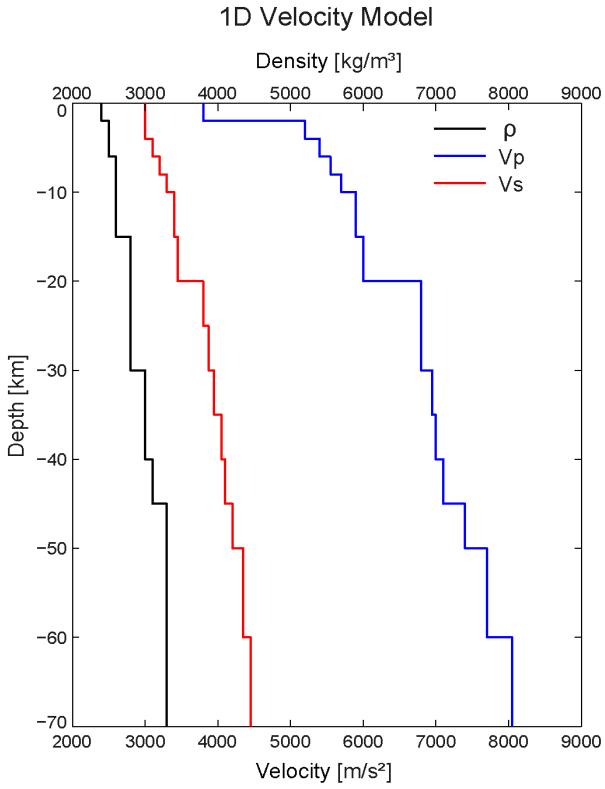

Figure 18: The 1-D velocity model used by León-Ríos (2015) to locate the Iquique earthquake sequence, modified from the velocity model proposed by Husen et al. (1999) for Northern Chile obtained from the Antofagasta earthquake sequence.

3.3.2. 2-D VELOCITY MODEL

The ANCORP'96 project collected geophysical data to construct a seismic image of the convergent continental margin and plateau in the Central Andes at approximately 21°S (**Figure 19**). The experiment collected onshore reflection data, and processed these data together with wide-angle offshore reflection data acquired previously by the CINCA'95 project in order to image the deep lithosphere with particular emphasis on the Nazca Plate Reflector and the Quebrada Blanca Bright Spot. The data obtained and processed was correlated with other geophysical data, such as gravity and heat flow, electrical resistivity models, seismicity and surface geology data.

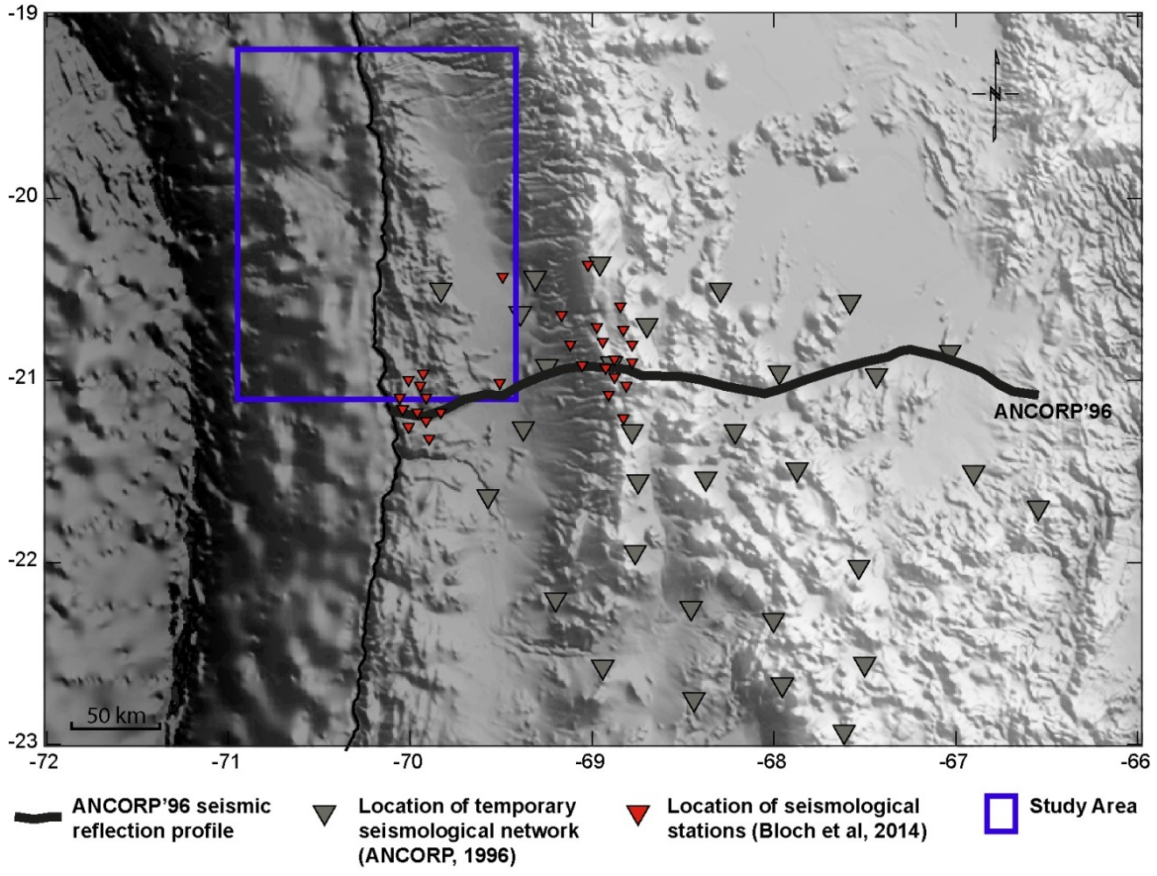

Figure 19: Location map of the ANCORP'96 reflection and refraction profile and the temporary seismic stations used by ANCORP & Oncken (2006) and Bloch et al. (2014). The blue rectangle represents the study area of this work.

A high-resolution velocity image (Figure 20) was developed by Bloch et al. (2014) by combining an extrapolation of the 2-D seismic wide-angle P-wave velocity model along the ANCORP reflectivity profile and the high-precision locations of a few thousand earthquakes calculated using two temporary local seismic network in the Iquique segment around 21°S.

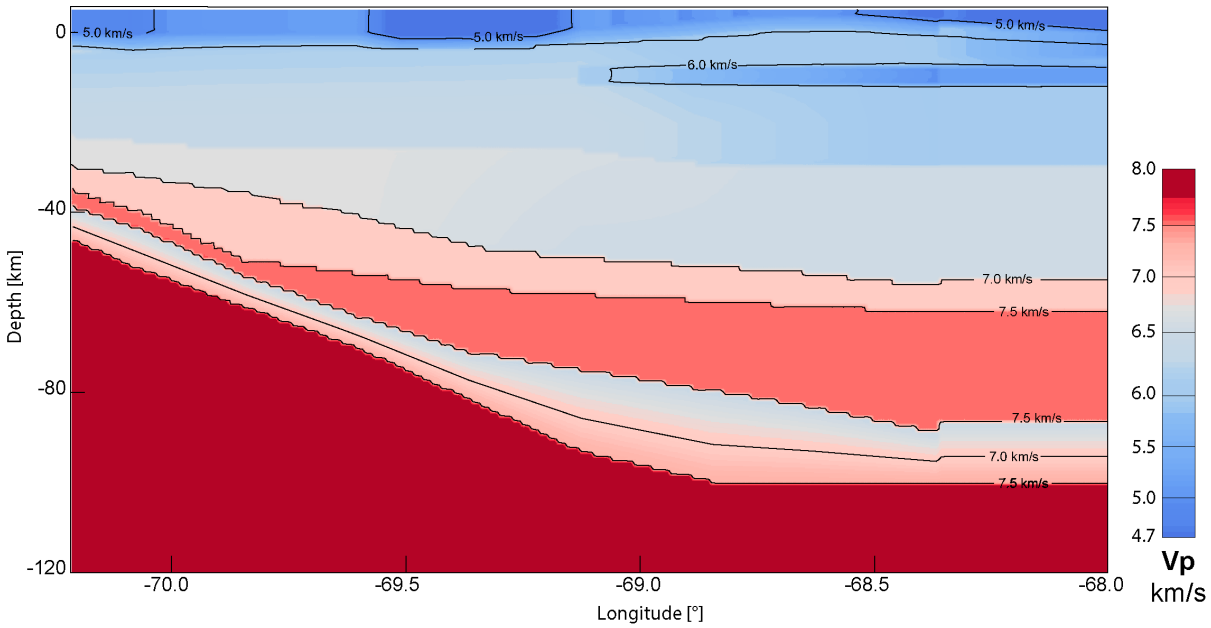

Figure 20: Cross-section P-wave velocity model (modified from Bloch et al, 2014). Red colors represent velocities higher than 7 km/s and blue colors represent velocities below 6 km/s.

The experiments of both ANCORP & Oncken (2006) and Bloch et al. (2014) suggest the prevalence of fluid processes in the subducted oceanic crust. In the continental forearc domain, the mantle has lower than average velocities (7.6 km/s), which indicates heterogeneously hydrated mantle above the downgoing slab. These P-wave velocity values were used in this work to construct the 2-D velocity model.

4. SEISMIC WAVEFORM MODELING

To understand the effects of the topography and sedimentary intramountainous basins on the amplification of seismic waves, simulations of the seismic wave propagation from the 2014 Iquique earthquake sequence in the study region was performed using the Cartesian version of SPECFEM3D, a software package that uses the spectral element method (SEM) to solve the 3-D wave equation at local or regional scales (Komatitsch & Vilotte, 1998; Komatitsch & Tromp, 1999; Komatitsch et al., 2010).

The Spectral Element Method (SEM) is a highly accurate numerical method that uses a mesh of hexahedral finite elements on which the wavefield is represented in terms of high-degree Lagrange polynomials on Gauss–Lobatto–Legendre interpolation points.

The SEM and the SPECFEM3D software have been widely employed to model seismic wave propagation using local, regional, and global velocity models as they combine the flexibility of the finite element method with the accuracy of pseudospectral techniques. The flexibility of the mesh allows the implementation of complex geometries, topography, bathymetry, and basement surfaces with minimal numerical dispersion and with the advantage of traction-free boundary conditions (Faccioli, 1991; Komatitsch et al., 2004, 2010; Komatitsch & Tromp, 1999; Komatitsch & Vilotte, 1998; Lee et al., 2009).

The following sections present further details about the SEM numerical method, the definition of the source as centroid moment tensor parameters, and the numerical implementation used in this work, including the mesh design for the crustal velocity models and the earthquakes studied.

4.1. SPECTRAL ELEMENT METHOD

The SEM is a special formulation of the finite element method (FEM) that has been used for more than 20 years to study 2-D and 3-D seismic wave propagation. The method easily

incorporates free-surface topography and accurately represents the propagation of surface waves.

4.1.1. ELASTIC WAVE EQUATIONS

To determine the displacement field produced by an earthquake in a finite earth model with volume Ω, it is necessary to solve the equation of motion that governs the propagation of seismic waves in an elastic or anelastic media, defining the boundary properties and the internal discontinuities of the earth model, as shown in **Figure 21**. The boundaries of this earth model include a free surface (i.e., stress-free surface) δΩ in which seismic waves are reflected, and an absorbing boundary Γ which completely absorbs the seismic waves to represent an infinite earth. The unit vector outward normal to the boundary δΩ+Γ is denoted by $\hat{\mathbf{n}}$, and the source is located at $\mathbf{x_s}$ (Komatitsch & Tromp, 1999).

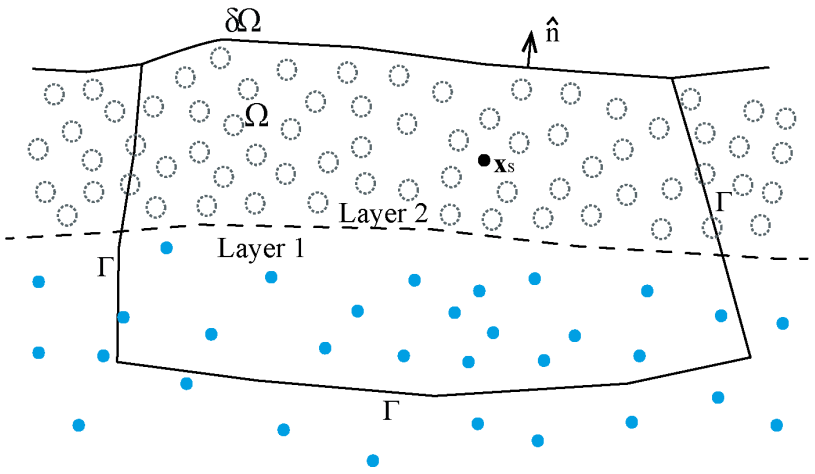

Figure 21: Finite earth model with volume Ω and free surface δΩ, absorbing boundary Γ, and unit outward normal vector $\hat{n}$. The model can be composed of any number of layers, and the source x_s can be placed anywhere inside Ω (modified from Komatitsch & Tromp, 1999).

The displacement field **u** produced by an earthquake is governed by the momentum equation:

$$\rho\ddot{\mathbf{u}} = \nabla \cdot \mathbf{T} + \mathbf{f} \qquad \textbf{(Equation 4.1.1-1)}$$

Where ρ is the density distribution, $\mathbf{f}$ is the point force, and $\mathbf{T}$ is the stress tensor. The stress tensor $\mathbf{T}$ is linearly related to the displacement gradient $\mathbf{\nabla u}$ by Hooke's law (Komatitsch et al., 2010) and can be written in terms of the fourth-order stiffness tensor $\mathbf{C}$, that determines the elastic properties of the earth models, and the symmetric second-order strain tensor $\boldsymbol{\varepsilon}$ as:

$$\mathbf{T} = \mathbf{C} : \boldsymbol{\varepsilon} \qquad \textbf{(Equation 4.1.1-2)}$$

$$\boldsymbol{\varepsilon} = \frac{\mathbf{1}}{\mathbf{2}}[\mathbf{\nabla u} + (\mathbf{\nabla u})^{\mathrm{T}}] \qquad \textbf{(Equation 4.1.1-3)}$$

The point force $\mathbf{f}$ is related to the earthquake source (Komatitsch et al., 1999), which can be represented as an equivalent body force, described by the moment tensor $\mathbf{M}$ as:

$$\mathbf{f} = -\mathbf{\nabla} \cdot \mathbf{M}(t)\delta(\mathbf{x} - \mathbf{x_s}) \qquad \textbf{(Equation 4.1.1-4)}$$

Where $\mathbf{x_s}$ represents the location of the point source and $\delta(\mathbf{x} - \mathbf{x_s})$ represents the Dirac delta distribution located at $\mathbf{x_s}$. The moment tensor $\mathbf{M}$ is a symmetric tensor that has all the properties of a stress tensor, which spherical part carries the information about P waves and the deviatoric part propagates the S and P waves. As the body wave radiation depends linearly on the rate of change of the moment tensor, a simple rise time approximation can be used to define $\mathbf{M}(t)$ as:

$$\mathbf{M}(t) = \mathbf{M}_0 \mathrm{S}(t) \qquad \textbf{(Equation 4.1.1-5)}$$

Where $\mathbf{M}_0$ is the constant moment tensor, which will be defined in the next section, and $\mathrm{S}(t)$ is a source time function.

The boundary conditions are represented by a stress-free condition at the earth's surface $\partial\Omega$, expressed by:

$$\mathbf{T} \cdot \hat{\mathbf{n}} = 0 \qquad \textbf{(Equation 4.1.1-6)}$$

And by the artificial model boundary Γ, where the waves travelling out of the volume Ω need to be absorbed. To approximate the absorbing boundary condition, traction can be written in terms of velocity as:

$$\mathbf{T}\cdot\hat{\mathbf{n}} = \rho[v_n(\hat{\mathbf{n}}\cdot\partial_t\mathbf{u})\hat{n} + v_1(\widehat{\mathbf{t_1}}\cdot\partial_t\mathbf{u})\widehat{t_1} + v_2(\widehat{\mathbf{t_2}}\cdot\partial_t\mathbf{u})\widehat{t_2}] \quad \textbf{(Equation 4.1.1-7)}$$

where $\widehat{\mathbf{t_1}}$ and $\widehat{\mathbf{t_2}}$ are orthogonal unit vectors tangential to the absorbing boundary Γ with unit outward normal vector $\hat{\mathbf{n}}$, v_n is the quasi-P-wave speed of waves polarized in the $\hat{\mathbf{n}}$ direction, v_1 is the quasi-S-wave speed of waves polarized in the $\widehat{\mathbf{t_1}}$ direction, and v_2 is the quasi-S-wave speed of waves polarized in the $\widehat{\mathbf{t_2}}$ direction. At the limits between layers or any other internal boundary, both, the displacement $\mathbf{u}$ and the traction $\mathbf{T}\cdot\hat{\mathbf{n}}$ need to be continuous (Komatitsch & Tromp, 1999).

The equation of motion can be solved based on a strong or a weak formulation of the problem. The strong formulation works directly with the equations and the boundary conditions written in differential form, being used in finite differences and pseudospectral modeling approaches. The weak formulation uses an integral form of the equations of motion, and is generally used in FEM, SEM, and direct solution methods (Komatitsch & Vilotte, 1998).

4.1.2. WEAK FORMULATION

In the weak formulation, the integrated form of the equation of motion **(Equation 4.1.1-1**) can be written as follows by dotting the equation with an arbitrary test function $\mathbf{w}$ and integrating by parts over the model volume Ω, imposing the stress-free boundary condition and the absorbing boundary condition expressed in terms of traction, then:

$$\int_\Omega \mathbf{w}\cdot\rho\ddot{\mathbf{u}}d\Omega = \int_\Omega \mathbf{w}\cdot\nabla\cdot\mathbf{T}\,d\Omega + \int_\Omega \mathbf{w}\cdot\mathbf{f}d\Omega$$

(**Equation 4.1.2-1**)

Integrating by parts:

$$\int_{\Omega} \mathbf{w} \cdot \boldsymbol{\nabla} \cdot \mathbf{T} \; d\Omega = \int_{\Gamma} \; \mathbf{w} \cdot \mathbf{T} \cdot \hat{\mathbf{n}} \; d\Gamma - \int_{\Omega} \boldsymbol{\nabla}\mathbf{w} : \mathbf{T} \, d\Omega$$

(**Equation 4.1.2-2**)

Then:

$$\int_{\Omega} \rho \mathbf{w} \cdot \ddot{\mathbf{u}} \, d\Omega = \int_{\Omega} \mathbf{w} \cdot \mathbf{f} \, d\Omega + \int_{\Gamma} \; \mathbf{w} \cdot \mathbf{T} \cdot \hat{\mathbf{n}} \, d\Gamma - \int_{\Omega} \boldsymbol{\nabla}\mathbf{w} : \mathbf{T} \, d\Omega$$

(**Equation 4.1.2-3**)

Replacing with previous definitions (**Equations 4.1.1-2**, **4.1.1-3**, **4.1.1-4, 4.1.1-6** and **4.1.1-7**)

$$\int_{\Omega} \rho \, \mathbf{w} \cdot \ddot{\mathbf{u}} \, d\Omega \; + \int_{\Omega} \boldsymbol{\nabla}\mathbf{w} : \mathbf{C} : \boldsymbol{\nabla}\mathbf{u} \; d\Omega \; = \; \mathbf{M} : \boldsymbol{\nabla}\mathbf{w}(\mathbf{x_s}) \, S(t)$$

$$+ \int_{\Gamma} \; \rho[v_n(\hat{\mathbf{n}} \cdot \partial_t \mathbf{u})\hat{\mathbf{n}} + v_1(\hat{\mathbf{t_1}} \cdot \partial_t \mathbf{u})\hat{\mathbf{t_1}} + v_2(\hat{\mathbf{t_2}} \cdot \partial_t \mathbf{u})\hat{\mathbf{t_2}}] \cdot \mathbf{w} d\Gamma$$

(**Equation 4.1.2-4**)

The **Equation 4.1.2-4** defines the seismic wave equation in a weak, i.e. variational form where the source term $\int_{\Omega} \; \mathbf{w} \cdot \mathbf{f} \, d\Omega$, has been explicitly integrated using the properties of the Dirac delta distribution (Komatitsch & Tromp, 1999). This mathematical weak formulation of the displacement field generated by a point source located at $\mathrm{x_s}$ in the volume shown in **Figure 21** can be solved as in a classical FEM by subdividing the model volume Ω into a number of non-overlapping elements $\Omega_{\mathbf{e}}$.

4.1.3. SPATIAL DISCRETIZATION

As in the classical FEM, the volume Ω is subdivided into non-overlapping elements Ω_e, $e = 1, \dots, n_e$, as shown in **Figure 22**, and the boundary Γ is also subdivided into surface elements Γ_b, $b = 1, \dots, n_b$.

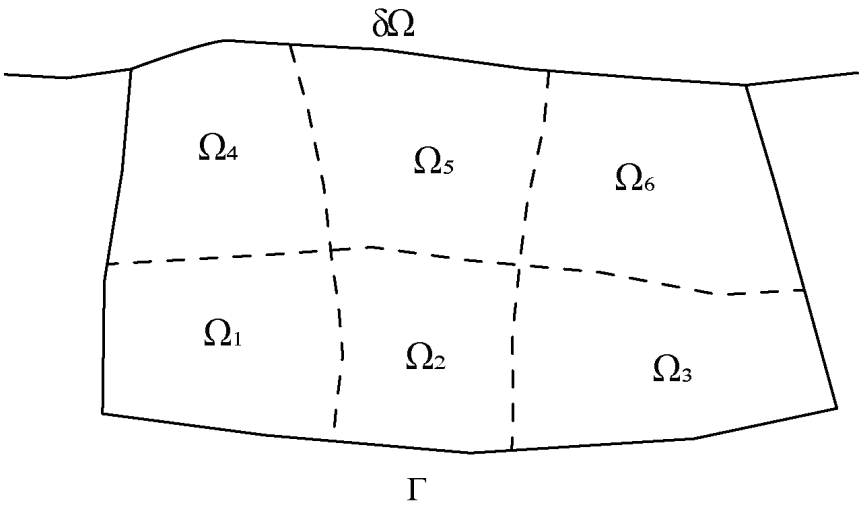

Figure 22: Subdivision of the earth model into elements with volume Ω and free surface δΩ shown in Figure 20 (modified from Komatitsch & Tromp, 1999).

In SEM the elements are restricted to hexahedral volume elements Ω_e, therefore the absorbing boundary is subdivided in quadrilateral surface elements Γ_b.

BOUNDARY ELEMENTS

Each quadrilateral boundary element can be defined in terms of a square in a local coordinate system, called natural coordinates, whose points are denoted by the vector (ξ, η), $-1 \leq \xi \leq 1$, $-1 \leq \eta \leq 1$; meanwhile, the boundary surface Γ_b is defined in terms of a set of n_a control points $x_a = x(\xi_a, \eta_a)$ and a set of n_a shape functions $N_a(\xi, \eta)$. For a simple boundary element with straight edges, four control points are used for anchors, but for curved boundary elements nine control points may be needed to describe their shape accurately (**Figure 23**).

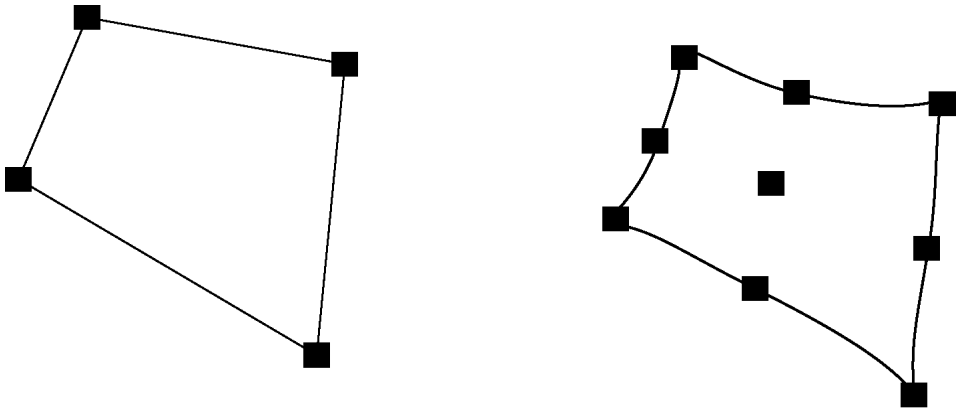

Figure 23: Geometry of any quadrangle surface can be defined by four control nodes or nine control nodes (modified from Komatitsch & Tromp, 1999).

For any boundary surface, the relation between a point **x** within the element Γ_b and a point (ξ, η) in the reference system may be written as follows:

$$\mathbf{x}(\xi,\eta) = \sum_{a=1}^{n_a} N_a(\xi,\eta)\mathbf{x}_a \qquad \textbf{(Equation 4.1.3-1)}$$

The shape functions $N_a(\xi, \eta)$ are products of Lagrange polynomials of degree 1 or 2. The $n_l + 1$ Lagrange polynomials of degree n_l are defined in terms of $n_l + 1$ control points $-1 \leq \xi_\alpha \leq 1, \alpha = 0, \ldots, n_l$ as follows:

$$l_\alpha^{n_l}(\xi) = \frac{(\xi-\xi_0)\cdots(\xi-\xi_{\alpha-1})(\xi-\xi_{\alpha+1})\cdots(\xi-\xi_{n_l})}{(\xi_\alpha-\xi_0)\cdots(\xi_\alpha-\xi_{\alpha-1})(\xi_\alpha-\xi_{\alpha+1})\cdots\left(\xi_\alpha-\xi_{n_l}\right)} \qquad \textbf{(Equation 4.1.3-2)}$$

From this definition, when the Lagrange polynomials are evaluated at a control point ξ_β, they return a value of 0 or 1, $l_\alpha^{n_l}(\xi_\beta) = \delta_{\alpha\beta}$ where δ is the Kronecker delta. The orientation of the reference square is chosen such that the unit outward normal vector $\hat{n}$ to the boundary element Γ_b is given by:

$$\hat{\mathbf{n}} = \frac{1}{J_b}\frac{\partial \mathbf{x}}{\partial \xi} \times \frac{\partial \mathbf{x}}{\partial \eta} \qquad \textbf{(Equation 4.1.3-3)}$$

where J_b is the Jacobian of the transformation, given by:

$$J_b = \left\| \frac{\partial \mathbf{x}}{\partial \xi} \times \frac{\partial \mathbf{x}}{\partial \eta} \right\| \qquad \textbf{(Equation 4.1.3-4)}$$

To calculate the Jacobian J_b and the unit onward normal vector $\hat{n}$, the six partial derivatives $\partial x/\partial \xi$ and $\partial x/\partial \eta$ must be calculated in terms of the shape functions as follows:

$$\partial_\xi \mathbf{x}(\xi, \eta) = \sum_{a=1}^{n_a} \partial_\xi N_a(\xi, \eta)\mathbf{x}_a$$

$$\partial_\eta \mathbf{x}(\xi, \eta) = \sum_{a=1}^{n_a} \partial_\eta N_a(\xi, \eta)\mathbf{x}_a \qquad \textbf{(Equation 4.1.3-5)}$$

The partial derivatives of the shape functions $\partial_\xi N_a$ and $\partial_\eta N_a$ are analytically determined in terms of Lagrange polynomials.

VOLUME ELEMENTS

In the same way that for boundary elements, each hexahedral volume element Ω_e can be defined in terms of a cube in the local reference coordinate system, in which the points are denoted by the vector $\xi = (\xi, \eta, \zeta)$, where $-1 \leq \xi \leq 1$, $-1 \leq \eta \leq 1$ and $-1 \leq \zeta \leq 1$. Each volume element is defined in terms of a set of n_a control points $\mathbf{x_a} = \mathbf{x}(\xi_a, \eta_a, \zeta_a)$ and a set of n_a shape functions $N_a(\xi, \eta, \zeta)$. At least eight corner nodes are needed to define a hexahedral volume element and by adding mid-side and center nodes the number of anchors increases at twenty-seven nodes **Figure 24**.

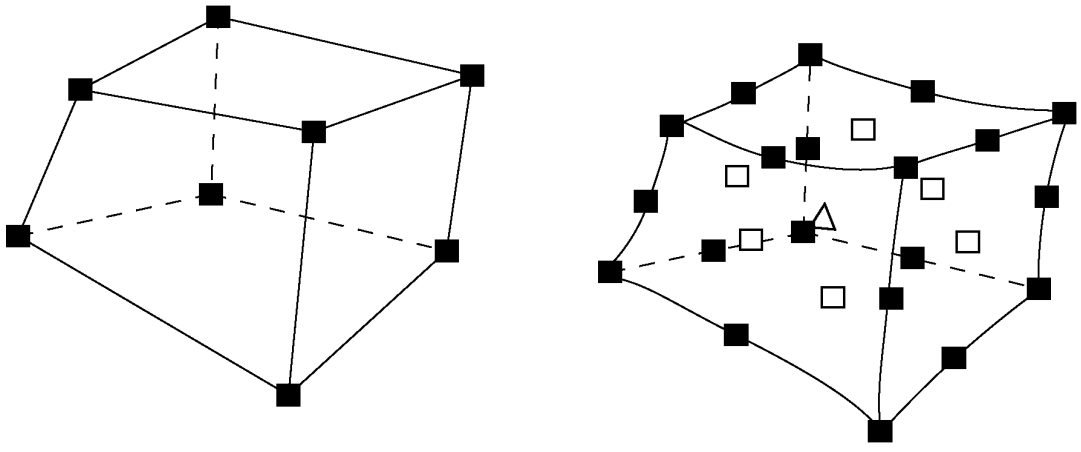

Figure 24: Geometry of any volume hexahedra can be defined by eight control nodes or twenty-seven control nodes. In the case of twenty-seven node brick, the empty squares indicate the six nodes that lie in the middle of the sides of the element, and the triangle indicates the node that lies at the center of the element (modified from Komatitsch & Tromp, 1999).

The relation between a point within the hexahedral element and the reference cube may be written as:

$$\mathbf{x}(\boldsymbol{\xi}) = \sum_{a=1}^{n_a} N_a(\boldsymbol{\xi})\mathbf{x}_a \qquad \textbf{(Equation 4.1.3-6)}$$

Shape functions of eight-node hexahedral elements are triple products of degree 1 Lagrange polynomials, and those of twenty-seven-node hexahedral elements are triple products of degree 2 Lagrange polynomials. An element of volume dxdydz within a given element Ω_e is related to an element of volume dξdηdζ in the reference cube by:

$$\mathrm{dxdydz} = J_e \mathrm{d}\xi\mathrm{d}\eta\mathrm{d}\zeta \qquad \textbf{(Equation 4.1.3-7)}$$

Where the volumetric Jacobian J_e is given by:

$$J_e = \left|\frac{\partial(\mathrm{x,y,z})}{\partial(\xi,\eta,\zeta)}\right| \qquad \textbf{(Equation 4.1.3-8)}$$

The components of which, in terms of the shape functions, are given by the partial derivative of the matrix $\partial\mathbf{x}/\partial\xi$ as follows:

$$\frac{\partial \mathbf{x}}{\partial \xi} = \sum_{\mathrm{a=1}}^{\mathrm{n_a}} \frac{\partial \mathrm{N_a}}{\partial \xi}\mathbf{x}_\mathrm{a} \qquad \textbf{(Equation 4.1.3-9)}$$

The partial derivatives of the shape functions are determined analytically in terms of Lagrange polynomials of degree 1 or 2 and their derivatives.

The superficial and volume elements should be constructed in such a way that the Jacobian J_e never vanishes; imposing important restrictions on the mesh generation process to ensure that the mapping of the element $\mathbf{x}(\xi)$ in the reference system $\xi(\mathbf{x})$ is unique and invertible.

Therefore, to solve the weak form of the equation of motion (**Equation 4.1.2-4**), integrations over the volume Ω and the absorbing boundary Γ are subdivided in terms of smaller integrals over the volume and surface elements $\Omega_e$and Γ_b, respectively. It is been showed that the shape of the boundary and volume elements can be defined in terms of low-degree Lagrange polynomials, that for the SEM formulation, higher-degree Lagrange interpolant are used to express functions on the elements. The control points ξ_α, $\alpha = 0, \dots, n_l$, needed in the definition of the Lagrange polynomials of degree n_l are chosen to be the $n_l + 1$ Gauss-Lobatto-Legendre points, which are roots of $(1 - \xi^2)P'_{n_l}(\xi) = 0$, where P'_{n_l} is the derivative of the Legendre polynomial of degree n_l. These Gauss-Lobatto-Legendre points can be computed by the numerical resolution of the roots (Komatitsch & Tromp, 1999).

Functions f that represent the physical unknowns on an element are interpolated in terms of triple products of Lagrange polynomials of degree n as:

$$f(\mathbf{x}(\xi,\eta,\zeta)) \approx \sum_{\alpha,\beta,\gamma=0}^{n_\alpha,n_\beta,n_\gamma} f^{\alpha\beta\gamma} l_\alpha(\xi) l_\beta(\eta)\, l_\gamma(\zeta) \qquad \textbf{(Equation 4.1.3-10)}$$

Where $f^{\alpha\beta\gamma} = f(\mathbf{x}(\xi_\alpha,\eta_\beta,\zeta_\gamma))$ is the value of the function f at the Gauss-Lobatto-Legendre point $\mathbf{x}(\xi_\alpha,\eta_\beta,\zeta_\gamma)$. The gradient of the function, $\nabla f = \sum_{i=1}^{3} \hat{\mathbf{x}}_i \partial_i f$ evaluated at the Gauss-Lobatto-Legendre point can be written as (Komatitsch et al., 2010):

$$\nabla f\left(\mathbf{x}(\xi_{\alpha'}, \eta_{\beta'}, \zeta_{\gamma'})\right)$$

$$\approx \sum_{i=1}^{3} \hat{\mathbf{x}}_i \left[(\partial_i \xi)^{\alpha'\beta'\gamma'} \sum_{\alpha=1}^{n_\alpha} f^{\alpha\beta'\gamma'} \, l'_{\alpha}(\xi_{\alpha'}) + (\partial_i \eta)^{\alpha'\beta'\gamma'} \sum_{\beta=0}^{n_\beta} f^{\alpha'\beta\gamma'} \, l'_{\beta}(\eta_{\beta'}) \right.$$

$$\left. + (\partial_i \zeta)^{\alpha'\beta'\gamma'} \sum_{\gamma=0}^{n_\gamma} f^{\alpha'\beta'\gamma} \, l'_{\gamma}(\zeta_{\gamma'}) \right]$$

(Equation 4.1.3-11)

Here $\hat{\mathbf{x}}_i, i = 1,2,3$ is a unit vector in the direction of increasing x, y, and z, respectively, and $\partial_i, i = 1,2,3$ are the partial derivatives in those directions. Therefore, integrations over surface elements Γ_b and volume elements Ω_e may be approximated using the Gauss-Lobatto-Legendre integration rule as:

$$\int_{\Gamma_b} f(\mathbf{x}) d^2\mathbf{x} = \int_{-1}^{1}\int_{-1}^{1} f\left(\mathbf{x}(\xi,\eta)\right) J_b(\xi,\eta) d\xi d\eta \approx \sum_{\alpha,\beta=0}^{n_l} \omega_\alpha \omega_\beta f^{\alpha\beta} J_b{}^{\alpha\beta}$$

$$\int_{\Omega_e} f(\mathbf{x}) d^3\mathbf{x} = \int_{-1}^{1}\int_{-1}^{1}\int_{-1}^{1} f\left(\mathbf{x}(\xi,\eta,\zeta)\right) J_e(\xi,\eta,\zeta) d\xi d\eta d\zeta \approx \sum_{\alpha,\beta,\gamma=0}^{n_\alpha,n_\beta,n_\gamma} \omega_\alpha \omega_\beta \omega_\gamma f^{\alpha\beta\gamma} J_e^{\alpha\beta\gamma}$$

(Equation 4.1.3-12)

Where $J_b^{\alpha\beta} = J_b\left(\xi_\alpha, \eta_\beta\right)$ and $J_e^{\alpha\beta\gamma} = J_e(\xi_\alpha, \eta_\beta, \zeta_\gamma)$ and $\omega_\alpha > 0$, for $\alpha = 0, \ldots, n$ correspond the weights associated with the Gauss-Lobatto-Legendre quadrature. To facilitate the integration of functions and their partial derivatives over the elements, the values of the inverse Jacobian matrix $\partial\xi/\partial\mathbf{x}$ need to be determined at the $(n_l + 1)^3$ Gauss-Lobatto-Legendre integration points for each element.

To distinguish between the grid points that define an element in the local mesh and all the other grid points in the global mesh (many of which are shared among several elements), a relationship between the grid points is defined using efficient modeling routines, as the contributions from all the elements that share a common global grid point need to be counted. This process is usually known as assembly. Computationally, the assembly process is an expensive and time-consuming part of the calculation as the information from individual elements needs to be shared with neighboring elements, involving the parallelization of the calculations and communications between CPUs (Komatitsch & Vilotte, 1998).

If U represents the displacement vector for the global system, which contains the displacement vector in all the grid points in the global mesh, the ordinary differential equation that governs the time dependence of the global systems can be written as:

$$M\ddot{U} + C\dot{U} + KU = F \qquad \textbf{(Equation 4.1.3-13)}$$

Where M is the global mass matrix, C is the global absorbing boundary matrix, K is the global stiffness matrix, and F is the source. Therefore, by solving the equation of motion at the elemental level through the weak formulation and introducing the Gauss–Lobatto–Legendre numerical integration, the global displacement field is obtained after assembling the system (Komatitsch & Tromp, 1999).

A highly desirable property which significantly reduces the complexity and cost of the algorithm is the construction of a diagonal mass matrix M. Additionally, the density ρ does not need to be constant over the element, and can vary from one grid point to another, which allows fully heterogeneous media to be modeled. The SEM combines the geometric flexibility of the FEM with the fast convergence derived from the good stability and approximation properties of the polynomial spaces and the accuracy associated with the Gauss–Lobatto–Legendre quadrature

and interpolation (Komatitsch et al., 1999; Komatitsch & Tromp, 1999; Komatitsch & Vilotte, 1998).

4.1.4. TIME DISCRETIZATION

The time discretization of the second-order ordinary differential equation **(Equation 4.1.3-13)** is defined by a time interval Δt and a classical second-order finite difference solution by introducing the three control parameters α, β, and γ as follows:

$$\frac{1}{\Delta t} M[\mathbf{v}_{n+1} - \mathbf{v}_n] = F^{\text{ext}}_{n+\alpha} - F^{\text{int}}\left(\mathbf{u}^h_{n+\alpha}, \mathbf{v}^h_{n+\alpha}\right) \qquad \textbf{(Equation 4.1.4-1)}$$

$$\mathbf{u}_{n+1} = \mathbf{u}_n + \Delta t\left[\left(1 - \frac{\beta}{\gamma}\right)\mathbf{v}_n + \frac{\beta}{\gamma}\mathbf{v}_{n+1}\right] + \Delta t^2\left(\frac{1}{2} - \frac{\beta}{\gamma}\right)\mathbf{a}_n \qquad \textbf{(Equation 4.1.4-2)}$$

$$\mathbf{a}_{n+1} = \frac{1}{\gamma \Delta t}[\mathbf{v}_{n+1} - \mathbf{v}_n] + \left(1 - \frac{1}{\gamma}\right)\mathbf{a}_n \qquad \textbf{(Equation 4.1.4-3)}$$

Where $\mathbf{u}_{n+\alpha} \doteq \alpha \mathbf{u}_{n+1} + (1-\alpha)\mathbf{u}_n$ and $\mathbf{F}^{\text{ext}}_{n+\alpha} \doteq \alpha \mathbf{F}^{\text{ext}}_{n+1} + (1-\alpha)\mathbf{F}^{\text{ext}}_n$. It has been shown that for $\alpha = \beta/\gamma = 1/2$ this energy-momentum method exactly preserves the total energy and linear and angular momenta. This Newmark-type scheme can be generalized to a predictor-multicorrector format that allows an efficient parallelization and is conditionally stable, as the Courant stability condition is governed by the minimum value of the ratio between the size of the grid cells and the P-wave velocity (Komatitsch et al., 1999; Komatitsch & Tromp, 1999).

The second-order iterative scheme is summarized as:

$i = 0$ (i is the iteration number)

Predictor phase:

$$\mathbf{u}_{n+1}^{(i)} = \tilde{\mathbf{u}}_{n+1} \quad \mathbf{v}_{n+1}^{(i)} = 0 \quad \mathbf{a}_{n+1}^{(i)} = \tilde{\mathbf{a}}_{n+1} \qquad \textbf{(Equation 4.1.4-4)}$$

Solution phase:

$$\frac{1}{\Delta t} M \Delta \mathbf{v}^{(i)} = F_{n+\alpha}^{\text{ext}} - F^{\text{int}}\left(\mathbf{u}_{n+\alpha}^{h}, \mathbf{v}_{n+\alpha}^{h}\right) - \frac{1}{\Delta t} M \left[\mathbf{v}_{n+1}^{(i)} - \mathbf{v}_{n}\right] \textbf{(Equation 4.1.4-5)}$$

Corrector phase:

$$\mathbf{v}_{n+1}^{(i+1)} = \mathbf{v}_{n+1}^{(i)} + \Delta \mathbf{v}$$

$$\mathbf{u}_{n+1}^{(i+1)} = \tilde{\mathbf{u}}_{n+1} + \frac{\beta \Delta t}{\gamma} \Delta \mathbf{v}_{n+1}^{(i+1)}$$

$$\mathbf{a}_{n+1}^{(i+1)} = \tilde{\mathbf{a}}_{n+1} - \frac{1}{\gamma \Delta t} \Delta \mathbf{v}_{n+1}^{(i+1)} \qquad \textbf{(Equation 4.1.4-6)}$$

Where the predictors are defined as:

$$\tilde{\mathbf{u}}_{n+1} = \mathbf{u}_{n} + \Delta t \left(1 - \frac{\beta}{\gamma}\right) \mathbf{v}_{n} + \Delta t^{2} \left(\frac{1}{2} - \frac{\beta}{\gamma}\right) \mathbf{a}_{n} \qquad \textbf{(Equation 4.1.4-7)}$$

$$\tilde{\mathbf{a}}_{n+1} = \left(1 - \frac{1}{\gamma}\right) \mathbf{a}_{n} - \frac{1}{\gamma \Delta t} \mathbf{v}_{n} \qquad \textbf{(Equation 4.1.4-8)}$$

4.2. MOMENT TENSOR

In the previous section, the numerical implementation of the spectral element method was developed. In this implementation, the point source that represents the earthquake is written in terms of the seismic moment tensor **M**. The definition of the seismic moment tensor is derived from the source mechanism theory, in which earthquakes are seen as fractures or dislocations in an elastic medium, and which represents a quantity that depends on the source strength, elastic properties, slip, and fault orientation and characterizes all the information about the source that can be obtained from observing seismic waves at the earth's surface (Aki & Richards, 1980; Udías & Mezcua, 1997).

When observing waves with wavelengths much longer than the linear dimension of the source, the source can be effectively approximated as a point with an associated radiation pattern. For sources of finite extent, the seismic moment tensor can be defined as a moment density tensor **m** per unit of volume or unit surface. For a dislocation with slip Δu on a surface defined by the normal vector n, the components of the moment density tensor can be defined as:

$$\mathbf{m}_{ij} \equiv C_{ijkl}\Delta u_k n_l \qquad \textbf{(Equation 4.2-1)}$$

Where C_{ijkl} corresponds to the fourth-order tensor of the elastic coefficients of the medium, which in the case of an isotropic medium C is symmetric and involves only the two independent Lamé constants λ and μ, as follows (e.g. Aki & Richards, 1980):

$$C_{ijkl} = \lambda\delta_{ij}\delta_{kl} + \mu(\delta_{ik}\delta_{jl} + \delta_{il}\delta_{jk}) \qquad \textbf{(Equation 4.2-2)}$$

In terms of this symmetric tensor, which is time dependent, the representation theorem for the displacement at **x** due to a general displacement discontinuity across a surface S is:

$$u_i(\mathbf{x}, t) = \iint_S m_{kj} * G_{ik,j} dS$$

(Equation 4.2-3)

where G is the Green function of the medium, which depends on the elastic coefficients and density and describes how the medium reacts mechanically to an impulse.

For a point source, the representation theorem can be written simply as:

$$u_i(\mathbf{x}, t) = M_{ij} * G_{ik,j} \quad \textbf{(Equation 4.2-4)}$$

Where the moment tensor components are:

$$M_{ij} = \iint_S m_{ij} dS = \iint_S C_{ijkl} \Delta u_k n_l \, dS$$

(Equation 4.2-5)

Since the elastic displacements are linear functions of the components of the moment tensor, as shown in **Equations 4.2-3** and **4.2-4**, in practice, these components can be obtained for sources that have a body-force equivalent given by couples alone, including geological faults (shearing) and explosions (expansion), by the linear inversion of observations of displacements at seismic stations (Aki & Richards, 1980).

4.3. MODEL IMPLEMENTATION

4.3.1. MESH DESIGN

This study used a mesh with a width of 145 km (EW), a length of 200 km (NS), and a depth of 60 km, ranging from 19.25–21.05°S and from 69.45–70.85°W. The number of elements in each side of the mesh is 320 in both horizontal directions and 100 in the depth direction; therefore, the element size varies between 453 meters and 679 meters. Stacey absorbing conditions were used for the four vertical faces and for the bottom face of the grid in order to simulate a semi-infinite regional medium of elastic elements, while a free-surface condition is imposed at the top of the grid (Komatitsch & Tromp, 1999). The sampling interval was set at 0.005 sec and the maximum resolvable frequency was 3.5 Hz, as roughly five points per wavelength are needed to correctly sample the wavefield in SEM. The computations were performed on the UK's national supercomputing facility ARCHER (Advanced Research Computing High End Resource) using parallel programming that distributes the 320 mesh slices over 20 processors for each coordinate axis, using a total of 400 processors for a total of approximately 12,288,000 elements. Each simulation had duration of approximately five hours on ARCHER, producing 2 minutes of wave propagation, with a total of 24,000 time steps.

In order to investigate the separate effects of topography and basins on seismic wave amplification in the study region, three different earth models were performed to simulate the seismic wave propagation, namely a flat model, a topographic model, and a basin model, all of them using the 1-D velocity model described in Section 3.3.1. To observe the effect produced by the velocity model, a fourth model was also implemented, namely a 2-D velocity model with topography using the P-wave velocity model described in Section 3.3.2. The four models are described as follows:

i. Flat model: a model with neither topography nor basins using the 1-D velocity model described in Section 3.3.1.

ii. Topography model: the topography model uses a Shuttle Radar Topography Mission (SRTM) digital elevation model (DEM) (Becker at all, 2009) for the study region with a 90 m resolution in the surface of the grid. However, since the spacing of the mesh (which has element lengths between 453 and 679 m) is coarser than the resolution of the DEM, the topography was smoothed when building the mesh (λ~450 m). Despite the smoothing of the topography, the important features are preserved, such as the coastal cliff, as is shown in the EW profiles in **Figure 26**. **Figure 25(a)** shows the computed tridimensional topographic model.

iii. Basin with topography model: two cuboids with different sizes are added to the topographic model. These two cuboids represent the Alto Hospicio (AH) and the northern part of the Pampa del Tamarugal (PT) basin, with density, Vp, and Vs values related to sedimentary geological units (Dentith & Mudge, 2014; Teldford et al., 1990). The geometry of the basins was obtained from previous studies as was presented in sections 3.1 and 3.2, which constrained the extension and depth of the sedimentary deposits filling the basins using geological, stratigraphic, and geophysical data. **Table 4** shows the geometric parameters that were used to simulate the basins in the mesh, in which the AH basin (the smaller basin) is located in the middle of the mesh next to the coastal cliff, whereas for the larger PT basin, only the northern part is located in the mesh (upper right part). The implementation of just the northern part of the PT basin was performed to understand the border effects of the basin and their interaction with the topography. **Figure 25(b)** shows the tridimensional basin model.

Table 4: Parameters of the Alto Hospicio (AH) and Pampa del Tamarugal (PT) basins.

Basin	Density (kg/m^3)	Vp (m/s)	Vs (m/s)	Length (m)	Width (m)	Depth (m)
AH	2400	3800	2500	8000	2000	500
PT	2400	3800	2500	105,000	50,000	1000

iv. 2-D velocity model: this model uses the 2-D P-wave velocity model described in Section 3.3.2 and interpolates the S-wave velocity and density values from the 1-D velocity model explained in Section **3.3.1**. As the EW 2-D profile starts at 70.15°W and the mesh starts at 70.85°W, the P-wave velocity, S-wave velocity, and density values were simply extended to the west, repeating the first value of the grid. The tridimensional 2-D velocity model is shown in **Figure 25(c)**.

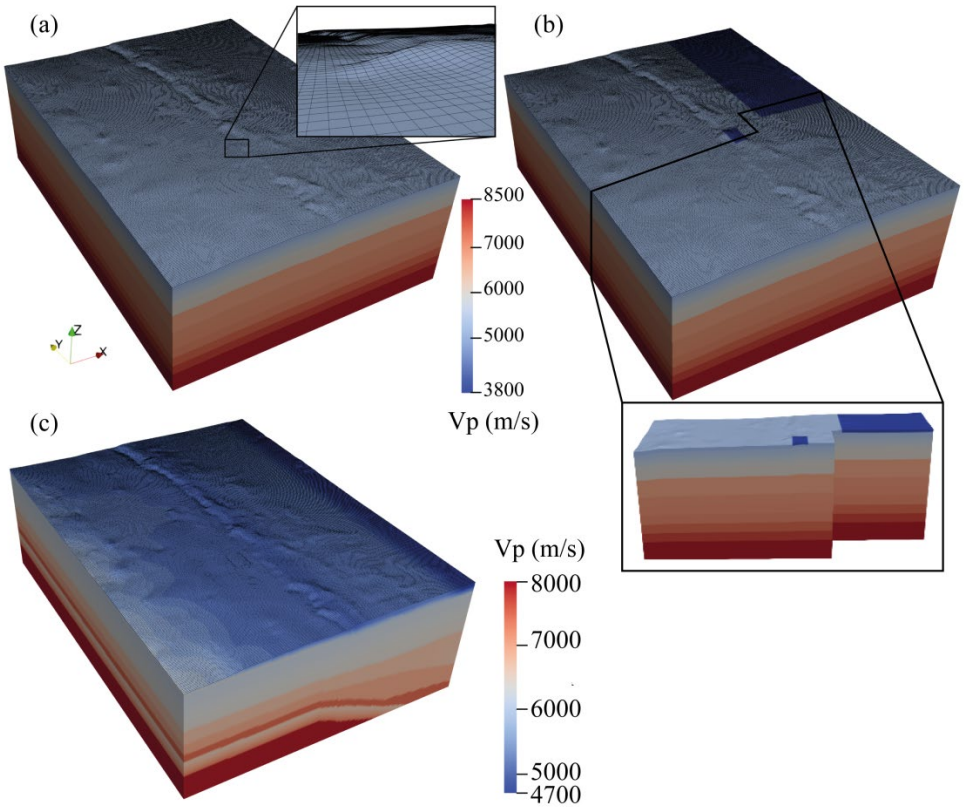

Figure 25: 3-D view of the mesh used in this study, which is 200 km in length, 145 km in width, and 60 km in depth. The P-wave velocity values which were implemented are also shown. (a) 1-D velocity model for Vp ranging from 3800 to 8500 m/s with topography. (b) 1-D velocity model with topography and basins, with Vp ranging from 3800 to 8500 m/s. The two considered basins are shown in dark blue: the smaller Alto Hospicio basin (8 km in length, 2 km in width, and 500 m in depth) and the northern part of the larger Pampa del Tamarugal basin (105 km in length, 50 km in width, and 1000 m in depth). (c) 2-D velocity model with topography, with Vp ranging from 4700 to 8000 m/s.

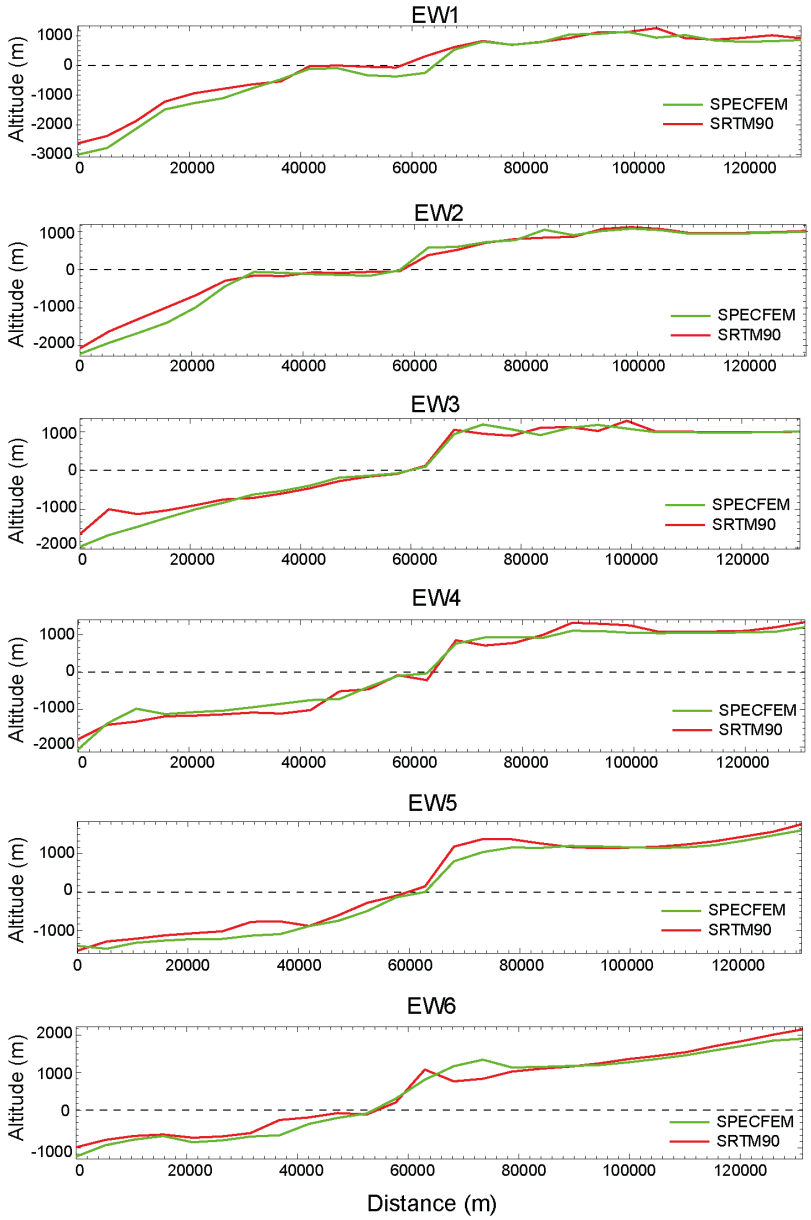

Figure 26: East-west cross-section topographic profiles comparing the topographies obtained from the SPECFEM and SRTM 90 models. The locations of the profiles are shown in Figure 27.

4.3.2. SOURCE PARAMETERS

In this work, Centroid Moment Tensor (CMT) parameters were used to represent point source earthquakes. The parameters consisted of the location of the earthquake in terms of latitude, longitude, and depth of the source, and the six components of the moment tensor.

This information was obtained from the study of León-Ríos (2015), who localized 210 events with local magnitude greater than or equal to 4.5 observed between March and July of 2014 for the Iquique earthquake sequence, and obtained the focal mechanism solutions for 150 earthquakes from the inversion of the seismic moment.

From this extensive catalogue, three earthquakes were simulated, one of them to validate the 1-D velocity model and the other two, with focal mechanisms similar to the Iquique earthquake mainshock, to observe the effects of the topographic, basins, and 2-D velocity models. The source parameters and hypocentral locations of the selected earthquakes are shown in **Table 5** and their locations and focal mechanisms are shown in the map in **Figure 27.**

Table 5: Parameters of the earthquakes used in this study.

Date	Earthquake ID	Location			Focal Mechanism			
		Lat [°]	Lon [°]	Depth [km]	Mw	Strike [°]	Dip [°]	Rake [°]
2014-04-02	20140402070345	−20.14	−70.15	49	4.5	350	30	95
2014-07-13	20140713205414	−20.25	−70.36	34	5.4	140	55	80
2014-04-15	20140415162116	−20.20	−70.87	8	5.0	70	45	75

The validation earthquake was selected in order to compare synthetic waveforms obtained with the SPECFEM 1-D velocity flat model, the synthetic waveforms from the computed regional moment tensor obtained by León-Ríos et al. (2016), and the real data.

The two events simulated for the observation of the effects of the topography, basins, and the 2-D velocity model correspond to earthquakes with focal mechanisms that are very similar to that of the Iquique earthquake mainshock but with smaller magnitudes of Mw 5.4 and Mw 4.5. These magnitudes were selected to avoid the extended source complexity effects which are associated with larger earthquakes while ensuring a good signal-to-noise ratio of the observed waveforms.

Figure 27 also shows the locations of the stations for which synthetic seismograms were computed, some of them coinciding with the locations of real seismic stations (red triangles). As the number of stations used in the SEM simulations does not increase their computational cost, synthetic seismograms for hypothetical stations (blue and yellow triangles) were also included in the computations. The synthetic stations in blue represent stations which were situated at the same latitude as a real seismic station and were positioned at various longitudes to allow a west–east profile to be constructed, whereas the synthetic stations in yellow were used to increase the spatial coverage across the mesh with widespread synthetic profiles.

Figure 27: SRTM topographic map (Becker at all, 2009) of the study area in WGS84 datum 19S including the focal mechanisms (León-Rios, 2015) of the two modeled aftershock earthquakes and the validation earthquake (red beach balls) and the locations of real seismic stations in the region (red inverted triangles) as well as hypothetical stations (blue and yellow inverted triangles) aligned along lines of constant latitude.

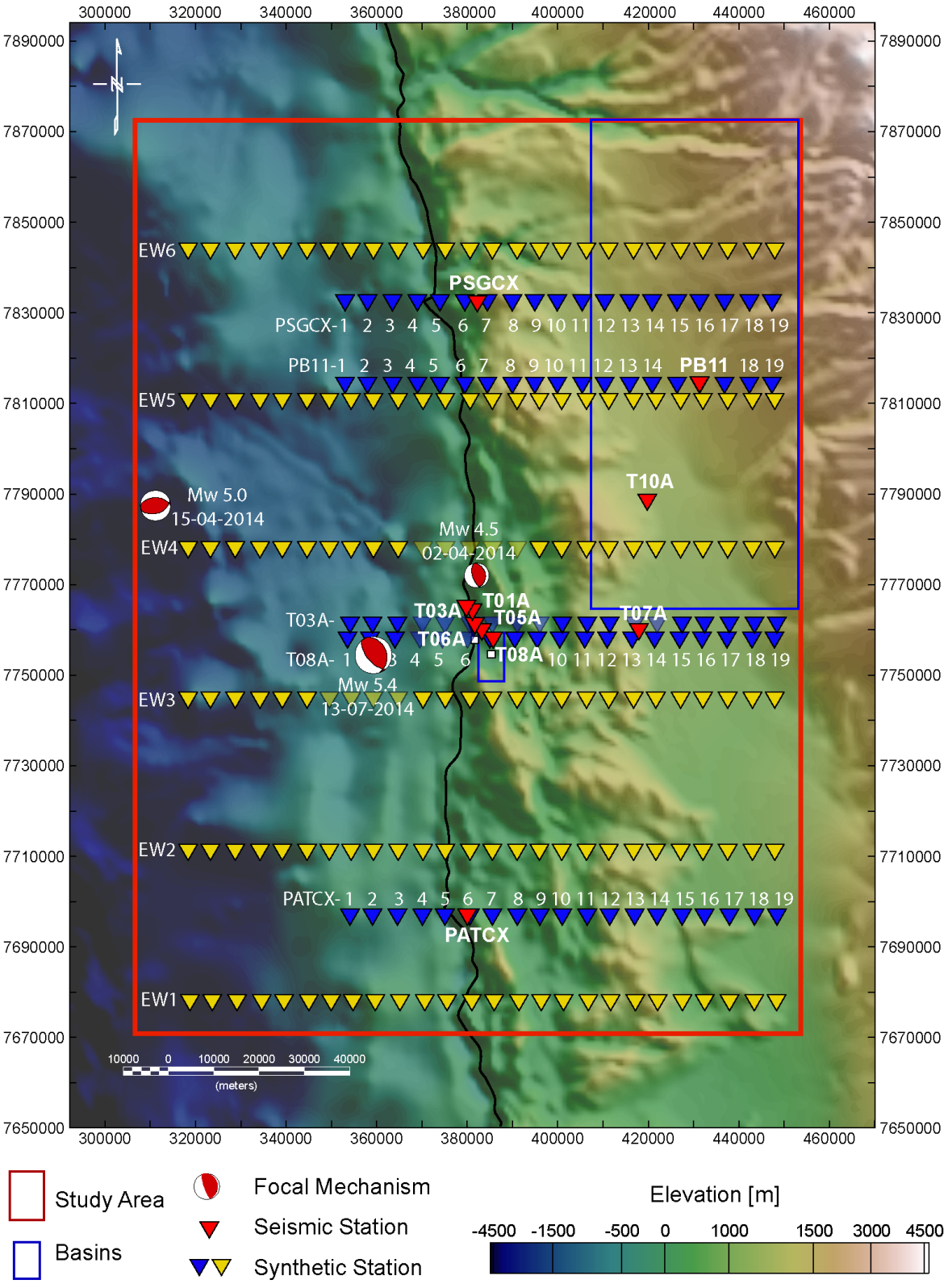
300000
320000
340000
360000
380000
400000
420000
440000
460000
7890000
7870000
7850000
7830000
7810000
7790000
7770000
7750000
7730000
7710000
7690000
7670000
7650000
N
EW6
PSGCX
PSGCX-1 2 3 4 5 6 7 8 9 10 11 12 13 14 15 16 17 18 19
PB11-1 2 3 4 5 6 7 8 9 10 11 12 13 14 PB11 18 19
EW5
T10A
Mw 5.0
15-04-2014
Mw 4.5
02-04-2014
EW4
T01A
T03A
T05A
T07A
T03A-
T06A
T08A
T08A- 1 3 4 5 6 10 11 12 13 14 15 16 17 18 19
Mw 5.4
13-07-2014
EW3
EW2
PATCX-1 2 3 4 5 6 7 8 9 10 11 12 13 14 15 16 17 18 19
PATCX
EW1
10000 0 10000 20000 30000 40000
(meters)
Study Area
Basins
Focal Mechanism
Seismic Station
Synthetic Station
Elevation [m]
-4500 -1500 -500 0 1000 1500 3000 4500

4.4. VALIDATION FOR THE 1-D MODEL

To demonstrate that the 1-D velocity model of the study area is able to reproduce the ground motion generated by the seismic waves during an earthquake, a preliminary validation was performed. This validation consisted of a comparison of the synthetic waveforms and the real seismic data for the 15 April 2015 Mw 5.0 earthquake presented by León-Ríos et al. (2016) and the synthetic waveforms obtained with the flat 1-D velocity model computed with SPECFEM.

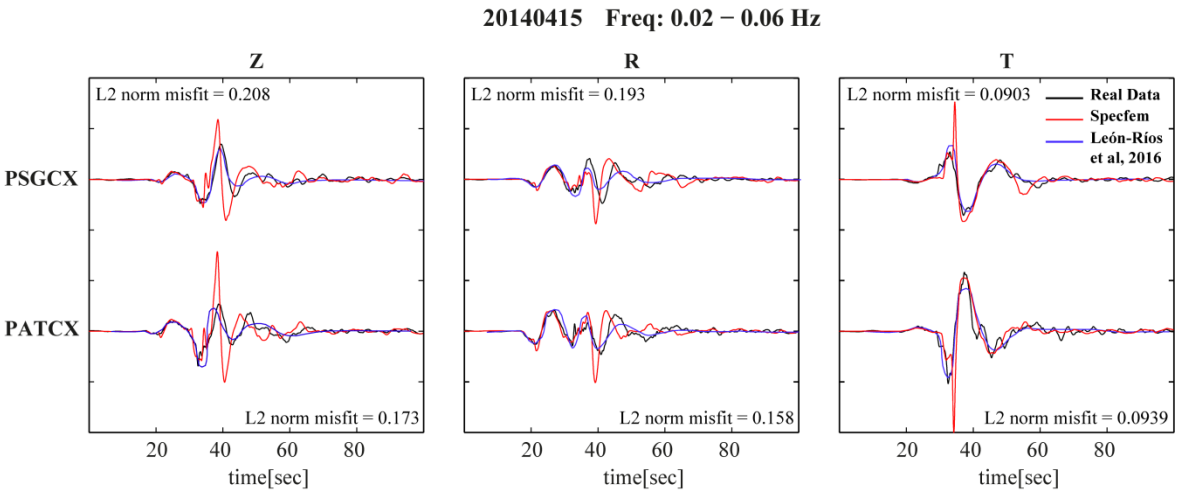

Figure 28: Comparison between real data (black line) for the 15 April 2014 Mw 5.0 earthquake and synthetic seismograms computed using a flat 1-D velocity model (red line) in SPECFEM and the regional moment tensor using the Computer Programs in Seismology package (CPS) computed by León-Ríos et al. (2016). The synthetic seismograms are all differentiated to obtain velocity (in m/s) and are all bandpass filtered between 0.02 and 0.06 Hz. The processed waveforms for the vertical (left), radial (middle) and horizontal (right) components are shown the stations PSGCX and PATCX, whose locations are shown in Figure 27.

The result of the comparison between the real data and the synthetics waveforms presented in **Figure 28**, shows that, in general, for the first 30 seconds, all components of the synthetic waveforms computed in this work coincide in phase and amplitude with the real data and with the synthetic waveforms computed by León-Ríos with the Computer Programs in Seismology (CPS) package. After 30 seconds, despite the peak that occurs in the synthetic waveform at

around 35 seconds, a good fit is obtained in the transverse component, whereas the fit is worse for the vertical and radial components, for both stations.

To quantify the overall fit between the real data and the SPECFEM synthetic waveform obtained a L2 norm misfit is calculated according to the following equation:

$$\text{L2 norm misfit} = \left(\frac{\sum(d_i - s_i)^2}{\sum d_i^2}\right)^{1/2}$$

(Equation 4.4-1)

Where d_i are the real data and s_i is the synthetic data. This normalized misfit parameter indicates the proximity between the real data and the synthetic waveform, point by point, in which misfits close to 0 represents good fits and over 1 represents bad fits.

The **Figure 28** also shows the calculated L2 norm misfit between the SPECFEM synthetic waveforms and the real data, obtaining differences less than 21% for all the components, considered a good agreement.

5. SYNTHETIC MODELS

5.1. TOPOGRAPHIC MODEL SIMULATIONS

To investigate the effects of topography on seismic wave propagation in the study region, simulations for the 13 July 2014 Mw 5.4 earthquake (depth ~34 km; Table 5) using the flat model and the topographic model combined with the 1-D earth structure described in Section 4.3.1 were performed.

Figure 29 and **Figure S1–S4** in the supplementary material compare the synthetic waveforms obtained for both models filtered in four different frequency ranges between 0.1 and 2.0 Hz (0.1–0.2, 0.2–0.5, 0.5–1.0, and 1.0–2.0 Hz). **Figure 29** shows the waveforms filtered between 0.5 and 1.0 Hz for some stations along profile PSGCX (location shown in **Figure 27**), in which three main effects related to topography can be seen. First, as expected, there is a small time shift between the two sets of waveforms due to the difference in altitude between the flat and the topographic model. Second, differences in amplitude can be observed between the three-component waveforms at some stations (e.g., PSGX6 and PSGCX7) located in the coastal cliff (**Figure 29**). Third, the simulations that include topography show waves reflected from the coastal cliff, which appear as a secondary arrival in the vertical and radial components for some stations located at the west of the coastal cliff (PSGCX8, PSGCX9, PSGCX10, etc.) and have the same or slightly larger amplitudes than the main waveforms (see stations PSGCX12, PSGCX14, PSGCX16, and PSGCX18).

To estimate the ground motion amplification generated by the topography at each station, the ratio between the total energy obtained from the velocity seismograms, filtered between 0.1 and 3.5 Hz, was calculated for the topographic and flat models. This calculation involved summing the integrals of the square of the ground velocity of the three components for each seismogram,

and then obtaining the ratio of this sum between the topographic and flat model, as shows **Equation 5.1-1**.

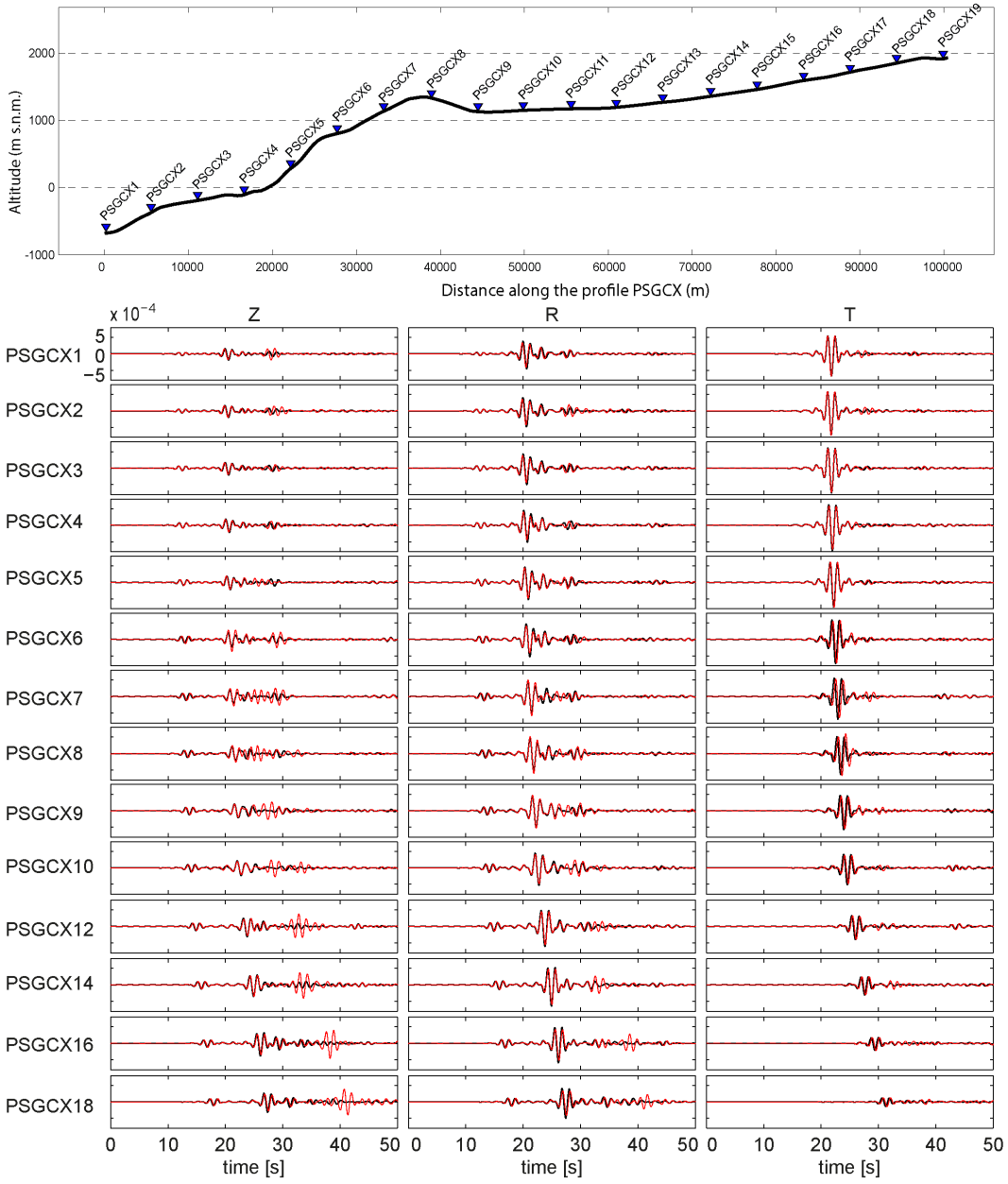

Figure 29: Top: Topography of profile PSGCX. Bottom: Comparison of synthetic seismograms computed using the 1-D flat model (black line) and the 1-D model with topography (red line). The synthetic seismograms are all bandpass filtered between 0.2 and 0.5 Hz. The processed waveforms for the vertical (left), radial (middle) and transverse (right) components are shown for 14 of the 19 stations of the profile PSGCX (see location in Figure 27).

$$AF = \frac{E_{topo}}{E_{flat}} = \frac{(\int v_Z^2 + \int v_R^2 + \int v_T^2)_{topo}}{(\int v_Z^2 + \int v_R^2 + \int v_T^2)_{flat}}$$

(Equation 5.1-1)

The calculated energy ratio or amplification factor (AF) between the topographic model and the flat model for every simulated station, was gridded over a gray-shaded elevation map, as shown in **Figure 30**; in a color grid with values between 0.851 and 1.584. For simplicity, in the remainder of this work, I shall refer to energy ratios > 1 as amplification and energy ratios < 1 as deamplification.

In **Figure 30**, a clear spatial relationship can be observed between amplification domains and the coastal cordillera, which is limited to the west by the coastal cliff and the coastal line (black line). On the other hand, it is possible to observe that topographic deamplification domains are mainly spatially related to the offshore area and valleys located within the coastal cordillera. Overall, the amplification reaches values of up to 2.16 (i.e., an amplification of 116%) and deamplification reaches values as low as 0.55 (i.e., deamplification of 45%).

Figure 31 shows the energy ratio maps for the frequency ranges 0.1–0.2, 0.2–0.5, 0.5–1.0, 1.0–2.0, and 2.5–3.5 Hz, for which maximum energy-ratios of 1.35, 1.53, 3.38, 3.6, and 2.3 were observed, respectively. In these maps, it is possible to observe that amplifications in the land area surrounding the coastal cliff increase with the frequency.

For all the stations and frequency ranges, the maximum amplification factors range between 1.35 and 3.6, with the lowest values being observed for the lowest frequency range (0.1–0.2 Hz) and the largest values of 3.4 and 3.6 being observed in the frequency ranges of 0.5–1.0 and 1.0–2.0 Hz, respectively.

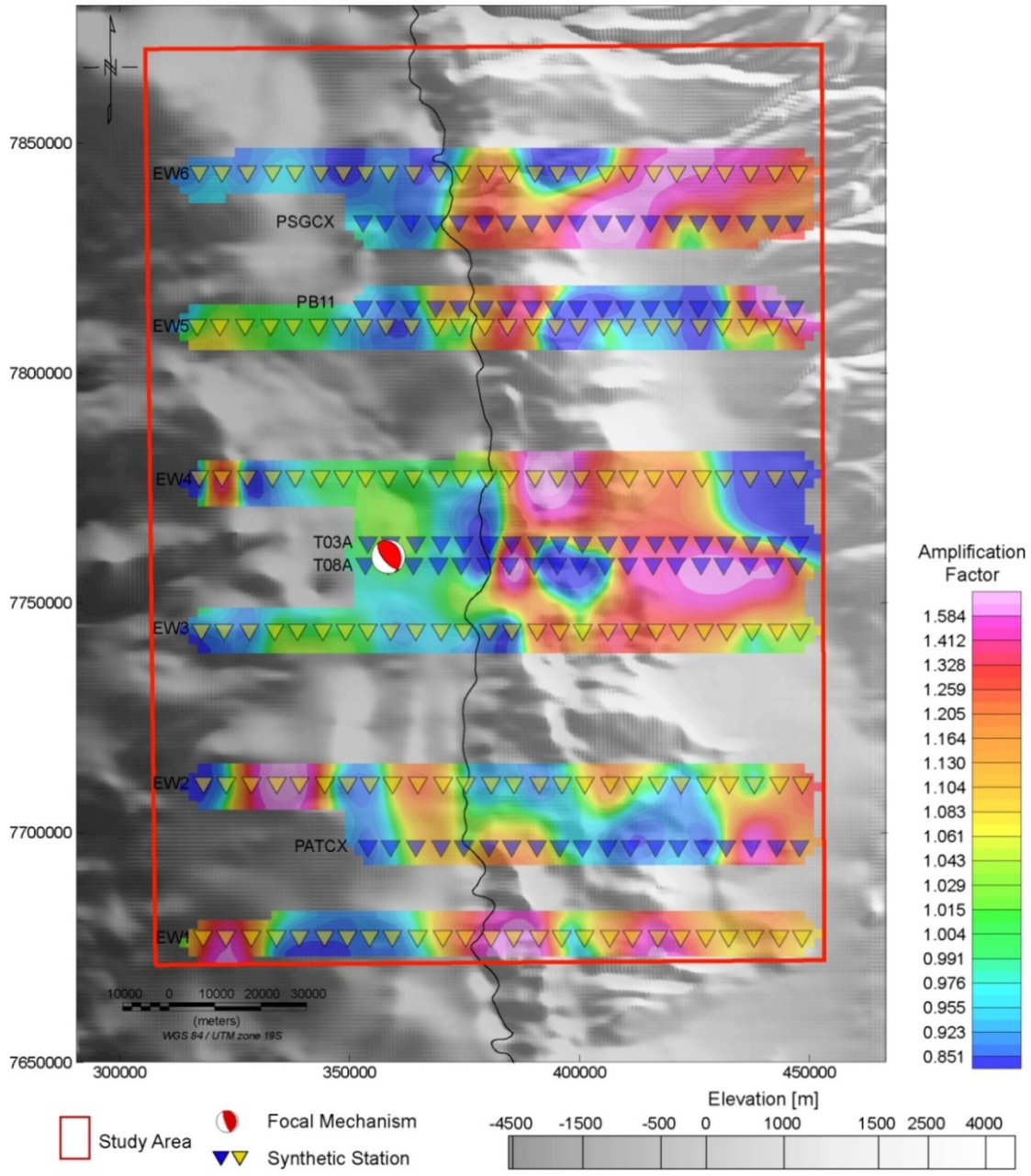

Figure 30: Map showing the energy ratio between the topographic model and the flat model for the velocity waveforms produced by the earthquake represented by the focal mechanism shown in the map. The grid map shows values between 0.851 and 1.584, with the scale being saturated at the extreme high and low values. Ratios less than 1 (green and blue colors) represent relative deamplification due to the topography while values above 1 (green to pink colors) represent relative amplification. The gray-shaded elevation map shows the geomorphological features related to the coastal cliff and the coastal cordillera to the east of the coastal line (black line). The inverted colored triangles show the locations of the synthetic stations used for the calculation of the energy amplification values.

In the same way, deamplification was observed at stations near the coastal line and in the coastal cordillera, spatially related to the coastal plains and valleys into the coastal cordillera. For low frequency ranges, that is, 0.1–0.2 and 0.2–0.5 Hz, an area of deamplification is observed near the coastal cliff. However, this deamplification disappears at higher frequencies, for which a large area of deamplification develops inland near valleys.

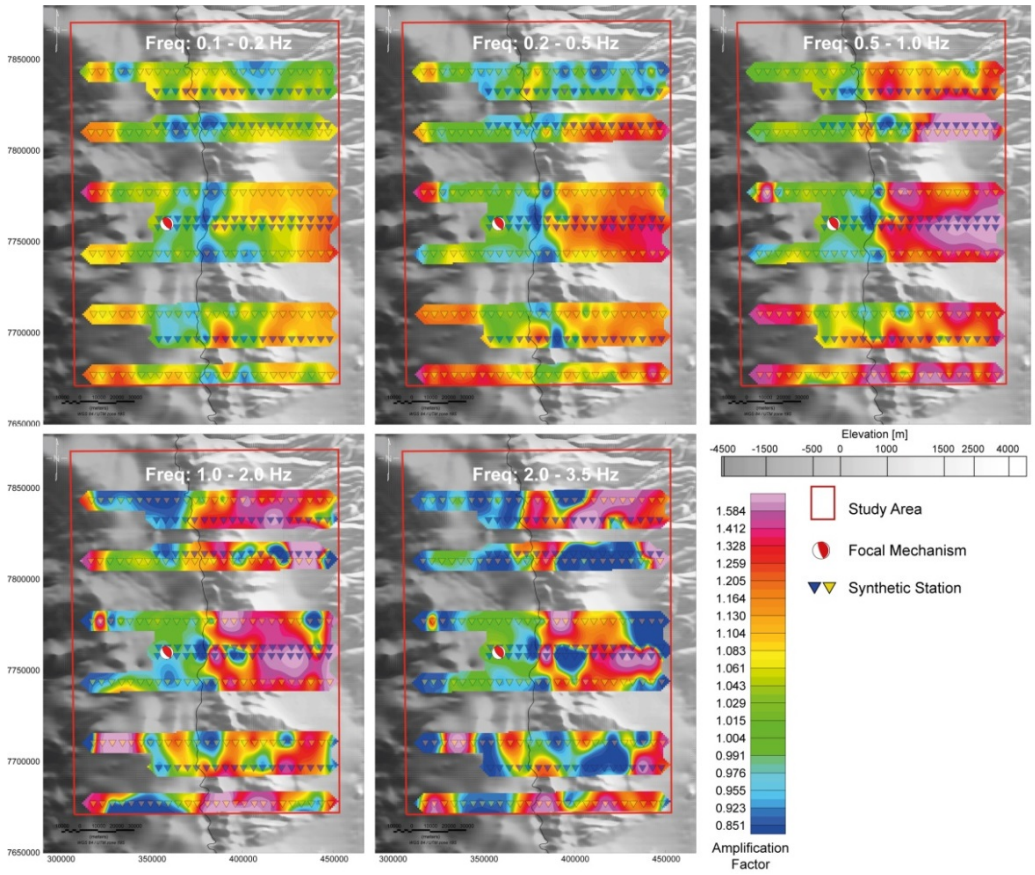

Figure 31: Maps showing the energy ratio between the flat and topographic models for frequency ranges of 0.1–0.2, 0.2–0.5, 0.5–1.0, 1.0–2.0, and 2.0–3.5 Hz. The color grid shows the energy amplification in the velocity waveforms produced by the earthquake represented by the focal mechanism located in the map, simulated for the flat and topographic model. The color scale shows values between 0.85 and 1.58, in a saturated scale, where values below 1 represent deamplification between flat and topographic model and values above 1 represent amplification between the flat and topographic model. The gray-shaded elevation map shows the geomorphological features related to the coastal cliff and the coastal cordillera to the east of the coastal line (black line). The colored triangles show the locations of the synthetic stations used for the calculation of the energy amplification values.

5.2. BASIN MODEL SIMULATION

In order to investigate the effect of the study region's basins on the seismic waveforms, this section presents the computation of synthetic seismograms for the 13 July 2014 Mw 5.4 earthquake using the 1-D velocity model with topography only and the 1-D velocity model with topography and basins, in which the sedimentary basins are simulated as described in **Section 4.3.1**.

A comparison of the synthetic waveforms obtained with the topography-only model and the model with topography and basins is shown in **Figure 32** for 11 seismograms along profile T08A, which crosses the Alto Hospicio basin from west to east, filtered between 0.5 and 1.0 Hz. In the same way, **Figure 33** shows a comparison between the synthetic waveforms for profile PB11, which crosses the Pampa del Tamarugal basin, filtered between 0.5 and 1.0 Hz.

From the comparison of the two types of synthetic waveforms in **Figure 32**, it can be seen that the differences between them are not significant until the seismic wave field reaches stations T08A7 and T08A8, which are located in the area surrounding the Alto Hospicio basin. These two stations show amplification of the seismic waves in the vertical and transverse components, while slight deamplification is observed for the radial component. On the other hand, the seismic stations further to the east (from T08A9 to T08A19) show small differences in amplitude between the transverse-component waveforms obtained for the two models, which is probably due to the reflection of waves in the Alto Hospicio basin.

Similarly, a comparison of the synthetic waveforms observed for the stations along profile PB11 in **Figure 33** shows evident amplification of the seismic waves at stations located in the modeled Pampa del Tamarugal basin (from PB11-12 to PB11-18), most notably for the vertical and radial components.

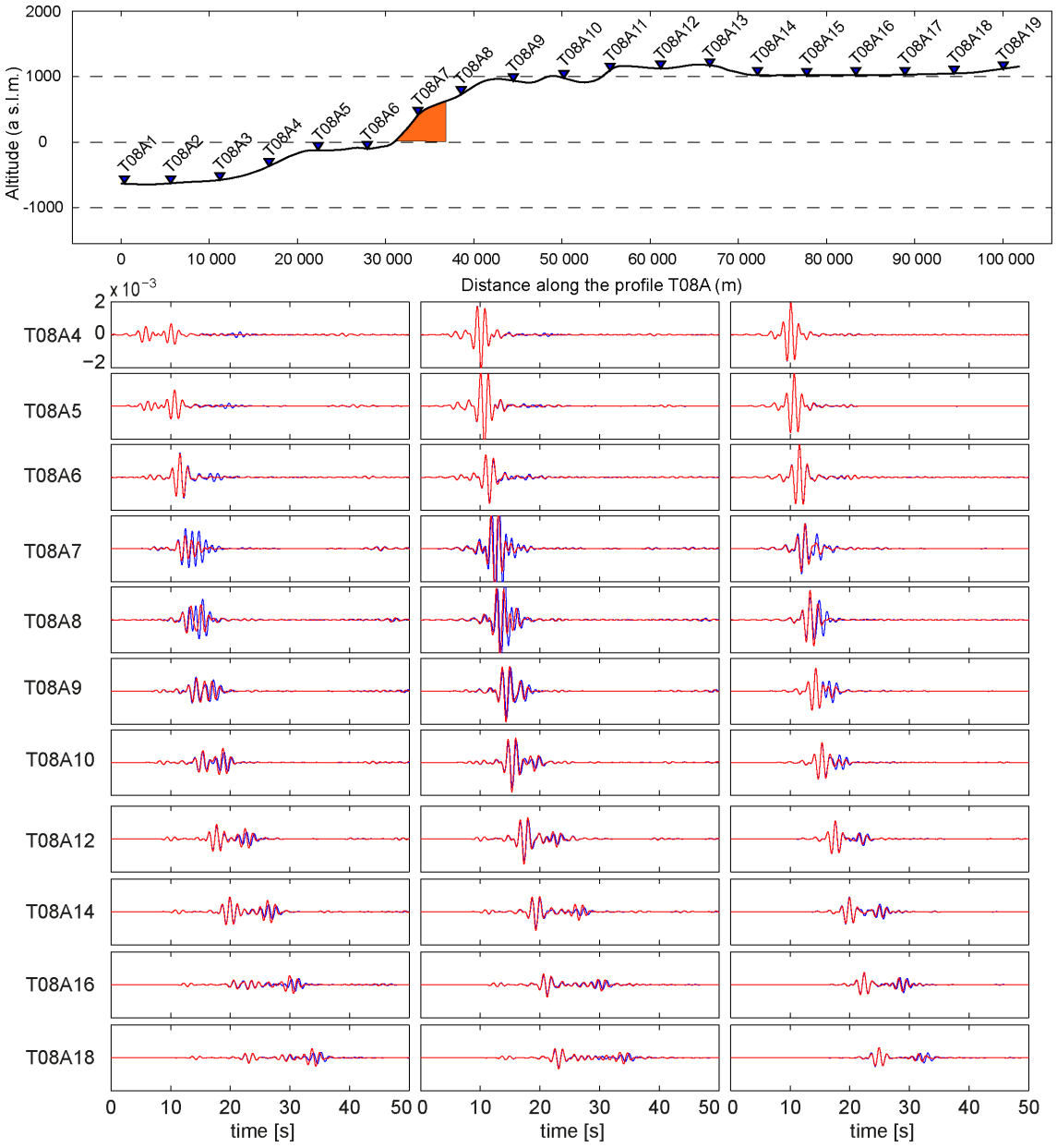

Figure 32: Top: Topography of profile T08A and the modeled Alto Hospicio basin (represented by the orange polygon). Bottom: Comparison of synthetic seismograms computed using the 1-D velocity model with topography only (red line) and the 1-D velocity model with topography and basins (blue line). The synthetic seismograms are all bandpass filtered between 0.5 and 1.0 Hz. The processed waveforms for the vertical (left), radial (middle), and transverse (right) components are shown for 11 of the 19 stations of profile T08A (see location in Figure 27).

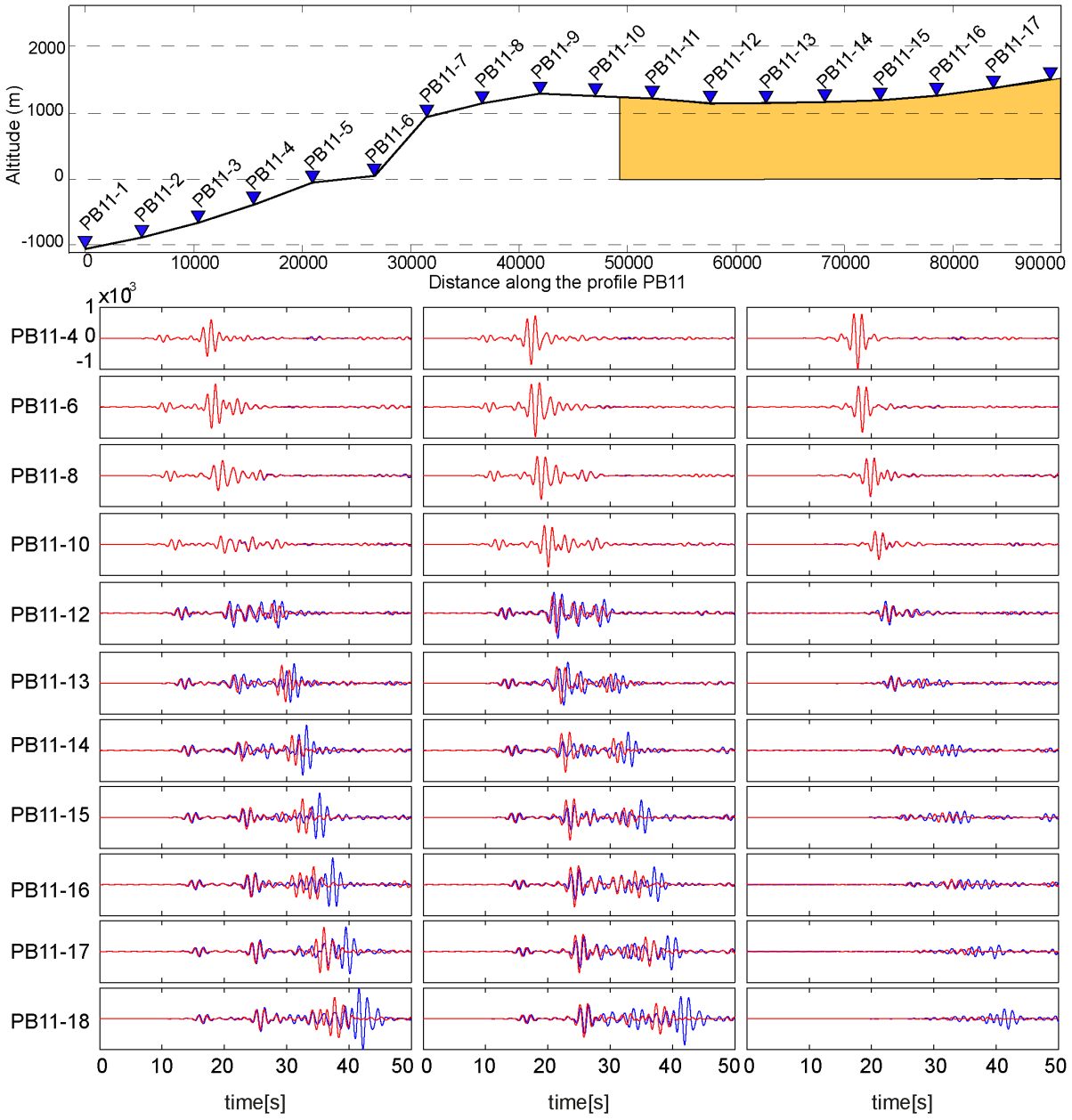

Figure 33: Top: Topography of profile PB11 and the modeled Pampa del Tamarugal basin (represented by the yellow polygon). Bottom: Comparison of synthetic seismograms computed using the 1-D velocity model with topography only (red line) and the 1-D velocity model with topography and basins (blue line). The synthetic seismograms are all bandpass filtered between 0.5 and 1.0 Hz. The processed waveforms for the vertical (left), radial (middle), and transverse (right) components are shown for 11 of the 19 stations of profile PB11 (see location in Figure 27).

The frequency dependence of the amplification effects due to the Alto Hospicio and Pampa del Tamarugal basins is clearly visible in **Figures S5–S8** (for profile T08A) and **Figures S9–S12** (for profile PB11) in the supplementary material, which present the complete set of synthetic waveforms, filtered between 0.1–0.2, 0.2–0.5, 0.5–1.0, and 1.0–2.0 Hz.

As in the previous section, the energy ratio between the topography-only model and the model with topography and basins was calculated (**Equation 5.2-1**) and gridded for the synthetic waveforms filtered between 0.1 and 3.5 Hz, as shown in **Figure 32**. This grid shows values of the energy ratio between 0.851 and 1.584 in a saturated scale.

$$AF = \frac{E_{basin}}{E_{topo}} = \frac{(\int v_Z^2 + \int v_R^2 + \int v_T^2)_{basin}}{(\int v_Z^2 + \int v_R^2 + \int v_T^2)_{topo}}$$

(Equation 5.2-1)

This energy ratio map (**Figure 34**) shows clear amplification at the stations located within basins (blue rectangles), with the amplification values reaching up to 2.9 (representing a 190% increase in amplitude), as well as amplification values of up to 1.25 (25% increase in amplitude) in stations in the far southeast region of the study area. Additionally, **Figure 34** also shows a clear deamplification of up to 0.75 (25% decrease in amplitude) in areas surrounding the basins.

The energy ratio maps for frequency ranges of 0.1–0.2, 0.5–1.0, 1.0–2.0, and 2.0–3.5 Hz are presented in **Figure 35**. As shown in the figure, the amplification generally increases with frequency, reaching a maximum value of 3.9 in the range of 1.0–2.0 Hz for stations located in the Pampa del Tamarugal basin. Meanwhile, for stations located in the Alto Hospicio basin, the amplification clearly increases with frequency, reaching a maximum of 3.1 in the frequency range 2.0–3.5 Hz.

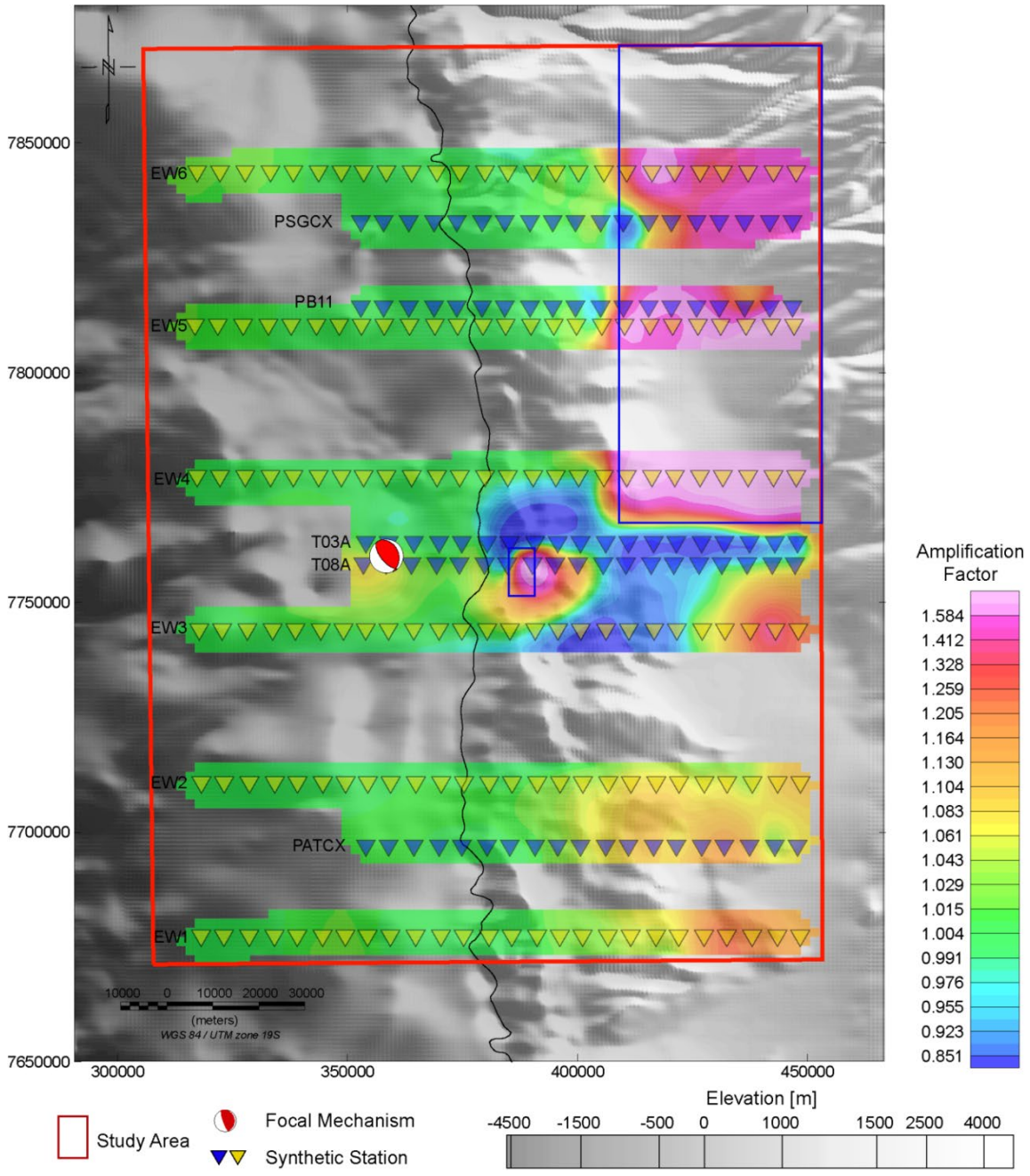

Figure 34: Map showing the energy ratio in the velocity waveforms between synthetic seismograms obtained using the model with topography only and the model with topography and basins. Values above 1 represent relative amplification in the model with topography and basins, while values below 1 represent relative deamplification in this model. The beach ball represents the earthquake source. The gray-shaded elevation map shows the geomorphological features related to the coastal cliff and the coastal cordillera to the east of the coastal line (black line). The colored triangles show the locations of the synthetic stations used for the calculation of the energy amplification values.

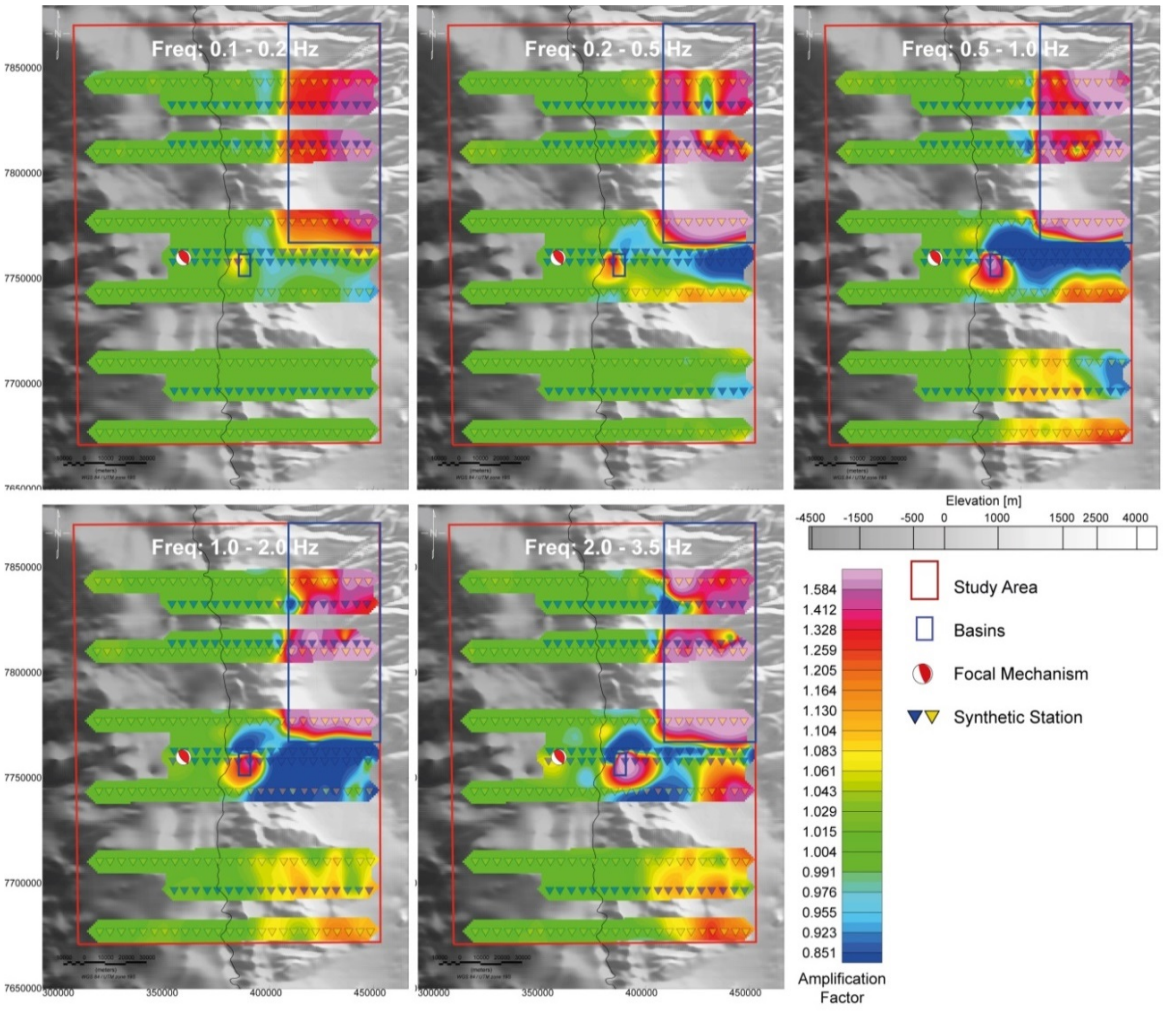

Figure 35: Map showing the energy ratio between the model with topography only and the model with basins and topography, for frequency ranges of 0.1–0.2, 0.2–0.5, 0.5–1.0, 1.0–2.0, and 2.0–3.5 Hz. The beach ball represents the earthquake source. The colored scale shows values between 0.85 and 1.58, where values <1 represent deamplification between the topography-only model and the topography and basin model and values >1 represent amplification. The gray-shaded elevation map shows the geomorphological features related to the coastal cliff and the coastal cordillera to the east of the coastal line (black line). The colored triangles show the locations of the synthetic stations used for the calculation of the energy-ratio values.

5.3. 2-D VELOCITY MODEL SIMULATION

A 2-D velocity model with topography was developed in order to investigate the effects of the crustal velocity structure on the waveforms. In this section, the synthetic seismograms for the 13 July 2014 Mw 5.4 earthquake obtained using the 1-D velocity model with topography and the 2-D velocity model with topography are compared, in which the 2-D velocity model was implemented as described in **Section 4.3.1**.

Figure 36 shows a comparison between the synthetic waveforms obtained using the 1-D velocity model with topography and the 2-D velocity model with topography for 10 seismograms along profile PATCX, filtered between 0.5 and 1.0 Hz. From the comparison, it is possible to see differences in amplitude, phase, and arrival time, particularly in the radial (R) and transverse (T) components. These differences become larger with increasing source–station distance and are present at all frequencies, as shown in **Figures S13** to **S16** in the supplementary material**.**

In general, the 1-D velocity model shows larger amplitudes for the vertical and radial components, while the 2-D velocity model shows larger amplitudes for the transverse component, most notably at frequencies between 0.5 and 2.0 Hz. Additionally, differences in arrival time are produced in all components for all stations and all frequencies, significantly increasing with the source–station distance and the frequency. These differences are related to the differences in the velocity models, which become more significant for longer path lengths.

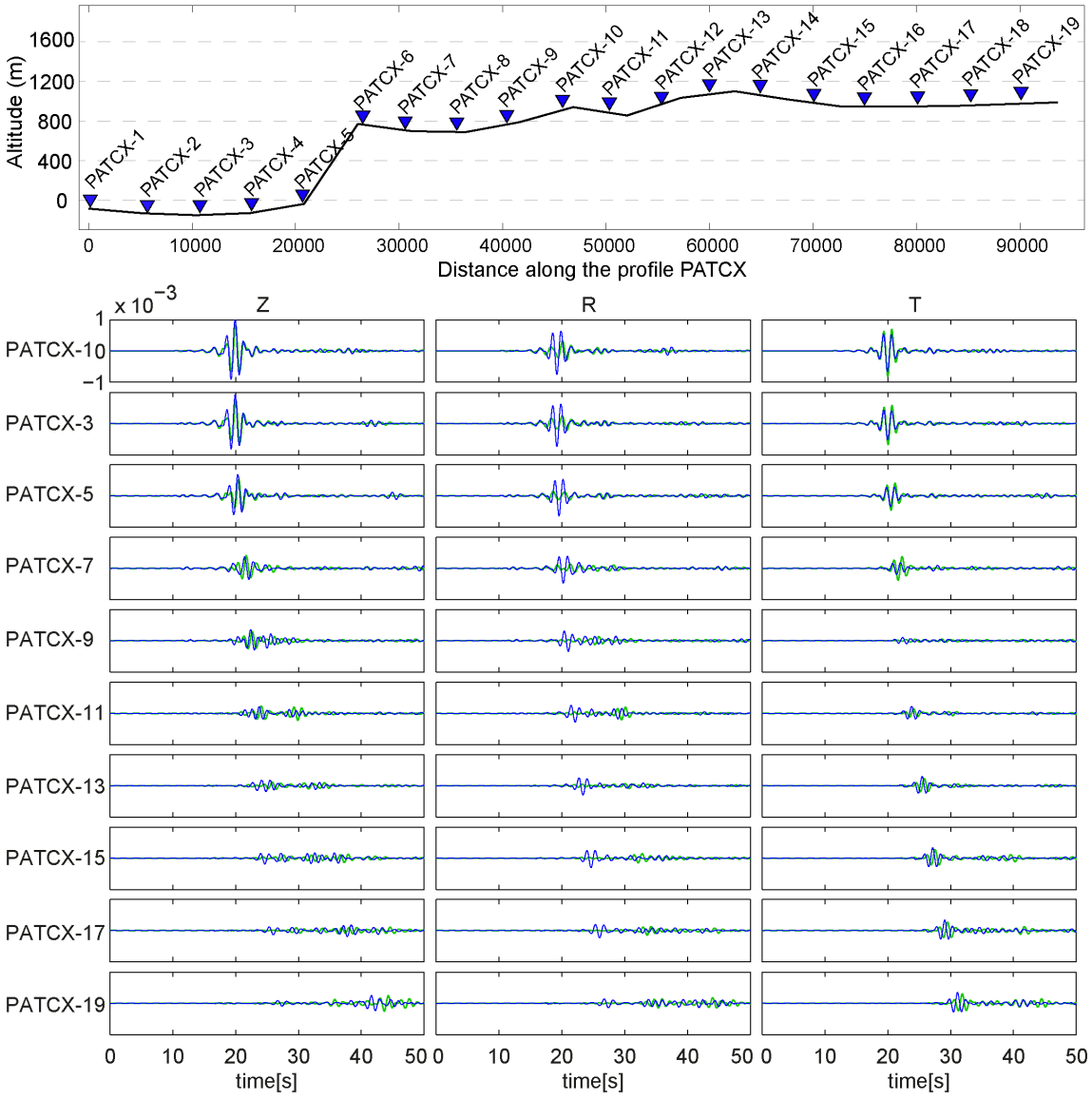

Figure 36: Top: Topography of profile PATCX. Bottom: Comparison of synthetic seismograms computed using the 1-D velocity model with topography (red line) and the 1-D velocity model with topography and basins (blue line). The synthetic seismograms are all bandpass filtered between 0.5 and 1.0 Hz. The processed waveforms for the vertical (left), radial (middle) and transverse (right) components are shown for 10 of the 19 stations of profile PATCX (location shown in Figure 27).

6. COMPARISON WITH REAL DATA

In this section, a comparison is shown between the different synthetic waveforms obtained in this study with real data for the 02 April 2014 Mw 4.5 and 13 July 2014 Mw 5.4 earthquakes. As explained previously, the selection of the earthquakes was based on the similarity between their focal mechanisms and that of the main 01 April 2014 Mw 8.1 Iquique earthquake, but their smaller magnitudes avoid the extended source complexity effects that are present in the real data due to the large size of the 01 April earthquake, thus allowing the site effects to be visualized more precisely. As the RSN network provides acceleration data, the IPOC data and all of the synthetic seismograms were double-differentiated to obtain acceleration values for all the stations considered.

The real data and the synthetic seismograms were processed in the same way by removing the trend and the mean and rotating the horizontal components into radial and transverse components. Finally, all the waveforms were bandpass filtered with a four-pole two-pass Butterworth filter for different frequency ranges between 0.1 and 3.5 Hz.

6.1. SIMULATION OF THE 02 APRIL 2014 MW 4.5 EARTHQUAKE

The Mw 4.5 earthquake of 02 April 2014 was located at a depth of ~50 km, with the hypocenter located close to the coastal line. The simulations for this earthquake included three different models: the flat 1-D velocity model; the topography-only 1-D velocity model; and the 1-D velocity model with topography and basins (as explained in Section 4.3.1). A comparison of the synthetic waveforms obtained from these three different simulations and the real data is shown in **Figure 37**. **Figure 37** also shows the L2 norm misfit value calculated between the real data and the flat model (black letters), real data and the topography model (blue letters) and real data and the topography and basin model (red letters) respectively.

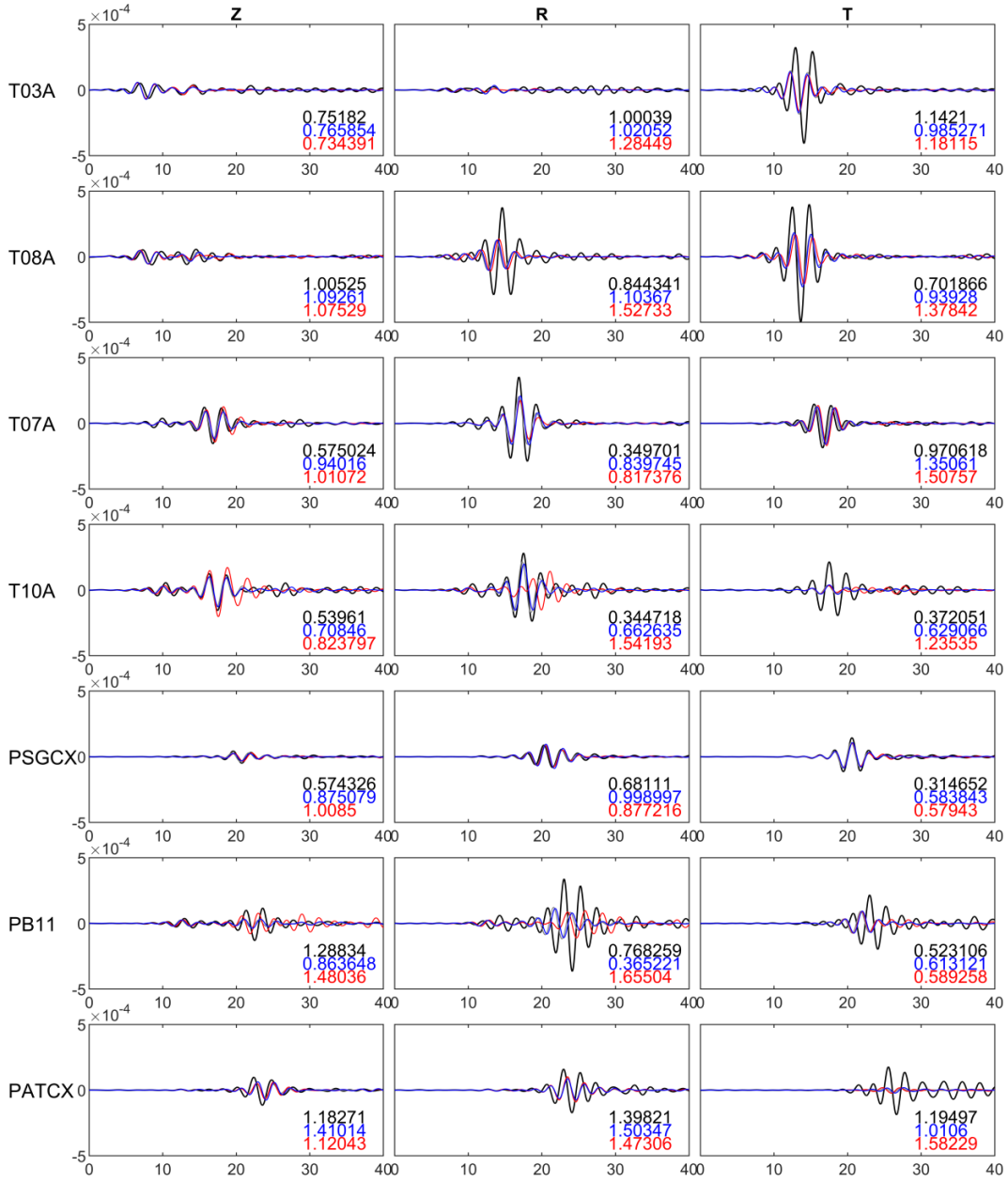

Figure 37: Comparison between real data (black line) for the 02 April 2014 Mw 4.5 earthquake and synthetic seismograms computed using the flat 1-D velocity model (gray lines), the 1-D velocity model with topography (blue line), and the 1-D velocity model with topography and basins (red lines). Synthetic seismograms are double differentiated to obtain acceleration in m/s2 and are all bandpass filtered between 0.2 and 0.5 Hz. The processed waveforms for the vertical (left), radial (middle) and horizontal (right) components are shown for seven stations, whose locations are shown in Figure 27. The L2 norm misfit value between the real data and the different model for each station in the three components is also presented, using the same color code than the lines.

The results for the different computed models show that there are only slight differences between the waveforms obtained for the flat and topography models, while more significant differences are observed for the model with topography and basins for the stations located within or around the modeled basins. Overall, a good fit is obtained between the real and synthetic waveforms for stations T03A (vertical and radial components), T08A (vertical component), T07A, and PSGCX, with small time shifts and some differences in amplitude, mostly in the radial and transverse components.

For stations PB11, T10A, and PATCX, larger differences are observed between the real data and the synthetic seismograms. Stations PB11 and T10A are located in the Pampa del Tamarugal basin (**Figure 27**), and, despite the fact that the wave amplitudes obtained using the model with topography and basins show differences to those obtained using the topographic-only and flat models, the real data are much more complex than the synthetic waveforms computed for the basin model. The disagreement between the real data and the synthetic waveforms obtained using the basin model is probably due to the simplified geometry and elastic properties of the basin used in the simulations. On the other hand, station PATCX shows substantial differences in phase and amplitude between the real data and the synthetics.

By considering different frequency ranges (see **Figures S17–S20** in the supplementary material), it can be seen that the differences between the real and synthetic waveforms increase as frequency increases, which implies that shallower structures are probably responsible for the complexity in the waveforms, since these structures are not included in the simple models.

6.2. SIMULATION OF THE 13 JULY 2014 MW 5.4 EARTHQUAKE

The 13 July 2014 Mw 5.4 earthquake was located at a depth of ~35 km and 20 km offshore from the coastal line. As in the previous section, three different models were used to simulate the seismic wave propagation from this earthquake, however this time using the 1-D velocity model with topography-only, the 1-D velocity model with topography and basins, and the 2-D velocity model with topography. A comparison of the synthetic waveforms obtained from these three models and the real data is shown in **Figure 38** in which, similarly to the previous simulation, the L2 norm misfit value calculated between the real data and the different models for each station in the three components is also presented.

As shown in **Figure 38**, there is a good fit between the simulated and real data for stations T01A, T08A, PATCX, and T07A, while stations PSGCX and PB11 present a poor fit in the late part of the waveforms, notably after arrival times of approximately 20 seconds. Additionally, minor time shifts and amplitude differences are observed for the 2-D velocity model with topography compared with the other two models after arrival times of approximately 20 seconds.

On the other hand, slight time shifts and differences in amplitude are observed between the waveforms simulated using the 1-D velocity model with topography model and those simulated using the 1-D velocity model with topography and basins for (1) stations T01A and T08A, which can be attributed to the effect of the Alto Hospicio basin, and (2) station T07A, which can be attributed to the effect of the Pampa del Tamarugal basin. For station PB11, there are larger differences between the real waveforms and the synthetic waveforms calculated using the topographic and basin models, however, the latter model performs less well in reproducing the complexity of the real data.

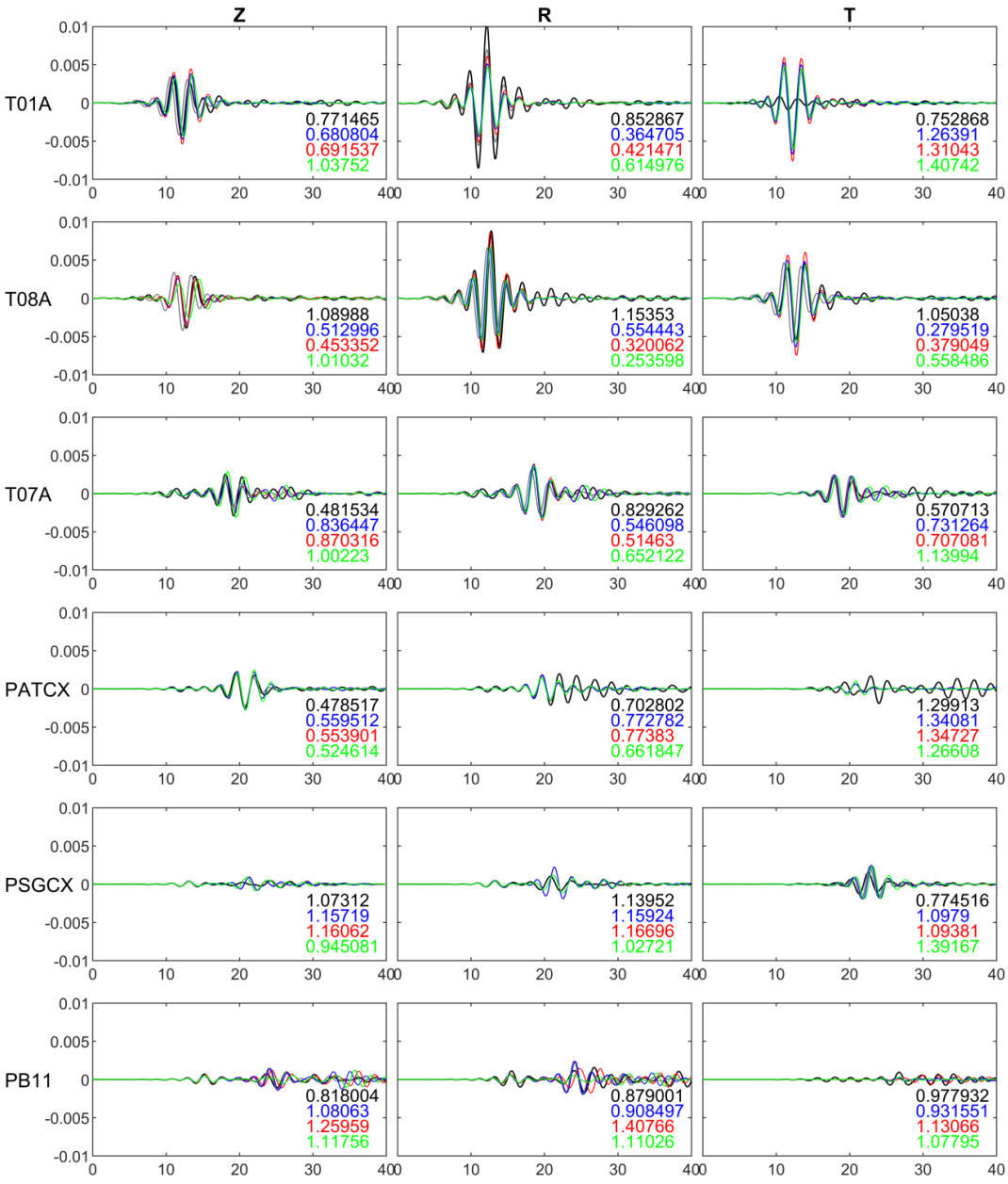

Figure 38: Comparison of real data (black line) for the 07 July 2014 Mw 5.4 earthquake and synthetic seismograms computed using the 1-D velocity model with topography (blue line), 1-D velocity model with topography and basins (red lines), and 2-D velocity model with topography (green lines). Synthetic seismograms are double differentiated to obtain acceleration in m/s^2 and are all bandpass filtered between 0.2 and 0.5 Hz. The processed waveforms for the vertical (left), radial (middle) and horizontal (right) components are shown for six stations, whose locations are shown in Figure 27. The L2 norm misfit value between the real data and the different model for each station in the three components is also presented, using the same color code than used in the lines.

Similar to the 02 April 2014 Mw 4.5 event, the differences between the real and simulated waveforms increase with increasing frequency (see **Figures S21** to **S24** in the supplementary material).

Figure 39 shows the L2 misfit values for the 02 of April of 2014 and 13 of July of 2014 earthquakes between the real data and the simulated waveform for all the models and all the frequency ranges according the **Equation 4.4-1** presented in the section **4.4**. In **Figure 39** the misfit values for each station are presented using different symbols for each component, using circles for vertical component (Z), square for radial component (R) and diamonds for transverse (T) component, and different colors for each model, using black for 1-D velocity flat model, blue for 1-D velocity with topography model, red for the topography with basins model and green for 2-D velocity with topography model. The stations are displayed in the graphs with increasing epicentral distance.

These graphs show that the misfit values are widely spread between 0.1 and 2, probably due to the fact that the calculation of the misfit does not distinguish differences between the real data and the simulated waveforms due to the amplitude or the phase, therefore the misfit augment if there are important differences in amplitudes or if the waveforms have differences in phase.

However, from the analyses of the misfit values, it is possible to say that the fit between the real and simulated waveforms deteriorates with increasing epicentral distance and with increasing frequency ranges.

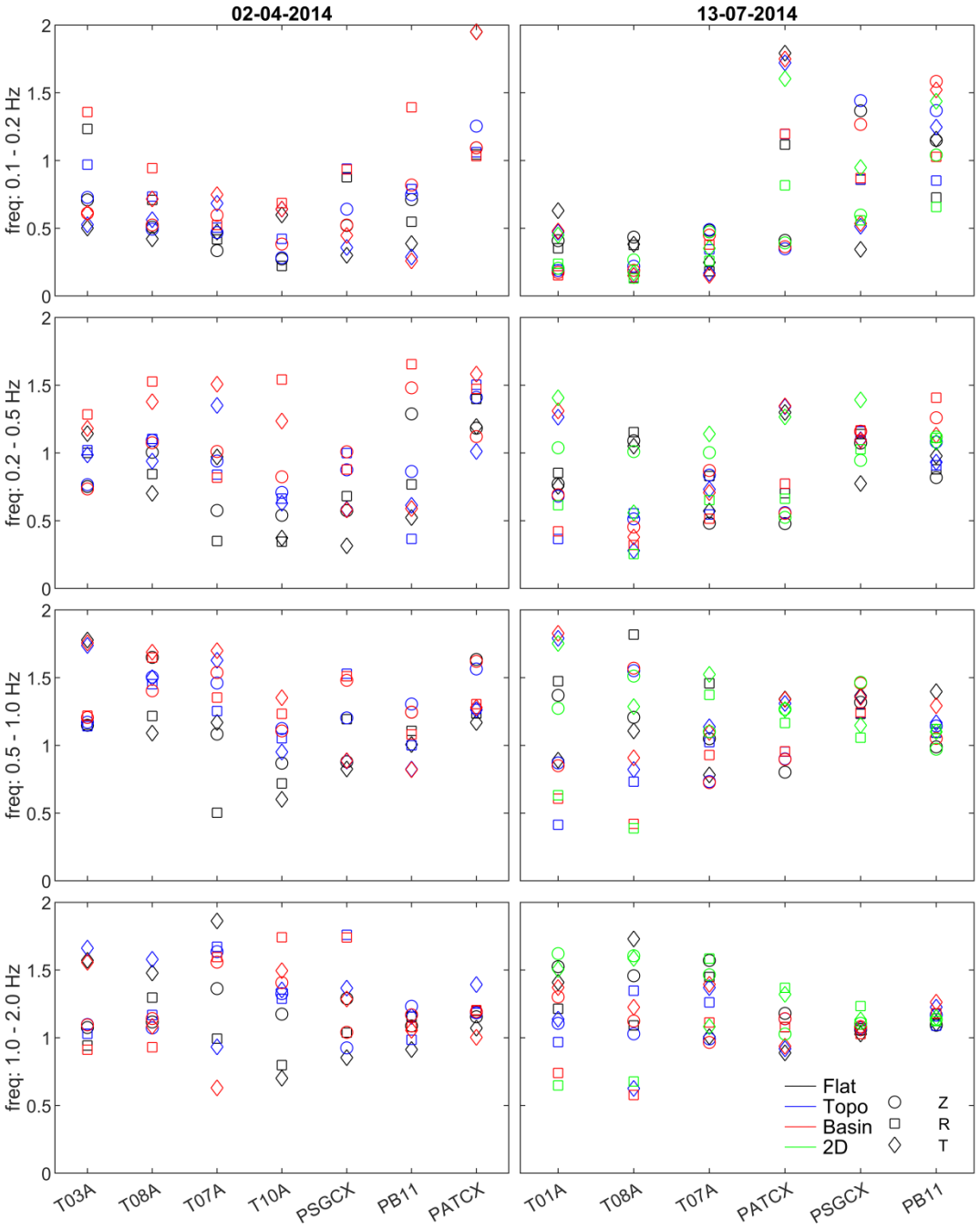

Figure 39: Misfit between real data and synthetic seismograms for different frequencies ranges and different simulated stations for the 02-04-2014 and 13-07-2014 earthquakes. The circles, squares and diamonds indicates the misfit value for each vertical (Z), radial (R) and transverse (T) components, whereas the different colors represents the comparison between the real data and the flat model (black), the real data and the topography model (blue), the real data and the basin with topography model (red) and the real data and the 2D velocity and topography model (green), respectively.

7. DISCUSSION

7.1. TOPOGRAPHY EFFECTS

This study shows that topography modifies the seismic ground motion response by changing the amplitude and duration of waveforms due to the reflections generated by topographic features. When seismic waves come into contact with topographic structures, the structures interact with the incident waves and modify them, producing reflected waves that increase the amplitude of the incident waves at the top of the topographic feature and propagate through the surrounding areas. As the distance between the topographic feature that produced the reflected wave and the observation point increases, the time separation between the incident and the reflected wave also increases, which in turn augments the duration of ground motion at the observation point. The results show that the amplitude of the reflected waves can be larger than that of the incident waves in some locations (see stations PSGCX-12, PSGCX-13, PSGCX-14, and PSGCX-15 in **Figure 29** and **Figures S1–S4** in the supplementary material), which has important implications for the seismic hazard in locations near to topographic features (Sánchez-Sesma & Campillo, 1993).

Previous studies reported topographic seismic amplification factors between 2 and 50% and found that amplification generally occurs close to the tops of slopes, whereas deamplification occurs at the bottoms of slopes (Boore, 1972; Bouchon et al., 1996; Bouchon, 1973; Buech et al., 2010; Paolucci, 2002). The results of this study indicate that, for the frequency range between 0.1 and 3.5 Hz, the amplification factor between the flat and topographic models reaches up to 2.2 (that is, an amplification of 120%) and that areas of amplification (i.e., energy ratio > 1) are strongly spatially related with the tops of topographic features such as the Coastal Cordillera (see **Figure 30**). On the other hand, areas of deamplification are observed in valleys

formed between hills, where amplification factors can reach values of 0.6 (i.e., 40% deamplification), which agrees with the aforementioned studies.

The analysis of different frequency ranges shows that, for stations located east of the coastal line, the degree of amplification increases as the frequency increases, and the amplification is spatially related to the Coastal Cliff and the Coastal Cordillera. The results also suggest that areas of amplification and deamplification are related to the size (height and width) and shape of the topographic features, where large features such as the Coastal Cliff (500–1000 m in height) or the Coastal Cordillera (50,000 m width) produce major effects in the 0.1–0.5 Hz frequency range, while smaller features such as hills and valleys in the Coastal Cordillera (~50–100 m in height and ~1000–3500 m in width) produce effects in the 1.0–3.5 Hz frequency range (see **Figure 31**). The relationship between seismic amplification and frequency for topographic features has been investigated in several previous studies. For example, in the Little Red Hill experimental studied presented by Buech et al. (2010), the frequency-domain analysis shows a maximum amplification at about 5 Hz, which is close to the first resonant frequency harmonic equal to the half-width or the height of the edifice. In the same way, the effects observed for a three-dimensional ellipsoid hill studied by a semi-analytical semi-numerical method show that amplification occurs at and near the top of the hill over a broad range of frequencies, and the maximum amplification value depends on the geometry of the features (Bouchon et al., 1996). In general, it is possible to say that the frequency of maximum amplification corresponds to a wavelength that is comparable to the mountain's width (Geli et al., 1988 and references therein), which is consistent with the results obtained in this work.

The results obtained in this work also agree with the findings of Lee et al (2009), who investigated seismic amplification due to topography using the SEM. They used a LiDAR digital terrain model (DTM) of the Yangminshan region in Taiwan to construct a high-quality

topographic model using a 4x4x10 km^3 mesh with a surface resolution of 2 m, obtaining peak ground acceleration (PGA) amplification of around 50% due to variations in topography in mountainous areas. The result obtained using the high-resolution topographic model for the Yangminshan region agrees with the amplifications found in this work, despite the use of a lower-resolution mesh (~200–300 m) and a larger domain (145 x 200 x 60 km^3). The compromise of a low-resolution mesh—which probably does not completely reproduce realistically the effects of the topography—was made to allow a larger domain to be studied, which allows the modeling of real earthquakes produced in the Iquique region and the comparison of the simulated waveforms with real observations in order to validate the results.

7.2. BASIN EFFECTS

As expected, the results obtained in this work showed that basins have a significant impact on the ground motion response, increasing the amplitude and duration of the incident seismic waves and producing reflections at their edges which propagate both within the basin and in the surrounding areas (Celebi, 1987; Frankel et al., 2002; Paolucci & Morstabilini, 2006; Semblat et al., 2005).

The results also show that basin amplifications are related to the size of the basin and are strongly frequency dependent. For example, in the frequency band between 0.1 and 3.5 Hz (see **Figure 34**), amplification occurs in the interior of the basins, reaching amplification ratios of up to 2.9 in the Pampa del Tamarugal basin and 2.2 in the Alto Hospicio basin—i.e., in the large and small basins, respectively—showing that larger amplification values are produced in the larger basin. The analysis of the amplification in different frequency ranges (see **Figure 35**) indicates that the amplitude and complexity of the amplification is intimately related to the frequency, as is clearly visible in the increasing amplification values with increasing frequency

for the Alto Hospicio basin, which suggests that the smaller basin interacts more with higher frequency waves (Semblat et al., 2002).

The peak amplification of 3.9 in the frequency range 1.0–2.0 Hz for the Pampa del Tamarugal basin and of 3.1 for the range 2.0–3.5 Hz for the Alto Hospicio basin obtained in this work agree with the results of Paolucci & Morstabilini (2006), who found that the peak amplification occurs at frequencies slightly larger than the fundamental resonance frequency of the sedimentary layer given by $f_0 = V_s/4H$, where V_s is the S-wave velocity of the basin and H is the height of the non-consolidated sedimentary soil, which is less than or equal to the height of the basin. This basin-related frequency-dependency of amplification was also shown in several other empirical and analytical studies (Borcherdt, 1970; Borcherdt & Glassmoyer, 1992; Day et al., 2008; Field, 1996; Semblat et al., 2002).

The results obtained in this work also show deamplification occurring at the edges of the basins, at the interface between rock and basin. This result is probably due a complex process of wave's interaction, including constructive and destructive waves summing, among other processes. One basic, rather simplistic, wave propagation calculation can provide some insights on the amplification at the basin/rock boundary. Considering a horizontal SH-wave incidence at the basin/rock interface, with sediments acoustic impedance 4/5 the acoustic impedance of the rock; the rock to sediment transmitted energy is 8/9, while the reflected energy is 1/9 for a unitary incidence ray (energy is conserved at the interface but not the amplitude). This reflected wave may produces deamplification in the basin's adjacent rock domain. Reality is much more complex, but this simple exercise provides a qualitative physical argument to explain the phenomena. The deamplification observed in the southern edge of the Pampa del Tamarugal basin also shows a clear frequency dependence, reaching a minimum value of 0.75 (i.e. 25% of deamplification) and a maximum spatial extent in the frequency range of 0.1–2.0 Hz, which is

also the frequency range associated with maximum amplification within the Pampa del Tamarugal basin. The deamplification observed in the basin's surroundings is an interesting result for seismic hazard analysis.

Notwithstanding the simplicity of the basin model used in this study, the amplifications observed in the simulations agree with the results obtained using more complex 3-D velocity basin models in previous studies. For example, using finite difference simulations to determine the three-dimensional seismic response in the Los Angeles basin, Olsen (2000) obtained average amplification factors of up to 4.

7.3. 2-D VELOCTY MODEL

The comparison between the 1-D and 2-D velocity models shows differences in amplitude and arrival time in the synthetic waveforms for all stations and all frequencies. These differences increase with increasing distance from the source. Therefore, the more distance the seismic waves have to travel, the larger the differences between the velocity models. Generally, the 2-D velocity model has lower velocity values, and therefore, the synthetic waveforms present delays compared with the waveforms generated in the 1-D velocity model. These delays are more significant for the secondary waves in the vertical component and in the radial and transverse components, evidencing larger differences in the S-wave velocity model.

The main purpose of the implementation of a 2-D velocity model was to improve the fit between the modeled waveforms and the real data, as, for earthquakes with shallow hypocenters (e.g., 13 July 2014), the fit deteriorates with increasing distance from the source. The results of the 2-D velocity model indicate that the fit did not improve. There are multiple potential explanations for this result: First, a 1-D velocity model was used to determine the location of the earthquakes by León-Ríos (2015), and therefore, it is likely that the same 1-D velocity model would better reproduce the waveforms; second, in the implementation of the 2-D velocity model,

approximations were used to obtain the S-wave velocity and the density, which may be not representative of the real crustal structure; third, the 2-D velocity model was extended to the west simply by using the last velocity values, which is a significant simplification of the crustal structure; and lastly, the 2-D velocity model was copied to the north and the south in order to build a 3-D model, which may not be representative of the longitudinal variations of the crustal structure. All these approximations generated a simplistic 2-D velocity model.

7.4. COMPARISONS WITH REAL DATA

The analyses for the 02 April 2014 Mw 4.5 and the 13 July 2014 Mw 5.4 earthquakes demonstrate a good first-order fit between the real waveforms and the modeled waveforms using a simplified 1-D velocity model with topography, notably for wave periods between 2 and 10 seconds. A particularly good match between the modeled waveforms and the real data was obtained for stations T01A, T03A, T07A, and T08A for both earthquakes (**Figure 37** and **Figure 38** and **Figure S17**–**S24** in the supplementary material), with small time shifts and amplitude differences, especially for the radial and transverse components. The 1-D velocity model with topography and basins shows an acceptable match for the station T08A, which is located in the modeled Alto Hospicio basin, for the 13 July 2014 earthquake, and differences in amplitude for the 02 April 2014. However, poor fits between the real data and the simulated waveforms were obtained for those stations near or within the Pampa del Tamarugal basin. This disagreement between the real and synthetic waveforms may be related to the simplified geometry and elastic properties of the Pampa del Tamarugal basin used in the simulations, which do not consider complex effects related to different soil layers and the heterogeneities at the base of the basin.

In simulations of ground motion in the Los Angeles Basin due to the Mw 4.2 Hollywood and Yorba Linda earthquakes performed by Komatitsch et al. (2004), the authors used the SEM with 3-D variation of seismic wave speeds, density, and topography to build a model of the Los

Angeles sedimentary basin based on data from petroleum-industry well logs and seismic reflection profiles. The modeling predicted significant amplification in the basin, and a good match was obtained between the simulated waveforms and the real data at a frequency of 0.5 Hz. Given the results of Komatitsch et al. (2004) for the Los Angeles basin, it is possible that the basin model used in this work is too simple to reproduce the seismic effects of the Pampa del Tamarugal basin shown in the seismic data, and a more realistically complex basin model may produce better results.

On the other hand, in the present study, for frequencies higher than 1 Hz, the fit between the real and simulated waveforms deteriorates for all stations, and the simulations including topography and basins do not capture the complexity of the waveforms. This deterioration is probably due to the effects of shallow geological structures that are not accounted for in the simulations and which become more important at high frequencies.

Additionally, for frequencies lower than 1 Hz, the fit between the real and simulated waveforms also deteriorates with increasing epicentral distance, most noticeably for the 13 July 2014 earthquake, whose epicenter was located 20 km west of the coastal line and at a depth of 34 km, which leads to shallower source–receiver paths and are probably strongly affected by shallower crustal heterogeneity. A good example of the differences in the fit obtained for both earthquakes is station PSGCX, which shows an exceptional fit for the 02 April 2014 earthquake (located at a depth of 49 km) for frequencies between 0.1 and 1.0 Hz, but a poor fit for the 13 July 2014 earthquake (located at a depth of 34 km). In an attempt to improve the fit between the simulated and real waveforms for the 13 July earthquake, the 2-D velocity model with topography was implemented, however this did not improve the fit as explained before. Therefore, these results suggest that the 1-D crustal velocity structure is too simple for large source–station distances or shallow earthquakes and the constructed 2-D velocity model is not representative of the large-

scale variations of the 3-D crustal velocity structure. Hence, future studies should focus on the construction of detailed 3-D velocity models for the study region.

Although this work analyzes just two earthquakes with relatively low magnitudes (Mw 4.5 and Mw 5.4), the amplitudes of the secondary waves generated by topographic features and basins are larger for the Mw 5.4 earthquake than for the Mw 4.5. From this very simple observation, it is possible hypothesize that, due to the higher energy available for larger earthquakes, seismic amplification due to topography and basins is larger for higher-magnitude earthquakes. However, with just two examples, a numerical relationship between the amplification factor of the site effects and the earthquake's magnitude cannot be established. Therefore, further studies should analyze the relationship between earthquake magnitude and amplification using synthetic earthquakes.

In the same way, in this work, a clear relationship between amplification and frequency was shown, with larger amplifications being observed for higher frequencies, and this effect is likely to be related to the fundamental resonance frequency of basins and hills. Since some studies have shown that intraplate earthquakes have a higher frequency content and larger seismic energy (Leyton et al., 2009),such earthquakes should be studied in future works.

7.5. CONCEPTUAL MODEL OF SEISMIC SITE EFFECTS

Together, the aforementioned analysis suggests that the damage and seismic amplification observed in Alto Hospicio City during the 01 April 2014 Mw 8.1 Iquique earthquake may have been related not only to the combination of topography and basin effects and the earthquake's large magnitude, but also to a complex shallow structure or structures which were not accounted for in the simulations performed in this work.

Finally, as a summary of the seismic effects due to topography and basins which were observed in the simulations implemented in this work, a conceptual model (west–east profile) of the site effects in the study area is presented in **Figure 40**. This conceptual model shows the main geomorphological features and their relationship with ground motion amplification or deamplification.

Generally, it can be concluded that larger amplifications and deamplifications are related to the reflection of waves from basin borders, affecting both basins and basin-adjacent areas, and that these amplifications and deamplifications are related to the size of the basins (based on the observed differences between the Alto Hospicio and Pampa del Tamarugal basins).

On the other hand, secondary waves generated by topographic features lead to amplifications in the slopes and tops of topographic features and deamplifications in foothills. These secondary waves are especially important for the Coastal Cliff, due to its remarkable height, leading to considerable amplification within the Coastal Cordillera and deamplification in the Coastal Plains at frequencies between 0.1 and 0.5 Hz. Meanwhile, within the Coastal Cordillera, amplification and deamplification effects at frequencies of 1.0–3.5 Hz are produced by hills and valleys. Additionally, in the offshore region, amplifications corresponding spatially to seamounts are also observed in the whole frequency range considered.

Therefore, from the analyses of the results obtained in this work and the conceptualization of site effects presented in **Figure 38**, it is possible to suggest that intramountainous basins represent a major seismic hazard for the amplification of ground motion during earthquakes in the Iquique region due to the combined effects of basins and topography.

Accordingly, future works should further assess the seismic hazard in populated intramountainous basins located in the Coastal Cordillera along a distance of more than 1000

km between Southern Peru and Northern Chile, as they constitute an important seismic risk for future earthquakes in the region.

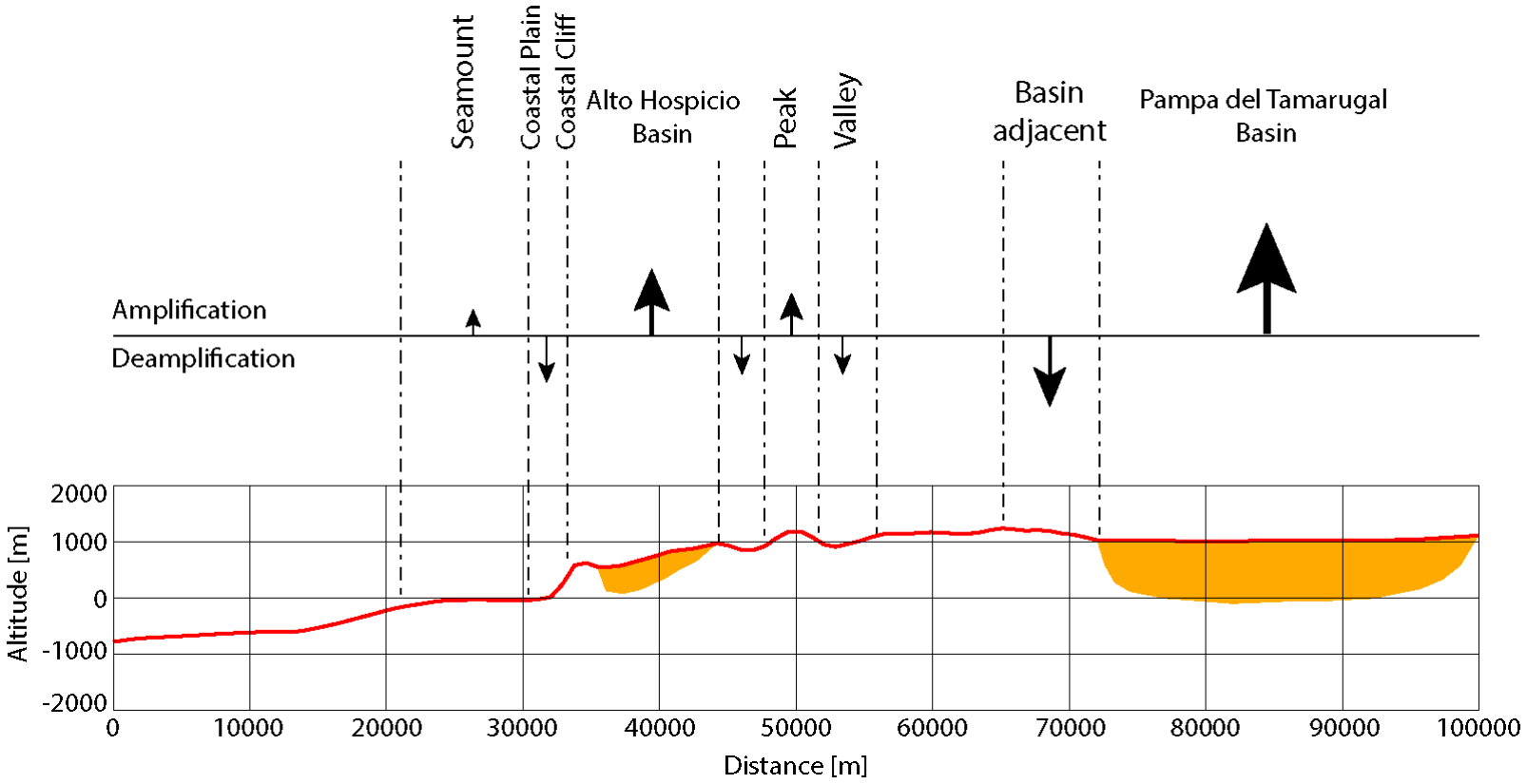

Figure 40: Conceptual model of the study region showing the simulated seismic amplification and deamplification in the study area and their association with topographic features and basins.

8. CONCLUSIONS

Assessing site effects is not simple. In recent decades, great efforts have been made to evaluate the amplification produced by the local surface geological and geomorphological features during earthquakes. The present study showed that simple numerical models are capable of estimating the amplifications generated by local geological conditions in a first order, but that the complexity of the interaction between topography and soil materials cannot be entirely reproduced by using such simple models. Despite this, some general insights into the nature of wave amplification under different scenarios were obtained.

In this work, a comprehensive study of the Iquique and Alto Hospicio area using geophysical and geological surveys were used to determine the geometrical and physical properties of the Alto Hospicio basin that were successfully represented in the numerical model. After a complete literature review of the geological and geophysical background of the Pampa del Tamarugal area, a first approximation of the northern part of the Pampa del Tamarugal basin was built and used in the numerical model. In the same way, two crustal velocity models for the Iquique area were implemented in the modeling.

From the analyses of the results obtained comparing a flat 1-D velocity model and a 1-D velocity model including topography, it is possible to conclude that topographic features do not significantly modify the incident waveform but rather produce frequency-dependent secondary waves that propagate inland; these waves prolong the duration of ground motion, and in some sites have larger amplitudes than the incident waves. These secondary waves augment the total energy of the seismic waveforms, producing amplification factors of up to 3.6 (i.e., an amplification of 260% relative to the flat 1-D model) for frequencies between 0.5 and 1 Hz.

In the same way, as has been reported in several previous works, from the comparison of the 1-D velocity model including topography with the 1-D velocity model with topography and basins, it is

possible to conclude that basins are the geomorphological features that produce the main amplification effects in seismic ground motion, both increasing the amplitudes of the incident seismic waves and augmenting the duration of the ground motion by generating secondary waves, where amplification factors (relative to the topographic 1-D model) of up to 3.9 were observed for frequencies between 1 and 2 Hz. However, in this work, the importance of the interaction between basins and topographic features was highlighted.

From the comparison between the real data and the synthetic waveforms produced with the 1-D velocity model with topography, the 1-D model with topography and basins, and the 2-D velocity model with topography, it was found that good fits were obtained for frequency ranges up to 1 Hz, and the fits progressively deteriorated with increasing frequency. Also, deterioration in the fit was found to be related to the source–station distance, notably for the shallower earthquake. These results indicate that the implemented velocity models may not entirely reproduce the more superficial velocity structures. Therefore, future works should focus on obtaining detailed seismic images of the fine shallow 3-D velocity structure of the Iquique region, which will be crucial to refining the simulations.

The conceptual model presented here summarizes the main amplification effects produced by the interaction between topography and basins in the study area, showing that the Alto Hospicio and Pampa del Tamarugal basins and the Coastal Cliff were the main cause of the seismic wave amplification, leading to the conclusion that the damage observed in the cities of Iquique and Alto Hospicio during the 01 April 2014 Mw 8.1 earthquake was likely related to the interaction between the surface geology (i.e., the Alto Hospicio basin) and the Coastal Cliff.

From this thesis, two publications were written; the first one related to the geological-geophysical conceptualization of the Alto Hospicio basin, published in the Journal Tectonophysics as *"Insights on the structural control of a Neogene forearc basin in Northern Chile: A geophysical approach"* (García-Pérez et al., 2018); and the second article in revision *"Effects of topography and basins on*

seismic wave amplification: the Northern Chile Coastal Cliff and Intra-mountainous basins", shows the numerical study that analyses the effects of topography and basins on seismic waves propagation using the spectral element method, for two earthquakes of the Mw 8.1 Iquique earthquake sequence.

REFERENCES

Aki, K. (1993). Local site effects on weak and strong ground motion. *Tectonophysics*, *218*, 93–111.

Aki, K., & Richards, P. G. (1980). *Quantitative Seismology. Theory and Methods*. (A. Cox, Ed.). San Francisco: W. H. Freeman and Company.

Allmendinger, R. W., & González, G. (2010). Invited review paper: Neogene to Quaternary tectonics of the coastal Cordillera, northern Chile. *Tectonophysics*, *495*(1–2), 93–110. https://doi.org/10.1016/j.tecto.2009.04.019

Allmendinger, R. W., González, G., Yu, J., Hoke, G., & Isacks, B. (2005a). Trench-parallel shortening in the Northern Chilean Forearc: Tectonic and climatic implications. *Bulletin of the Geological Society of America*, *117*(1–2), 89–104. https://doi.org/10.1130/B25505.1

Allmendinger, R. W., González, G., Yu, J., Hoke, G., & Isacks, B. (2005b). Trench-parallel shortening in the Northern Chilean Forearc: Tectonic and climatic implications. *Bulletin of the Geological Society of America*, *117*(1–2), 89–104. https://doi.org/10.1130/B25505.1

Álvarez-Rubio, S., Sánchez-Sesma, F. J., Benito, J. J., & Alarcón, E. (2004). The direct boundary element method: 2D site effects assessment on laterally varying layered media (methodology). *Soil Dynamics and Earthquake Engineering*, *24*(2), 167–180. https://doi.org/10.1016/j.soildyn.2003.09.003

ANCORP, & Oncken, O. (2006). Seismic imaging of a convergent continental margin and plateau in the central Andes (Andean Continental Research Project 1996, *108*(July), 1–25. https://doi.org/10.1029/2002JB001771

Arenas, A., González, K., Morales, L., Matamala, M., Soza, D., Cares, S., et al. (2013). *Levantamiento de Información Geofísica en la Región de Tarapacá*. *Ministerio de Obras Públicas. Direccion General de Aguas. Gobierno de Chile*.

Armijo, R., & Thiele, R. (1990). Active faulting in northern Chile: ramp stacking and lateral decoupling along a subduction plate boundary? *Earth and Planetary Science Letters*, *98*(1),

40–61. https://doi.org/10.1016/0012-821X(90)90087-E

Armijo, R., Lacassin, R., Coudurier-Curveur, A., & Carrizo, D. (2015). Coupled tectonic evolution of Andean orogeny and global climate. *Earth-Science Reviews*, *143*, 1–35. https://doi.org/10.1016/j.earscirev.2015.01.005

Ashford, S. A., Sitar, N., Lysmer, J., & Deng, N. (1997). Topographic effects on the seismic response of steep slopes. *Bulletin of the Seismological Society of America*, *87*(3), 701–709.

Barrientos, S. (2018). The Seismic Network of Chile. *Seismological Research Letters*, *89*(2A), 467–474. https://doi.org/10.1785/0220160195

Barrientos, S., & Ward, S. (1990). The 1960 Chile earthquake: inversion for slip distribution from surface deformation. *Geophysical Journal International*, *103*(3), 589–598. https://doi.org/10.1111/j.1365-246X.1990.tb05673.x

Becerra, A., Podestá, L., Monetta, R., Sáez, E., Leyton, F., & Yañez, G. (2015). Seismic microzoning of Arica and Iquique, Chile. *Natural Hazards*, *79*(1), 567–586. https://doi.org/10.1007/s11069-015-1863-y

Becerra, A., Sáez, E., Podest, L., & Leyton, F. (2016). The 2014 earthquake in Iquique, Chile: Comparison between local soil conditions and observed damage in the cities of iquique and Alto Hospicio. *Earthquake Spectra*, *32*(3), 1489–1505. https://doi.org/10.1193/111014EQS188M

Blanco, N., Vásquez, P., Sepúlveda, F., Tomlinson, A. J., Quezada, A., & Ladino, M. (2012). Levantamiento geológico para el fomento de la exploración de recursos minerales e hídricos de la Cordillera de la Costa, Depresión Central y Precordillera de la Región de Tarapacá (20º-21ºS). *Servicio Nacional de Geología y Minería. Gobierno Regional de Tarapacá*, 245.

Bloch, W., Kummerow, J., Salazar, P., Wigger, P., & Shapiro, S. A. (2014). High-resolution image of the North Chilean subduction zone : seismicity , reflectivity and fluids, 1744–1749. https://doi.org/10.1093/gji/ggu084

Boore, D. M. (1972). A note o the effects of simple topography on seismic SH waves. *Bulletin of the Seismological Society of America Society of America*, *62*(1), 275–284.

Borcherdt, R., & Glassmoyer, G. (1992). On the Characteristics of Local Geoloy and Their Influence on Ground Motions Generated by the Loma Prieta Earthquake in the San Francisco Bay Regio, California. *Bulletin of the Geological Society of America*, *82*(2), 603–641.

Borcherdt, R. D. (1970). Effects of Local Geology on Ground Motion Near San Francisco Bay. *Bulletin of the Seismological Society of America*, *60*(1), 29–61.

Bouchon, M, Schultz, C. A., & Toksoz, M. N. (1996). Effect of three-dimensional topography on seismic motion. *Journal of Geophysical Research*, *101*, 5835–5846.

Bouchon, Michel. (1973). Effect of topography on surface motion. *Bulletin of the Seismological Society of America*, *63*(2), 615–632.

Bouchon, Michel, Marsan, D., Durand, V., Campillo, M., Perfettini, H., Madariaga, R., & Gardonio, B. (2016). Potential slab deformation and plunge prior to the Tohoku, Iquique and Maule earthquakes. *Nature Geoscience*, *9*(5), 380–383. https://doi.org/10.1038/ngeo2701

Bouckovalas, G. D., & Kouretzis, G. P. (2001). Stiff soil amplification effects in the 7 September 1999 Athens (Greece) earthquake. *Soil Dynamics and Earthquake Engineering*, *21*(8), 671–687. https://doi.org/10.1016/S0267-7261(01)00045-8

Buech, F., Davies, T. R., & Pettinga, J. R. (2010). The little red hill seismic experimental study: Topographic effects on ground motion at a bedrock-dominated mountain edifice. *Bulletin of the Seismological Society of America*, *100*(5 A), 2219–2229. https://doi.org/10.1785/0120090345

Bürgmann, R. (2014). Earth science: Warning signs of the Iquique earthquake. *Nature*, *512*(7514), 258–259. https://doi.org/10.1038/nature13655

Burjánek, J., Edwards, B., & Fäh, D. (2014). Empirical evidence of local seismic effects at sites with pronounced topography: A systematic approach. *Geophysical Journal International*, *197*(1),

608–619. https://doi.org/10.1093/gji/ggu014

Campillo, M., Gariel, J. C., Aki, K., & Sánchez-Sesma, F. J. (1989). Destructive strong ground motion in Mexico City: source, path, and site effects during great 1985 Michoacan earthquake. *Bulletin of the Seismological Society of America*, *79*(6), 1718–1735.

Carrizo, D., González, G., & Dunai, T. (2008). Constricción neógena en la Cordillera de la Costa, norte de Chile: neotectónica y datación de superficies con 21Ne cosmogónico. *Revista Geológica de Chile*, *35*(1), 01–38. https://doi.org/10.4067/S0716-02082008000100001

Celebi, M. (1987). Topographical and geological amplifications determined from strong-motion and aftershock records of the 3 March 1985 Chile earthquake. *Bulletin of the Seismological Society of America*, *77*(4), 1147–1167.

Cembrano, J., González, G., Arancibia, G., Ahumada, I., Olivares, V., & Herrera, V. (2005). Fault zone development and strain partitioning in an extensional strike-slip duplex: A case study from the Mesozoic Atacama fault system, Northern Chile. *Tectonophysics*, *400*(1–4), 105–125. https://doi.org/10.1016/j.tecto.2005.02.012

Chlieh, M., De Chabalier, J. B., Ruegg, J. C., Armijo, R., Dmowska, R., Campos, J., & Feigl, K. L. (2004). Crustal deformation and fault slip during the seismic cycle in the North Chile subduction zone, from GPS and InSAR observations. *Geophysical Journal International*, *158*(2), 695–711. https://doi.org/10.1111/j.1365-246X.2004.02326.x

Chlieh, Mohamed, Perfettini, H., Tavera, H., Avouac, J. P., Remy, D., Nocquet, J. M., et al. (2011). Interseismic coupling and seismic potential along the Central Andes subduction zone. *Journal of Geophysical Research: Solid Earth*, *116*(12), 1–21. https://doi.org/10.1029/2010JB008166

Comte, D., Eisenberg, A., Lorca, E., Pardo, M., Ponce, L., Saragoni, R., et al. (1986). The 1985 Central Chile earthquake: A repeat of previous great earthquakes in the region? *Science*, *233*(4762), 449–453. https://doi.org/10.1126/science.233.4762.449

Comte, Diana, & Pardo, M. (1991). Reappraisal of great historical earthquakes in the northern Chile

and southern Peru seismic gaps. *Natural Hazards*, *4*(1), 23–44. https://doi.org/10.1007/BF00126557

Comte, Diana, & Suárez, G. (1995). Stress distribution and geometry of the subducting Nazca plate in northern Chile using teleseismically recorded earthquakes. *Geophysical Journal International*, *122*(2), 419–440. https://doi.org/10.1111/j.1365-246X.1995.tb07005.x

Contreras-Reyes, E., Jara, J., Grevemeyer, I., Ruiz, S., & Carrizo, D. (2012). Abrupt change in the dip of the subducting plate beneath north Chile. *Nature Geoscience*, *5*(5), 342–345. https://doi.org/10.1038/ngeo1447

Day, S. M., Graves, R., Bielak, J., Dreger, D., Larsen, S., Olsen, K. B., et al. (2008). Model for basin effects on long-period response spectra in southern California. *Earthquake Spectra*, *24*(1), 257–277. https://doi.org/10.1193/1.2857545

Dentith, M., & Mudge, S. T. (2014). *Geophysics for the Mineral Exploration Geoscientist*. Cambridge University Press.

Faccioli, E. (1991). Seismic amplification in the presence of geological and topographic irregularities. *Proceedings of the 2nd International Conference on Recent Advances in Geotechnical Earthquake Engineering and Soil Dynamics*, *2*, 1779–1797.

Fan, G., Liu, F. C., Wen, R. Z., & Zhang, J. J. (2014). Research of Earthquake Topographic Effect. *Applied Mechanics and Materials*, *501–504*, 1566–1572. https://doi.org/10.4028/www.scientific.net/amm.501-504.1566

Farías, M., Charrier, R., Comte, D., Martinod, J., & Hérail, G. (2005). Late Cenozoic deformation and uplift of the western flank of the Altiplano: Evidence from the depositional, tectonic, and geomorphologic evolution and shallow seismic activity (northern Chile at 19°30′S). *Tectonics*, *24*(4), 1–27. https://doi.org/10.1029/2004TC001667

Field, E. H. (1996). Spectral amplification in a sediment-filled valley exhibiting clear basin-edge-induced waves. *Bulletin of the Seismological Society of America*, *86*(4), 991–1005.

Fitterman, D. V., & Stewartj, M. T. (1986). Transient electromagnetic sounding for groundwater. *Geophysics*, *51*(4), 995–1005. https://doi.org/10.1190/1.1442158

Frankel, A. D., Carver, D. L., & Williams, R. A. (2002). Nonlinear and linear site response and basin effects in Seattle for the M 6.8 Nisqually, Washington, earthquake. *Bulletin of the Seismological Society of America*, *92*(6), 2090–2109. https://doi.org/10.1785/0120010254

García-Pérez, T., Marquardt, C., Yáñez, G., Cembrano, J., Gomila, R., Santibañez, I., & Maringue, J. (2018). Insights on the structural control of a Neogene forearc basin in Northern Chile: A geophysical approach. *Tectonophysics*, *736*(March), 1–14. https://doi.org/10.1016/j.tecto.2018.04.003

Garzione, C. N., Hoke, G. D., Libarkin, J. C., Withers, S., MacFadden, B., Eiler, J., et al. (2008). Rise of the Andes. *Science*, *320*(5881), 1304–1307. https://doi.org/10.1126/science.1148615

Geli, L., Bard, P. Y., & Jullien, B. (1988a). Effect of Topography on Earthquake Ground Motion: a Review and New Results. *Bulletin of the Seismological Society of America*, *78*(1), 42–63.

Geli, L., Bard, P.-Y., & Jullien, B. (1988b). The effect of topography on earthquake ground motion: A review and new results. *Bull. Seism. Soc. Am.*, *78*(1), 42–63. https://doi.org/10.1016/0148-9062(88)90024-1

Geosciences, G. G. R. C. for, & CNRS-INSU, I. des S. de l'Univers-C. N. de la R. (2006). IPOC Seismic Network. https://doi.org/doi:10.14470/PK615318

González, G., Cembrano, J., Carrizo, D., Macci, A., & Schneider, H. (2003). The link between forearc tectonics and Pliocene-Quaternary deformation of the Coastal Cordillera, northern Chile. *Journal of South American Earth Sciences*, *16*(5), 321–342. https://doi.org/10.1016/S0895-9811(03)00100-7

González, G., Gerbault, M., Martinod, J., Cembrano, J., Carrizo, D., Allmendinger, R., & Espina, J. (2008). Crack formation on top of propagating reverse faults of the Chuculay Fault System, northern Chile: Insights from field data and numerical modelling. *Journal of Structural*

Geology, *30*(6), 791–808. https://doi.org/10.1016/j.jsg.2008.02.008

González, G., Salazar, P., Loveless, J. P., Allmendinger, R. W., Aron, F., & Shrivastava, M. (2015). Upper plate reverse fault reactivation and the unclamping of the megathrust during the 2014 northern Chile earthquake sequence. *Geology*, *43*(8), 671–674. https://doi.org/10.1130/G36703.1

Hartley, A. J., & Evenstar, L. (2010). Cenozoic stratigraphic development in the north Chilean forearc: Implications for basin development and uplift history of the Central Andean margin. *Tectonophysics*, *495*(1–2), 67–77. https://doi.org/10.1016/j.tecto.2009.05.013

Hayes, G. P., Myers, E. K., Dewey, J. W., Briggs, R. W., Earle, P. S., Benz, H. M., et al. (2017). Tectonic summaries of magnitude 7 and greater earthquakes from 2000 to 2015. *U.S. Geological Survey Open-File Report*, *2016–1192*, 148.

Hayes, Gavin P., Herman, M. W., Barnhart, W. D., Furlong, K. P., Riquelme, S., Benz, H. M., et al. (2014). Continuing megathrust earthquake potential in Chile after the 2014 Iquique earthquake. *Nature*, *512*(7514), 295–298. https://doi.org/10.1038/nature13677

Herrera, S., Pinto, L., Deckart, K., Cortés, J., & Valenzuela, J. I. (2017). Evolución tectonoestratigráfica y arquitectura cenozoica de los Andes Centrales en el norte de Chile, región de Aquine, Cordillera Occidental (19°-19°30’ S). *Andean Geology*, *44*(2), 87–122. https://doi.org/10.5027/andgeoV44n2-a01

Hervé, F., Godoy, E., Parada, M. A., Ramos, V., Rapela, C., Mpodozis, C., & Davidson, J. (1987). A general view on the Chilean-Argentine Andes, with emphasis on their early history. *American Geophysical Union*, *18*, 97–113. https://doi.org/10.1029/gd018p0097

Hough, S. E., Altidor, J. R., Anglade, D., Given, D., Janvier, M. G., Maharrey, J. Z., et al. (2010). Localized damage caused by topographic amplification during the 2010 Mw 7.0 Haiti earthquake. *Nature Geoscience*, *3*(11), 778–782. https://doi.org/10.1038/ngeo988

Houston, J. (2002). Groundwater recharge through an alluvial fan in the Atacama Desert, northern

Chile: Mechanisms, magnitudes and causes. *Hydrological Processes*, *16*(15), 3019–3035. https://doi.org/10.1002/hyp.1086

Von Huene, R., Weinrebe, W., & Heeren, F. (1999). Subduction erosion along the North Chile margin. *Journal of Geodynamics*, *27*(3), 345–358. https://doi.org/10.1016/S0264-3707(98)00002-7

Humire, F., Sáez, E., Leyton, F., & Yañez, G. (2015). Combining active and passive multi-channel analysis of surface waves to improve reliability of VS30 estimation using standard equipment. *Bulletin of Earthquake Engineering*, *13*(5), 1303–1321. https://doi.org/10.1007/s10518-014-9662-5

Husen, S., Kissling, E., Flueh, E., & Asch, G. (1999). Accurate hypocentre determination in the seismogenic zone of the subducting Nazca Plate in northern Chile using a combined on-/offshore network. *Geophysical Journal International*, *138*, 687–701.

Jordan, T. E., Burns, W. M., Veiga, R., Pangaro, F., Copeland, P., & Mpodozis, C. (2001). Extension and basin formation in the southern Andes caused by increased convergence rate. *Tectonics*, *20*(3), 308–424. https://doi.org/10.1029/1999TC001181

Jordan, T. E., Nester, P. L., Blanco, N., Hoke, G. D., Dávila, F., & Tomlinson, A. J. (2010). Uplift of the Altiplano-Puna plateau: A view from the west. *Tectonics*, *29*(5). https://doi.org/10.1029/2010TC002661

Kendrick, E., Bevis, M., Smalley, R., Brooks, B., Vargas, R. B., Lauría, E., & Fortes, L. P. S. (2003). The Nazca-South America Euler vector and its rate of change. *Journal of South American Earth Sciences*, *16*(2), 125–131. https://doi.org/10.1016/S0895-9811(03)00028-2

Komatitsch, D., & Tromp, J. (1999). Introduction to the spectral element method for three-dimensional seismic wave propagation. *Geophysical Journal International*, *139*, 806–822.

Komatitsch, D., & Vilotte, J. P. (1998). The Spectral Element Method : An Efficient Tool to Simulate the Seismic Response of 2D and 3D Geological Structures. *Bulletin of the Seismological Society*

of America, *88*(2), 368–392. Retrieved from http://bssa.geoscienceworld.org/content/88/2/368.short

Komatitsch, D., Vilotte, J. P., Vai, R., Castillo-Covarruvias, J., & Sánchez-Sesma, F. J. (1999). The Spectral Element Method for Elastic Wave Equations — Application to 2-D and 3-D Seismic Problems. *International Journal for Numerical Methods in Engineering*, *1164*, 1139–1164.

Komatitsch, D., Liu, Q., Tromp, J., Su, P., Stidham, C., & Shaw, J. H. (2004). Simulations of Ground Motion in the Los Angeles Basin Based upon the Spectral-Element Method. *Bulletin of the Seismological Society of America*, *94*(1), 187–206.

Komatitsch, D., Erlebacher, G., Göddeke, D., & Michéa, D. (2010). High-order finite-element seismic wave propagation modeling with MPI on a large GPU cluster. *Journal of Computational Physics*, *229*(20), 7692–7714. https://doi.org/10.1016/j.jcp.2010.06.024

Kozhevnikov, N., Sharlov, M., Sharlov, R., Stefanenko, S., & Agafonov, Y. (2016). Turn-Off Waveform of Large and Small Transmitter Loop Currents. In *23rd Electromagnetic Induction in the Earth Workshop*. https://doi.org/10.1016/j.rgg.2008.09.004

Lamb, S., & Davis, P. (2003). Cenozoic climate change as a possible cause for the rise of the Andes. *Nature*, *425*(6960), 792–797. https://doi.org/10.1038/nature02049

Lay, T., Yue, H., Brodsky, E. E., & An, C. (2014). The 1 April 2014 Iquique, Chile, Mw 8.1 earthquake rupture sequence. *Geophysical Research Letters*, *7*(April), 1–8. https://doi.org/10.1002/2014GL060238.Received

Lee, S. J., Chan, Y. C., Komatitsch, D., Huang, B. S., & Tromp, J. (2009). Effects of realistic surface topography on seismic ground motion in the Yangminshan region of Taiwan based upon the spectral-element method and LiDAR DTM. *Bulletin of the Seismological Society of America*, *99*(2 A), 681–693. https://doi.org/10.1785/0120080264

León-Ríos, S. (2015). *Análisis de la Distribución Espacial de la Sismicidad Precursora y Post Sísmica del Terremoto Mw 8.1 de Iquique 2014*. Universidad de Chile.

León-Ríos, S., Ruiz, S., Maksymowicz, A., Leyton, F., Fuenzalida, A., & Madariaga, R. (2016). Diversity of the 2014 Iquique's foreshocks and aftershocks: clues about the complex rupture process of a Mw 8.1 earthquake. *Journal of Seismology*, *20*(4), 1059–1073. https://doi.org/10.1007/s10950-016-9568-6

Lermo, J., & Chávez-García, F. (1993). Site Effect Evaluation Using Spectral Ratios with Only One Stations. *Bulletin of the Seismological Society of America*, *83*(N°5), 1574–1594.

Leyton, F., Ruiz, S., Sepúlveda, S. A., Contreras, J. P., Rebolledo, S., & Astroza, M. (2013). Microtremors' HVSR and its correlation with surface geology and damage observed after the 2010 Maule earthquake (Mw 8.8) at Talca and Curicó, Central Chile. *Engineering Geology*, *161*, 26–33. https://doi.org/10.1016/j.enggeo.2013.04.009

Leyton, Felipe, Ruiz, J., Campos, J., & Kausel, E. (2009). Intraplate and interplate earthquakes in Chilean subduction zone: A theoretical and observational comparison. *Physics of the Earth and Planetary Interiors*, *175*(1–2), 37–46. https://doi.org/10.1016/j.pepi.2008.03.017

Lomnitz, C. (2004). Major earthquakes of Chile: A historical survey, 1535-1960. *Seismological Research Letters*, *75*(3), 368–378. https://doi.org/10.1785/gssrl.75.3.368

López, L. A., Cifuentes, J. L., Fuentes, F. C., Neira, H. A., Cervetto, M. M., Troncoso, R. A., & Feuker, P. (2017). Hidrogeología de la Cuenca de la Pampa del Tamarugal, Región de Tarapacá. *Servicio Nacional de Geología y Minería. Carta Geológica de Chile. Serie Hidrogeología*, (6), 186.

Magaritz, M., Aravena, R., Peña, H., Suzuki, O., & Grilli, A. (1990). Source of Ground Water in the Deserts of Northern Chile: Evidence of deep Circulation of Ground Water from the Andes. *Ground Water*, *28*(4).

Marquardt, C., Lavenu, A., Ortlieb, L., Godoy, E., & Comte, D. (2004). Coastal neotectonics in Southern Central Andes: Uplift and deformation of marine terraces in Northern Chile (27°S). *Tectonophysics*, *394*(3–4), 193–219. https://doi.org/10.1016/j.tecto.2004.07.059

Marquardt, C., Marinovic, N., & Munoz, V. (2008). Geología de las ciudades de Iquique y Alto Hospicio, Región de Tarapacá. *Servicio Nacional de Geología y Minería, Carta Geológica de Chile, Serie Geología Básica*, *133*(33), 1. https://doi.org/mapa escala 1:25.000. Santiago

Martinod, J., Regard, V., Riquelme, R., Aguilar, G., Guillaume, B., Carretier, S., et al. (2016). Pleistocene uplift , climate and morphological segmentation of the Northern Chile coasts (24° S-32° S): insights from cosmogenic 10Be dating of paleoshorelines. *Geomorphology*, *274*, 78–91. https://doi.org/10.1016/j.geommph.2016.09.010

Massa, M., Lovati, S., D'Alema, E., Ferretti, G., & Bakavoli, M. (2010). An experimental approach for estimating seismic amplification effects at the top of a ridge, and the implication for ground-motion predictions: The case of Narni, Central Italy. *Bulletin of the Seismological Society of America*, *100*(6), 3020–3034. https://doi.org/10.1785/0120090382

Métois, M., Socquet, A., Vigny, C., Carrizo, D., Peyrat, S., Delorme, A., et al. (2013). Revisiting the North Chile seismic gap segmentation using GPS-derived interseismic coupling. *Geophysical Journal International*, *194*(3), 1283–1294. https://doi.org/10.1093/gji/ggt183

Miksat, J., Wen, K. L., Wenzel, F., Sokolov, V., & Chen, C. T. (2010). Numerical modelling of ground motion in the Taipei Basin: Basin and source effects. *Geophysical Journal International*, *183*(3), 1633–1647. https://doi.org/10.1111/j.1365-246X.2010.04818.x

Mortimer, C., & Saric Rendic, N. (1975). Cenozoic studies in northernmost Chile. *Geologische Rundschau*, *64*(1), 395–420. https://doi.org/10.1007/BF01820676

Muñoz, N., & Charrier, R. (1996). Uplift of the western border of the Altiplano on a west-vergent thrust system, Northern Chile. *Journal of South American Earth Sciences*, *9*(3–4), 171–181. https://doi.org/10.1016/0895-9811(96)00004-1

Nester, P. (2008). *Basin and Paleoclimate Evolution of the Pampa del Tamarugal Forearc Valley, Atacama Desert, Northern Chile*. https://doi.org/10.1016/j.cell.2009.01.043

Nester, P., & Jordan, T. (2012). The Pampa del Tamarugal Forearc Basin in Northern Chile: The

Interaction of Tectonics and Climate. *Tectonics of Sedimentary Basins: Recent Advances*, 369–381. https://doi.org/10.1002/9781444347166.ch18

Niemeyer, H., González, G., & Martínez-De Los Ríos, E. (1996). Evolución tectónica cenozoica del margen continental activo de Antofagasta , norte de Chile. *Revista Geologica de Chile*, *23*(2), 165–186.

Olsen, K. B. (2000). Site amplification in the Los Angeles basin from three-dimensional modeling of ground motion. *Bulletin of the Seismological Society of America*, *90*(6 SUPPL.). https://doi.org/10.1785/0120000506

Oncken, O., Chong, G., Franz, G., Giese, P., Götze, H. J., Ramos, V. A., et al. (2006). *The Andes. Active Subductio Orogeny*.

Ortlieb, L., Zazo, C., Goy, J. L., Hillaire-Marcel, C., Ghaleb, B., & Cournoyer, L. (1996). Coastal deformation and sea-level changes in the northern Chile subduction area (23°S) during the last 330 ky. *Quaternary Science Reviews*, *15*(8–9), 819–831. https://doi.org/10.1016/S0277-3791(96)00066-2

Paolucci, R. (2002). Amplification of earthquake ground motion by steep topographic irregularities. *Earthquake Engineering and Structural Dynamics*, *31*(10), 1831–1853. https://doi.org/10.1002/eqe.192

Paolucci, R., & Morstabilini, L. (2006). Non-Dimensional Site Amplification Functions for Basin Edge Effects on Seismic Ground Motion. *Third International Symposium on the Effects of Surface Geology on Seismic Motion*, (September), 823–831.

Park, C. B., & Miller, R. D. (2008). Roadside passive multichannel analysis of surface waves (MASW). *Journal of Environmental and Engineering Geophysics*, *13*(1), 1–11. https://doi.org/10.2113/JEEG13.1.1

Park, C. B., Miller, R. D., & Xia, J. (1999). Multichannel analysis of surface waves. *Geophysics*, *64*(3), 800–808. https://doi.org/10.1190/1.1444590

Paskoff, R. P. (1978). Sobre la evolución geomorfológica del gran acantilado costero del Norte Grande de Chile. *Géographie Physique et Quaternaire*, *32*(4), 351. https://doi.org/10.7202/1000333ar

Paterson, N. R., & Reeves, C. V. (1985). Applications of gravity and magnetic surveys : The state of the art in 1985. *Geophysics*, *50*(12), 2558–2594.

Pedersen, H. . A., Sánchez-Sesma, F. J., & Campillo, M. (1994). Three-Dimensional Scattering by Two-Dimensional Topographies. *Bulletin of the Seismological Society of America*, *84*(4), 1169–1183. Retrieved from http://www.bssaonline.org/content/84/4/1169.short

Plouff, D. (1976). Gravity and magnetics fields of polygonal prisms and application to magnetic terrain corrections. *Geophysics*, *41*(4), 727–741.

Quezada, J., Cerda, J. L., & Jensen, A. (2010). Efectos de la tectónica y el clima en la configuración morfológica del relieve costero del norte de Chile. *Andean Geology*, *37*(1), 78–109. https://doi.org/10.4067/S0718-71062010000100004

Ramos, V. A. (2009). Anatomy and global context of the Andes: Main geologic features and the Andean orogenic cycle. *Memoir of the Geological Society of America*, *204*(02), 31–65. https://doi.org/10.1130/2009.1204(02)

Restrepo, D., Bielak, J., Serrano, R., Gómez, J., & Jaramillo, J. (2016). Effects of realistic topography on the ground motion of the Colombian Andes - A case study at the Aburrá Valley, Antioquia. *Geophysical Journal International*, *204*(3), 1801–1816. https://doi.org/10.1093/gji/ggv556

Rietbrock, A., & Waldhauser, F. (2004). A narrowly spaced double-seismic zone in the subducting Nazca plate. *Geophysical Research Letters*, *31*(10), 2–5. https://doi.org/10.1029/2004GL019610

Roquer, T., Arancibia, G., Rowland, J., Estay, N. P., & Yáñez, G. (2016). Geoelectricity , Faults and Mineralogy : an Experiment from Exposed Fault-Controlled Hydrothermal Systems in the Southern Andes. *Proceedings 38th New Zealand Geothermal Workshop*, (November).

Ruiz, S., Metois, M., Fuenzalida, A., Ruiz, J., Leyton, F., Grandin, R., et al. (2014). Intense foreshocks and a slow slip event preceded the 2014 Iquique Mw 8.1 earthquake. *Science*, *345*(6201), 1165–1169.

Sánchez-Sesma, F. J., & Campillo, M. (1993). Topographic effects for incident P, SV and Rayleigh waves. *Tectonophysics*, *218*(1–3), 113–125. https://doi.org/10.1016/0040-1951(93)90263-J

Sánchez-Sesma, F. J., Palencia, V. J., & Luzón, F. (2002). Estimation of Local Site Effects during Earthquakes: An Overview. *ISET Journal of Earthquake Technology*, *39*(423), 167–193.

Scheuber, E., & González, G. (1999). Tectonics of the Jurassic-Early Cretaceous magmatic arc of the north Chilean Coastal Cordillera (22°–26°S): A story of crustal deformation along a convergent plate boundary. *Tectonics*, *18*(5), 895. https://doi.org/10.1029/1999TC900024

Semblat, J. F., Duval, A. M., & Dangla, P. (2002). Seismic site effects in a deep alluvial basin: numerical analysis by the boundary element method. *Computers and Geotechnics*, *29*, 573–585.

Semblat, J. F., Kham, M., Parara, E., Bard, P. Y., Pitilakis, K., Makra, K., & Raptakis, D. (2005). Seismic wave amplification: Basin geometry vs soil layering. *Soil Dynamics and Earthquake Engineering*, *25*(7–10), 529–538. https://doi.org/10.1016/j.soildyn.2004.11.003

Sepúlveda, F., & Vásquez, P. (2015). El Grupo Huantajaya : Nuevo esquema estratigráfico para las unidades de la cuenca de trasarco jurásica en la Cordillera de la Costa del área de Iquique (20 ° -21 ° S). *XIV Congreso Geológico Chileno*, 643–645.

Sepúlveda, N. (2014). *Caracterización de estructuras con evidencia de deformación cuaternaria para la estimación del peligro sísmico en las ciudades de Iquique y Alto Hospicio*. Universidad de Concepción.

SERNAGEOMIN. (2003). Mapa geologico de chile: version digital. *Mapa Geológico de Chile: Versión Digital. Servicio Nacional de Geología y Minería*, *Publicacio*, (CD-ROM, versión 1.0) Santiago. Retrieved from

http://geoportal.sernageomin.cl/geovisor/GeoVisor/index.html?resources=map:ags@http://geoarcgis.sernageomin.cl/ArcGIS/rest/services/geoportal/GeologiaBase/MapServer

Sharlov, M. V. (2017). An Integrated Approach to the Processing and Inversion of TEM Data. *Devices and Systems of Exploration Geophysics (in Russian)*, *2*, 24–36.

Sharlov, M. V., Agafonov, Y. A., & Stefanenko, S. M. (2010). Modern Telemetric Electroprospecting Equipment SGS-TEM and FastSnap. *Efficiency and Experience of Applying Devices and Systems of Exploration Geophysics (in Russian)*, *31*, 27–31.

Sharlov, M. V., Buddo, I. V., Misurkeeva, N. V., Shelokhov, I. A., & Agafonov, Y. A. (2017). Experience of Applying TEM for the Effective Study of Shallow part of the Section with FastSnap Equipment. *Devices and Systems of Exploration Geophysics (in Russian)*, *2*, 8–23.

Singh, S. K., Mena, E., & Castro, R. (1988). Some Aspects of Source Characteristics of the 19 September 1985 Michoacan Earthquake and Ground Motion Amplification in and Near Mexico City From Strong Motion Data. *Bulletin of the Seismological Society of America*, *78*(2), 451–477. https://doi.org/10.1017/CBO9781107415324.004

Spies, B. R. (1989). Depth of investigation in electromagntic soundings methods. *Geophysics*, *64*(7), 872–888.

Tassara, A., & Yáñez, G. (2003). Relación entre el espesor elástico de la litosfera y la segmentación tectónica del margen andino (15-47°S). *Revista Geológica de Chile*, *30*(2), 59–186.

Teldford, W. M., Geldart, L. P., & Sheriff, R. E. (1990). *Applied Geophysics*. (C. U. Press, Ed.) (2nd ed.). Cambridge University Press.

Thompson, G. A. (1959). Gravity Measurements between Hazen and Austin , Nevada: A Study of Basin-Range Structure. *Journal of Geophysical Research*, *64*(2), 217–229.

Tolorza, V., Marquardt, C., & Vargas, G. (2009). Sobre la edad del Gran Escarpe Costero. In *XII Congreso Geológico Chileno* (p. S10_040).

Udías, A., & Mezcua, J. (1997). *Fundamentos de Geofísica*. Madrid: Alianza Editorial S.A.

Vásquez, P., & Sepúlveda, F. (2013). Cartas Iquique y Pozo Almonte, Región de Tarapacá. Servicio Nacional de Geologia y Mineria. *Carta Geológica de Chile, Serie Geología Básica*, *Santiago*(1 mapa escala 1:100.000), 162–163.

Victor, P., Oncken, O., & Glodny, J. (2004). Uplift of the western Altiplano plateau: Evidence from the Precordillera between 20°and 21°S (northern Chile). *Tectonics*, *23*(4). https://doi.org/10.1029/2003TC001519

Viguier, B., Jourde, H., Yáñez, G., Lira, E. S., Leonardi, V., Moya, C. E., et al. (2018). Journal of South American Earth Sciences Multidisciplinary study for the assessment of the geometry , boundaries and preferential recharge zones of an overexploited aquifer in the Atacama. *Journal of South American Earth Sciences*, *86*(June), 366–383. https://doi.org/10.1016/j.jsames.2018.05.018

Yáñez, G., Muñoz, M., Flores-Aqueveque, V., & Bosch, A. (2015). Profundidad del basamento derivado de la gravedad en la Cuenca de Santiago: Implicancias para la evolución geológica, hidrogeológica, geotermia de baja entalpía, caracterización de suelos y peligros geológicos. *Andean Geology*, *42*(2), 147–172. https://doi.org/10.5027/andgeoV42n2-a01

SUPPLEMENTARY MATERIAL

APPENDIX 1: TOPOGRAPHIC MODEL

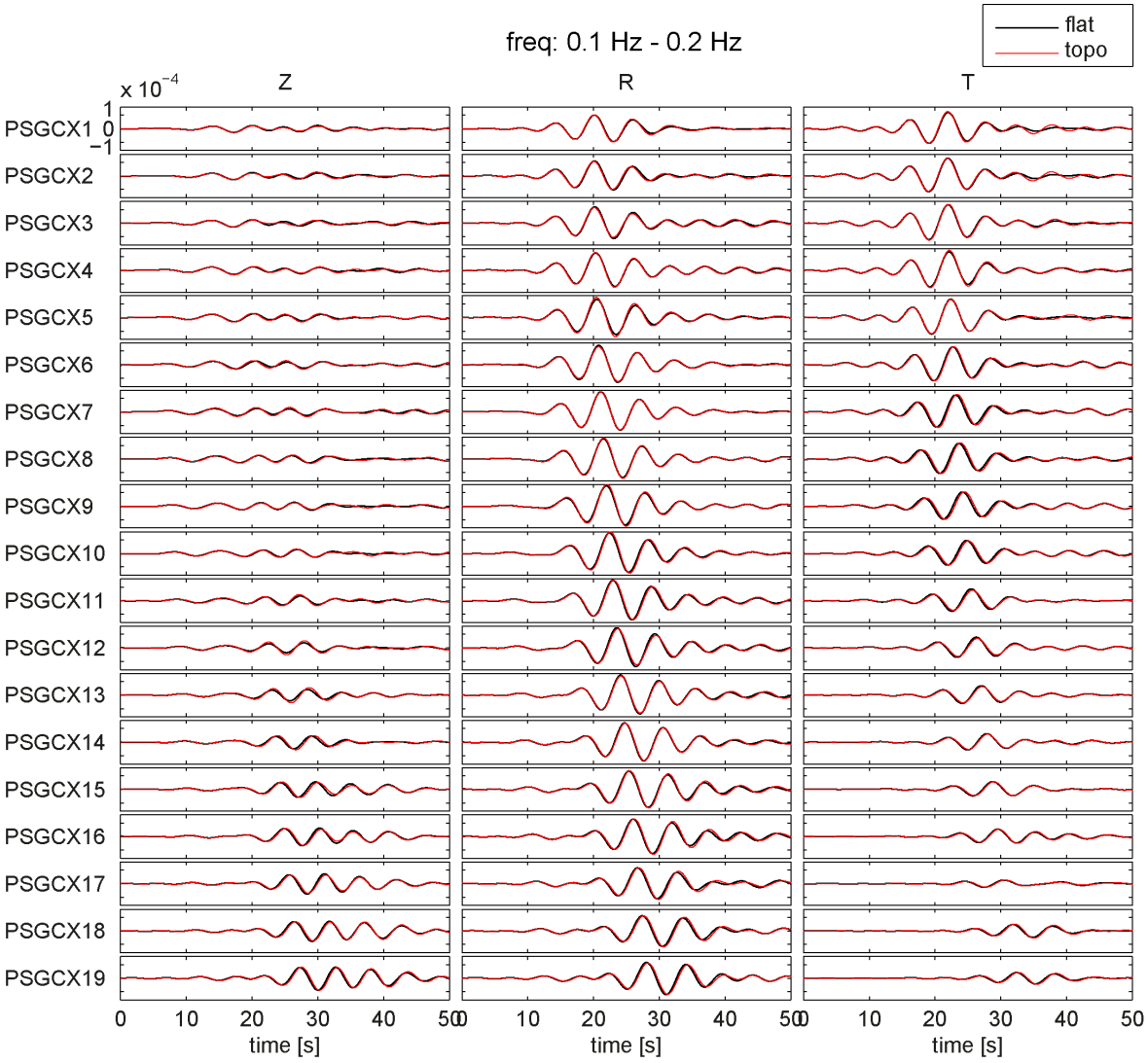

Figure S1: Comparison of synthetic seismograms computed using the 1-D flat model (black line) and the 1-D model with topography (red line). The synthetic seismograms are all bandpass filtered between 0.5 and 1.0 Hz. The processed waveforms for the vertical (left), radial (middle) and transverse (right) components are shown for the 19 stations along profile PSGCX (see location in Figure 27).

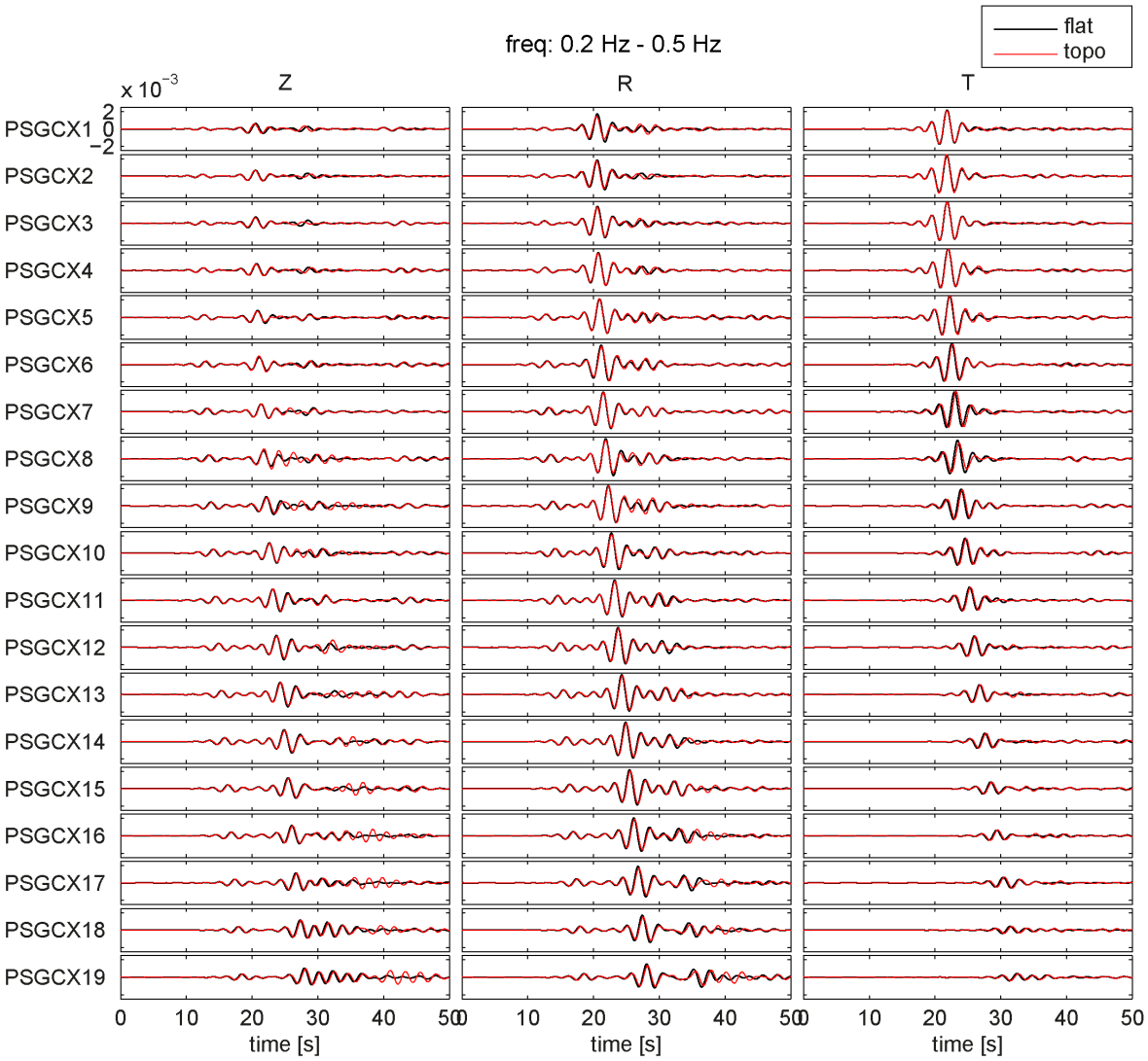

Figure S2: Comparison of synthetic seismograms computed using the 1-D flat model (black line) and the 1-D model with topography (red line). The synthetic seismograms are all bandpass filtered between 1.0 and 2.0 Hz. The processed waveforms for the vertical (left), radial (middle) and transverse (right) components are shown for the 19 stations along profile PSGCX (see location in Figure 27).

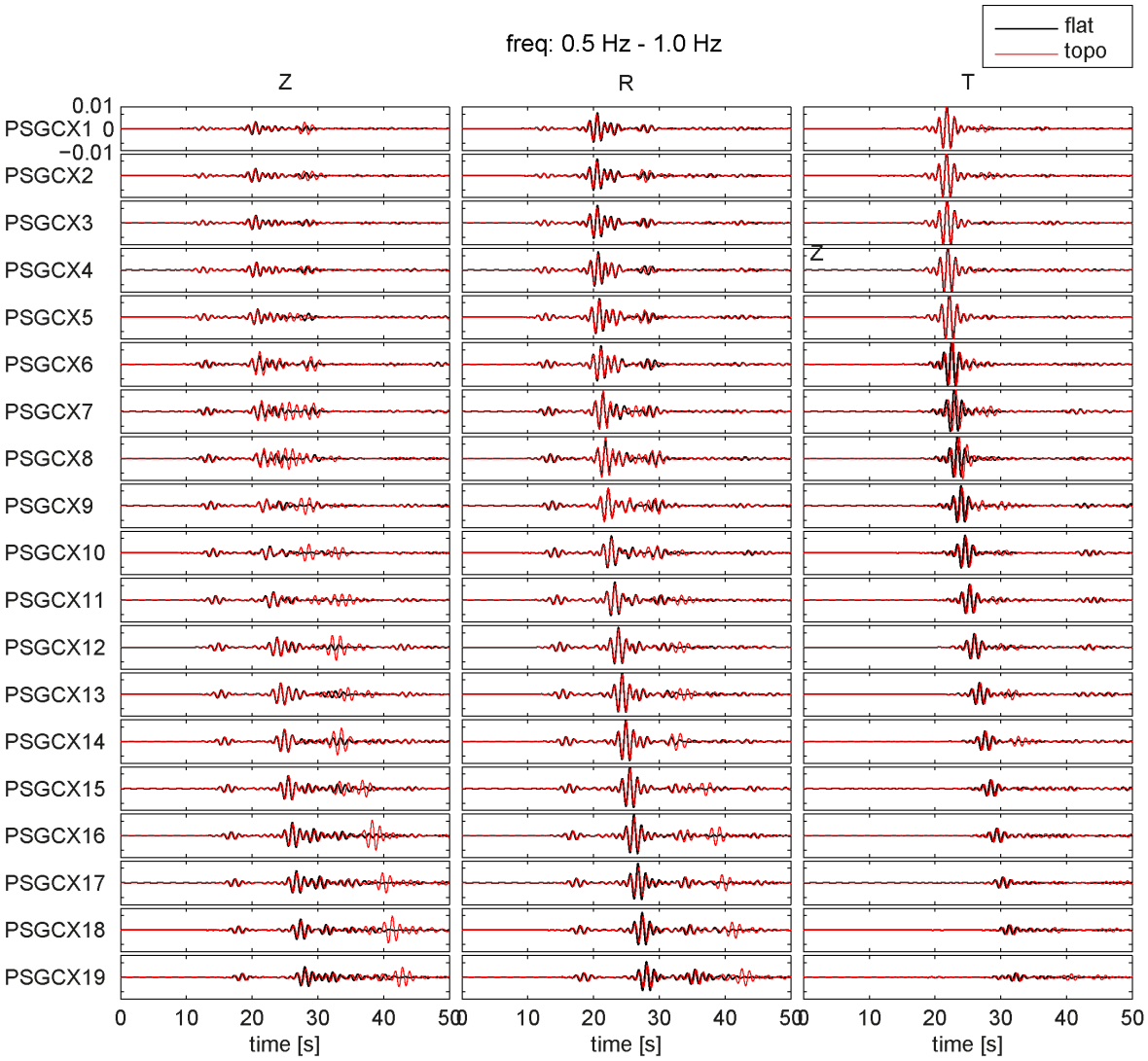

Figure S3: Comparison of synthetic seismograms computed using the 1-D flat model (black line) and the 1-D model with topography (red line). The synthetic seismograms are all bandpass filtered between 0.5 and 1.0 Hz. The processed waveforms for the vertical (left), radial (middle) and transverse (right) components are shown for the 19 stations along profile PSGCX (see location in Figure 27).

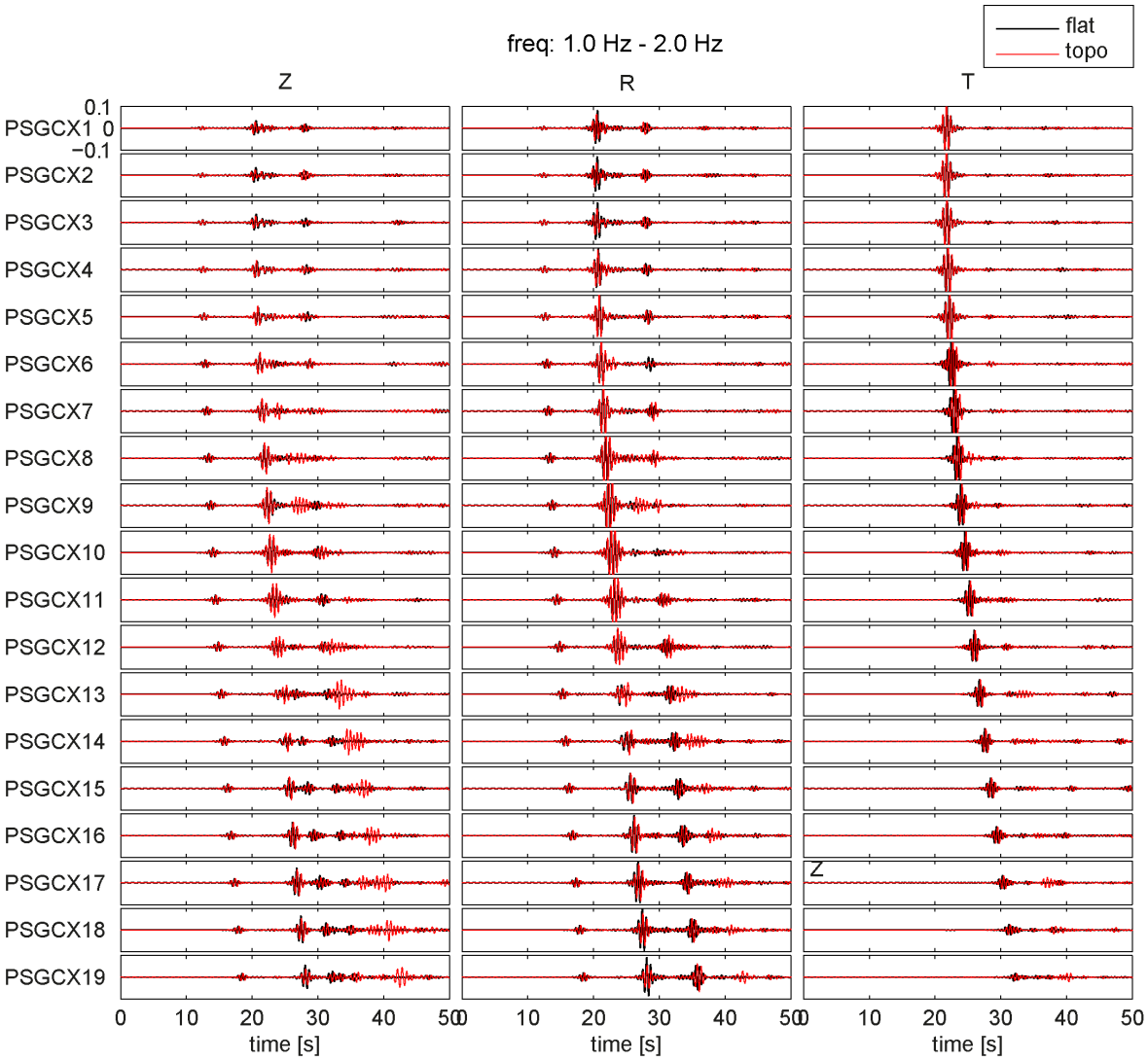

Figure S4: Comparison of synthetic seismograms computed using the 1-D flat model (black line) and the 1-D model with topography (red line). The synthetic seismograms are all bandpass filtered between 1.0 and 2.0 Hz. The processed waveforms for the vertical (left), radial (middle) and transverse (right) components are shown for the 19 stations along profile PSGCX (see location in Figure 27).

APPENDIX 2: BASIN MODEL

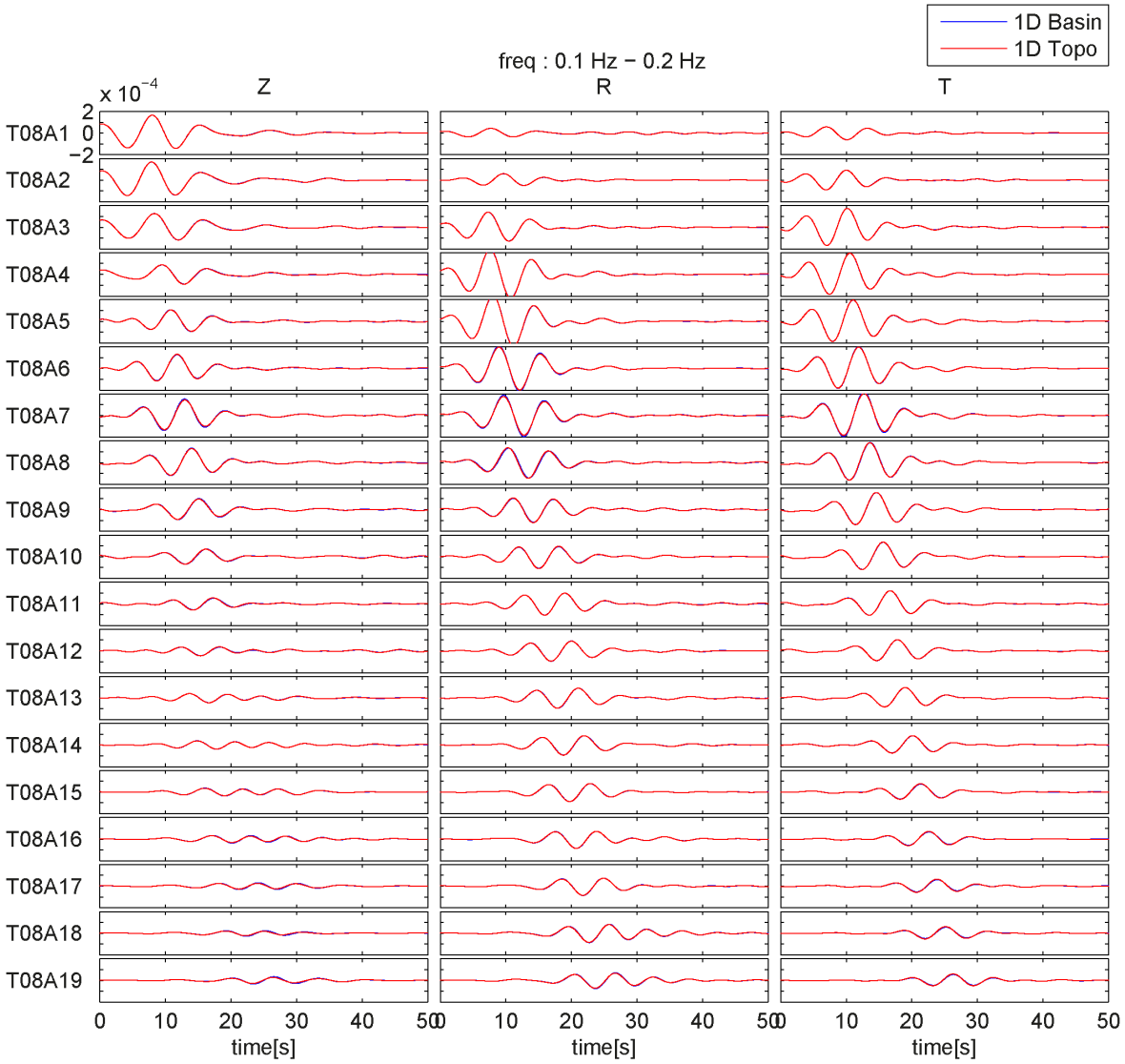

Figure S5: Comparison of synthetic seismograms computed using the 1-D topography model (red line) and the 1-D topography with basin model (blue line). The synthetic seismograms are all bandpass filtered between 0.1 and 0.2 Hz. The processed waveforms for the vertical (left), radial (middle) and transverse (right) components are shown for the 19 stations along profile T08A (see location in Figure 27).

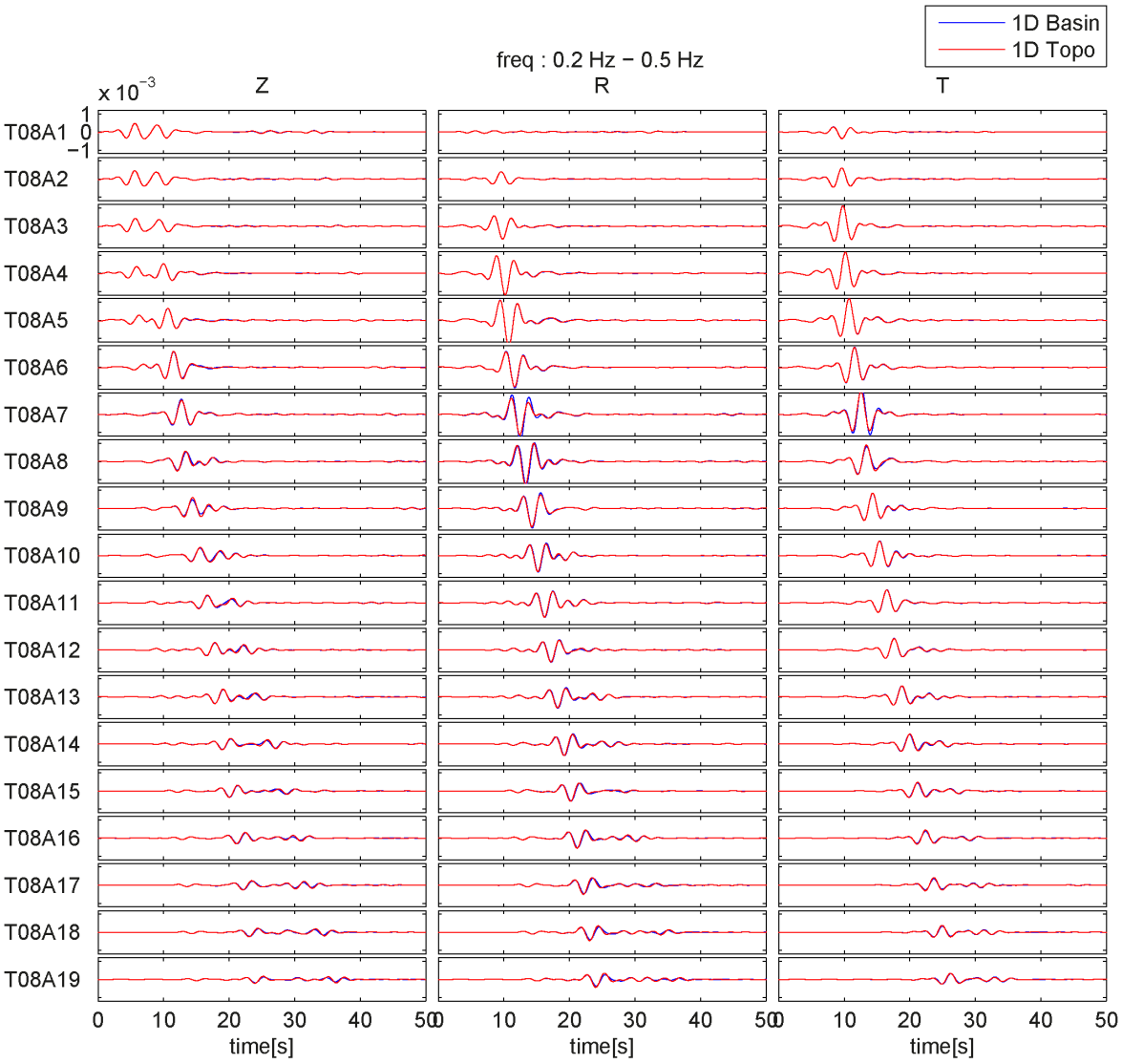

Figure S6: Comparison of synthetic seismograms computed using the 1-D topography model (red line) and the 1-D topography with basin model (blue line). The synthetic seismograms are all bandpass filtered between 0.2 and 0.5 Hz. The processed waveforms for the vertical (left), radial (middle) and transverse (right) components are shown for the 19 stations along profile T08A (see location in Figure 27).

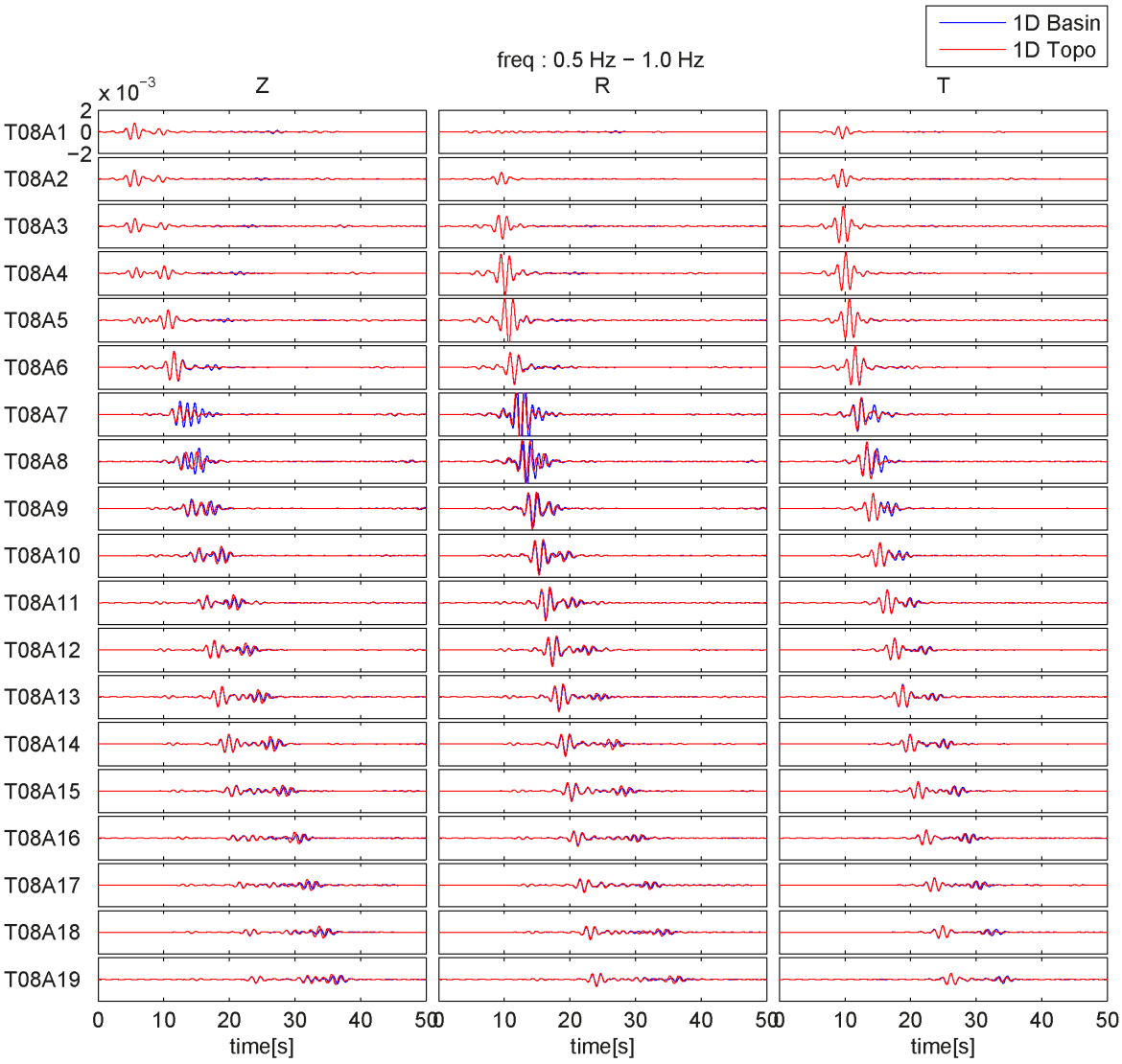

Figure S7: Comparison of synthetic seismograms computed using the 1-D topography model (red line) and the 1-D topography with basin model (blue line). The synthetic seismograms are all bandpass filtered between 0.5 and 1.0 Hz. The processed waveforms for the vertical (left), radial (middle) and transverse (right) components are shown for the 19 stations along profile T08A (see location in Figure 27).

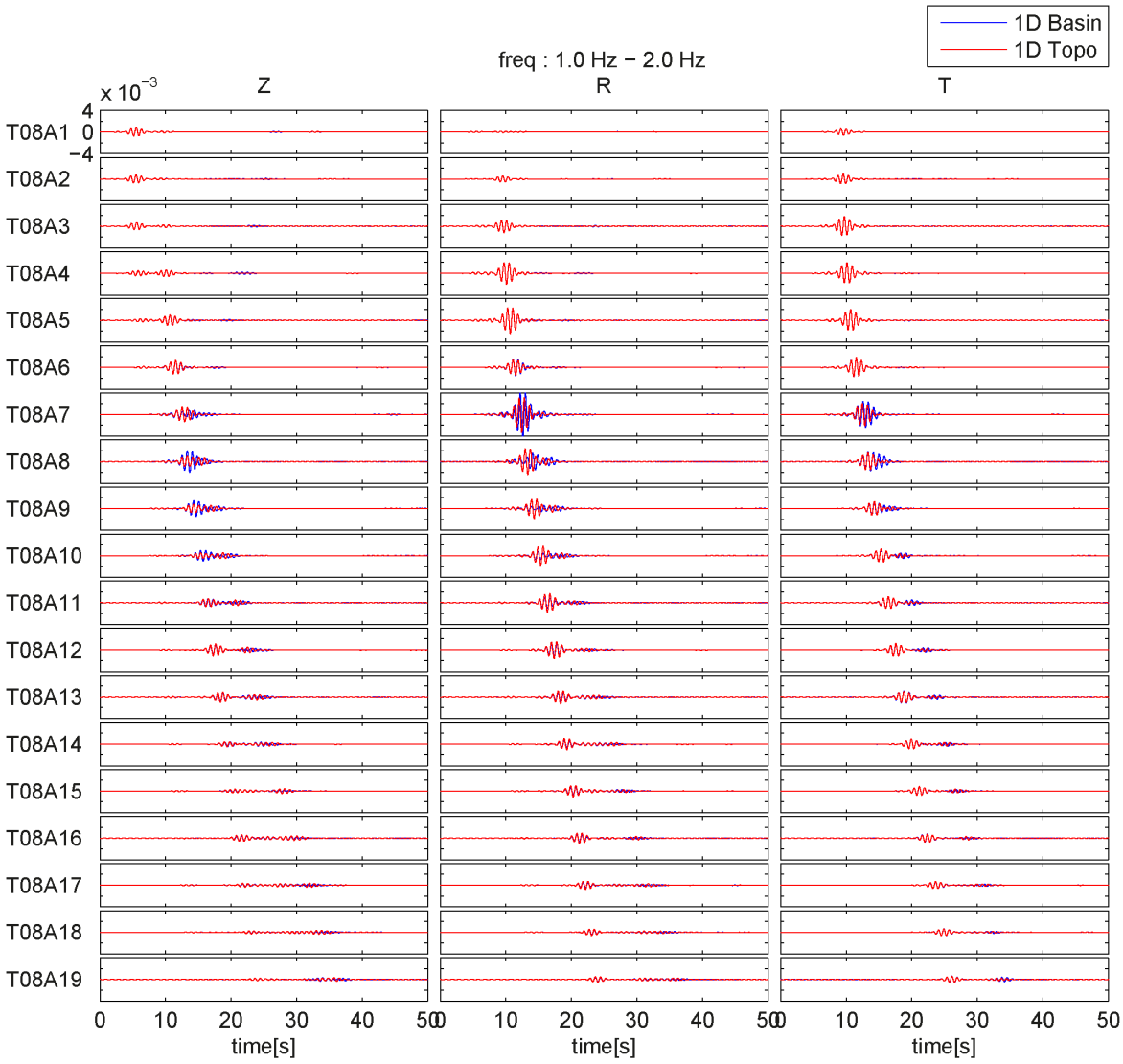

Figure S8: Comparison of synthetic seismograms computed using the 1-D topography model (red line) and the 1-D topography with basin model (blue line). The synthetic seismograms are all bandpass filtered between 1.0 and 2.0 Hz. The processed waveforms for the vertical (left), radial (middle) and transverse (right) components are shown for the 19 stations along profile T08A (see location in Figure 27).

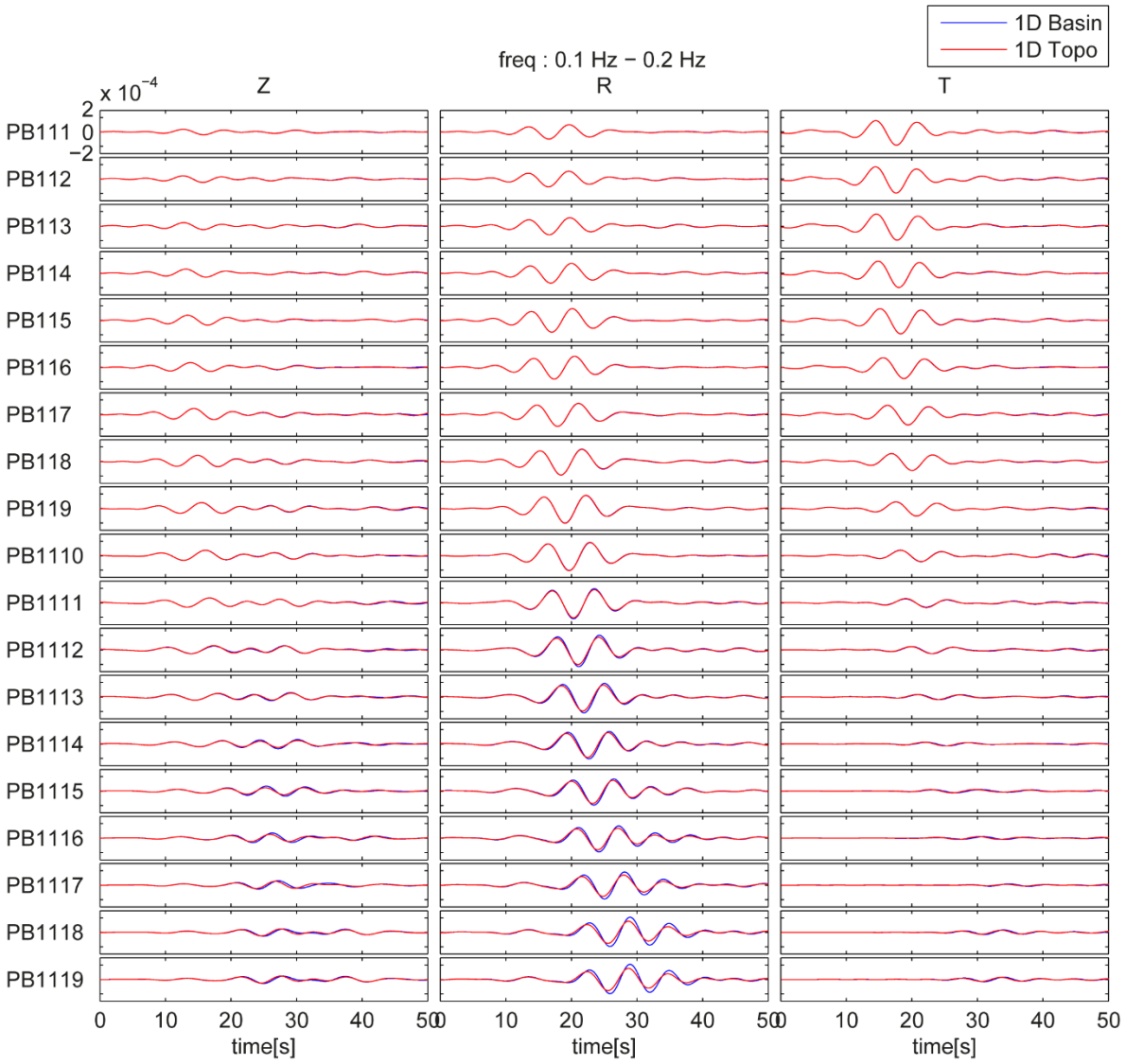

Figure S9: Comparison of synthetic seismograms computed using the 1-D topography model (red line) and the 1-D topography with basin model (blue line). The synthetic seismograms are all bandpass filtered between 0.1 and 0.2 Hz. The processed waveforms for the vertical (left), radial (middle) and transverse (right) components are shown for the 19 stations along profile PB11 (see location in Figure 27).

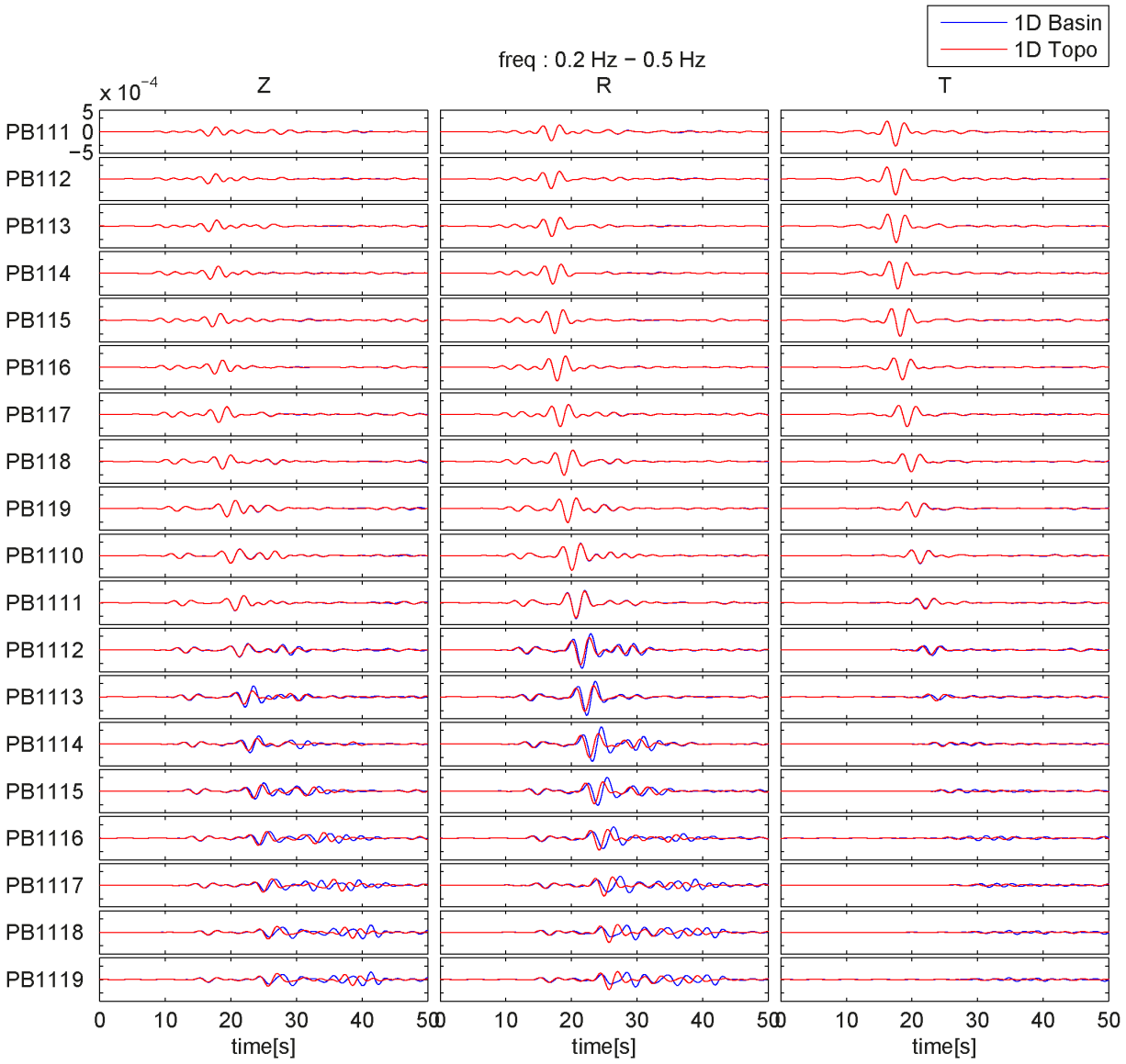

Figure S10: Comparison of synthetic seismograms computed using the 1-D topography model (red line) and the 1-D topography with basin model (blue line). The synthetic seismograms are all bandpass filtered between 0.2 and 0.5 Hz. The processed waveforms for the vertical (left), radial (middle) and transverse (right) components are shown for the 19 stations along profile PB11 (see location in Figure 27).

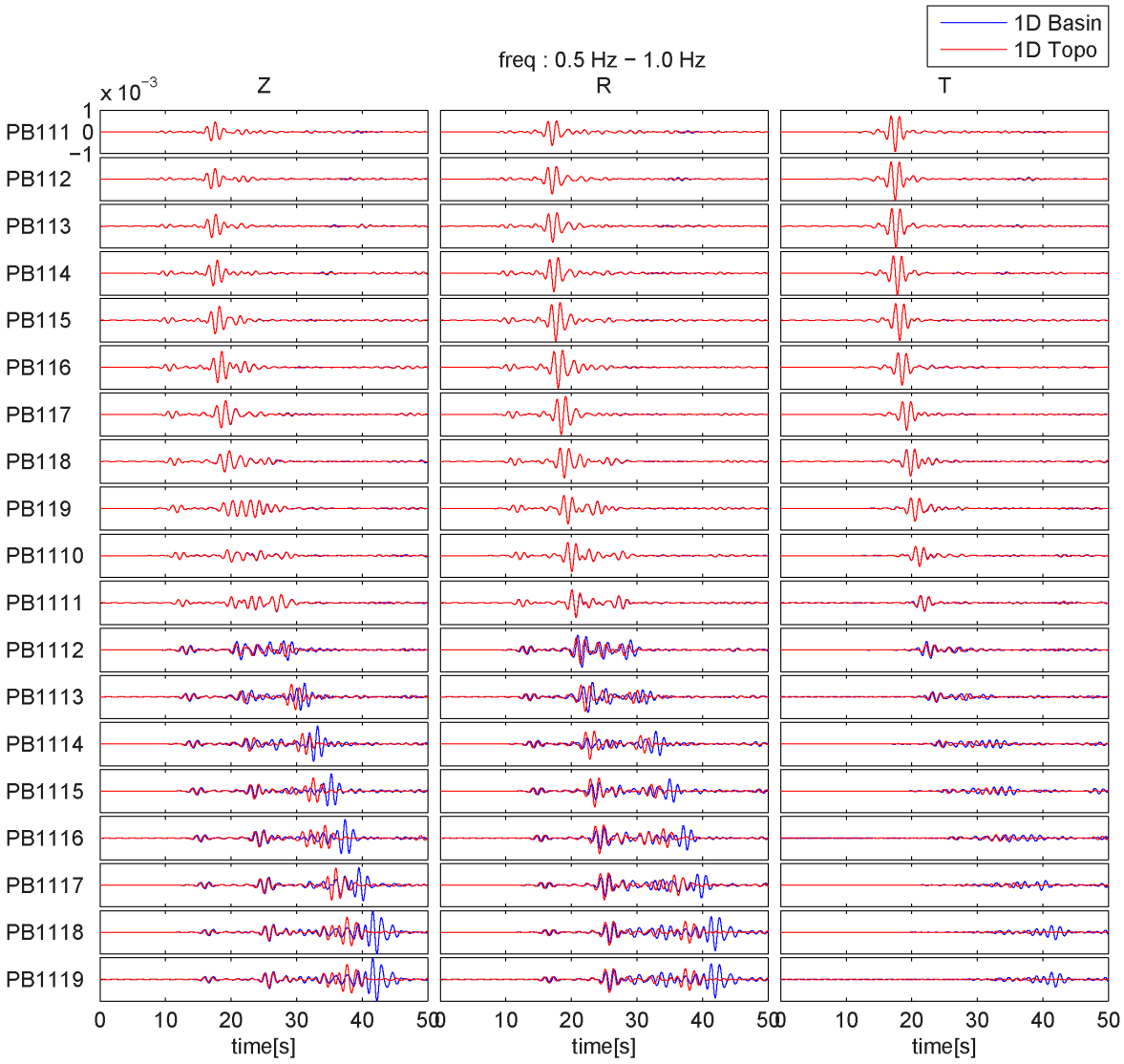

Figure S11: Comparison of synthetic seismograms computed using the 1-D topography model (red line) and the 1-D topography with basin model (blue line). The synthetic seismograms are all bandpass filtered between 0.5 and 1.0 Hz. The processed waveforms for the vertical (left), radial (middle) and transverse (right) components are shown for the 19 stations along profile PB11 (see location in Figure 27).

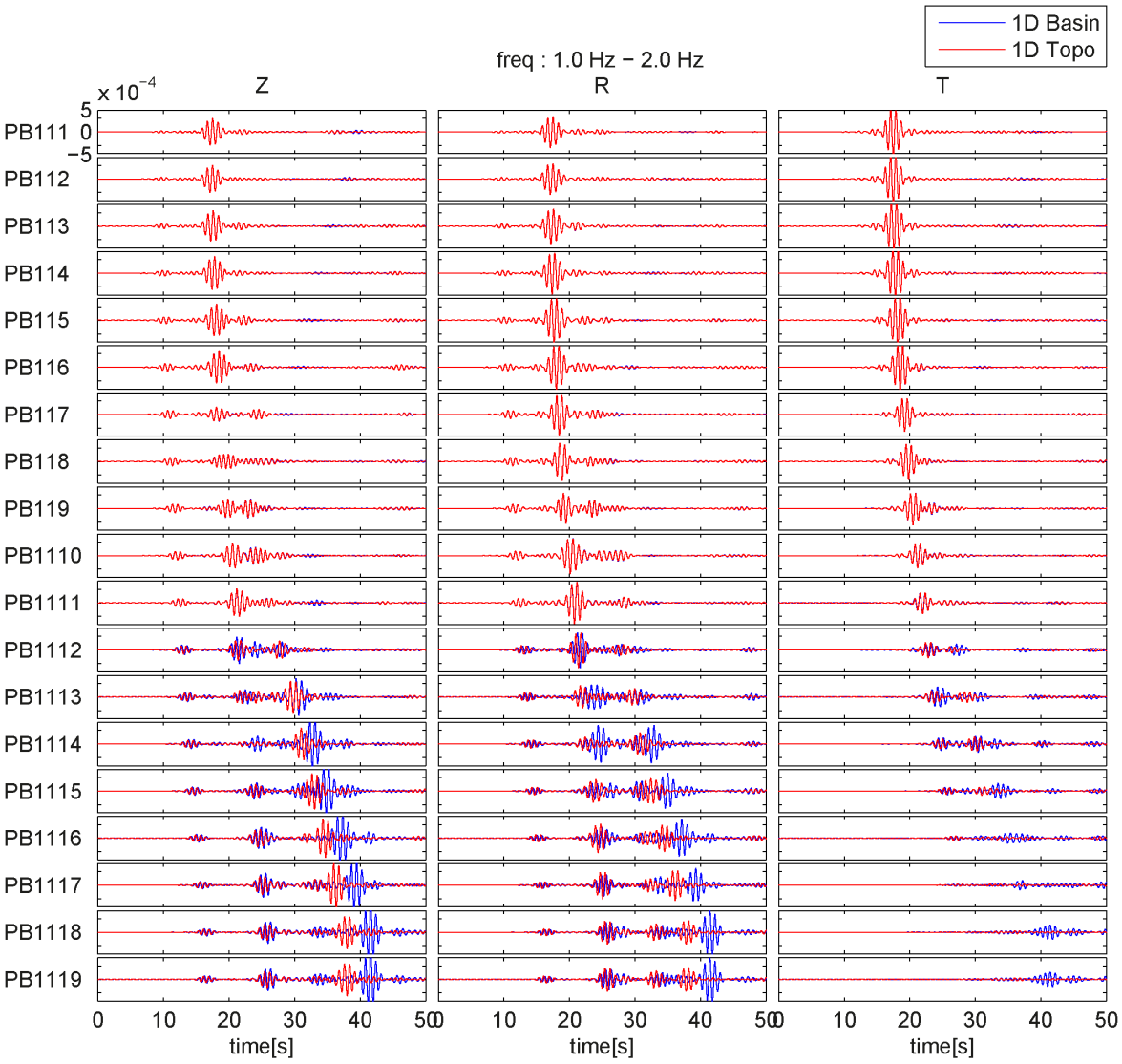

Figure S12: Comparison of synthetic seismograms computed using the 1-D topography model (red line) and the 1-D topography with basin model (blue line). The synthetic seismograms are all bandpass filtered between 1.0 and 2.0 Hz. The processed waveforms for the vertical (left), radial (middle) and transverse (right) components are shown for the 19 stations along profile PB11 (see location in Figure 27).

APPENDIX 3: 2-D VELOCITY MODEL

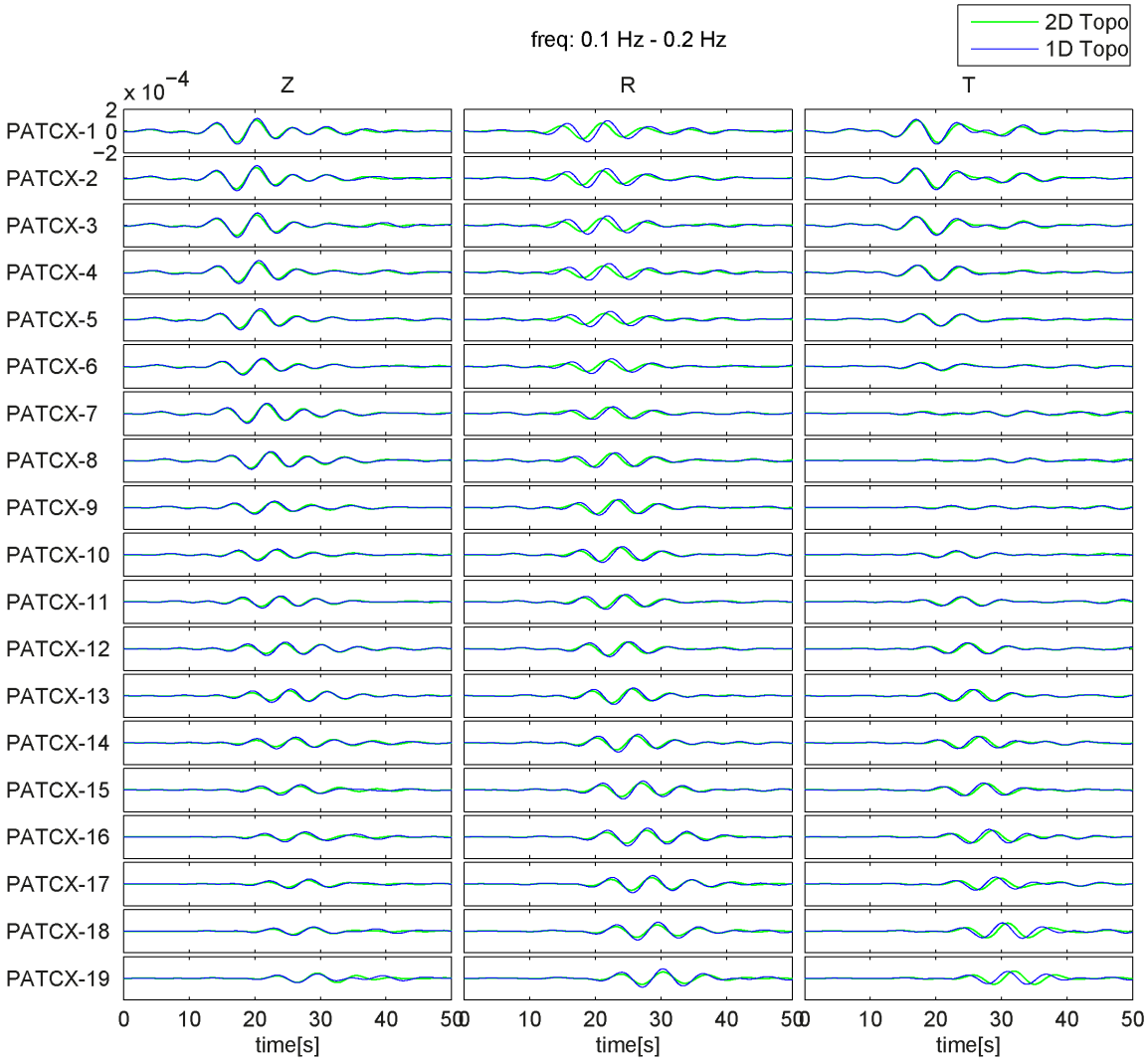

Figure S13: Comparison of synthetic seismograms computed using the 1-D topography model (blue line) and the 2D topography model (blue line). The synthetic seismograms are all bandpass filtered between 0.1 Hz and 0.2 Hz. The processed waveforms for the vertical (left), radial (middle) and transverse (right) components are shown for the 19 stations along profile PATCX (see location in Figure 27).

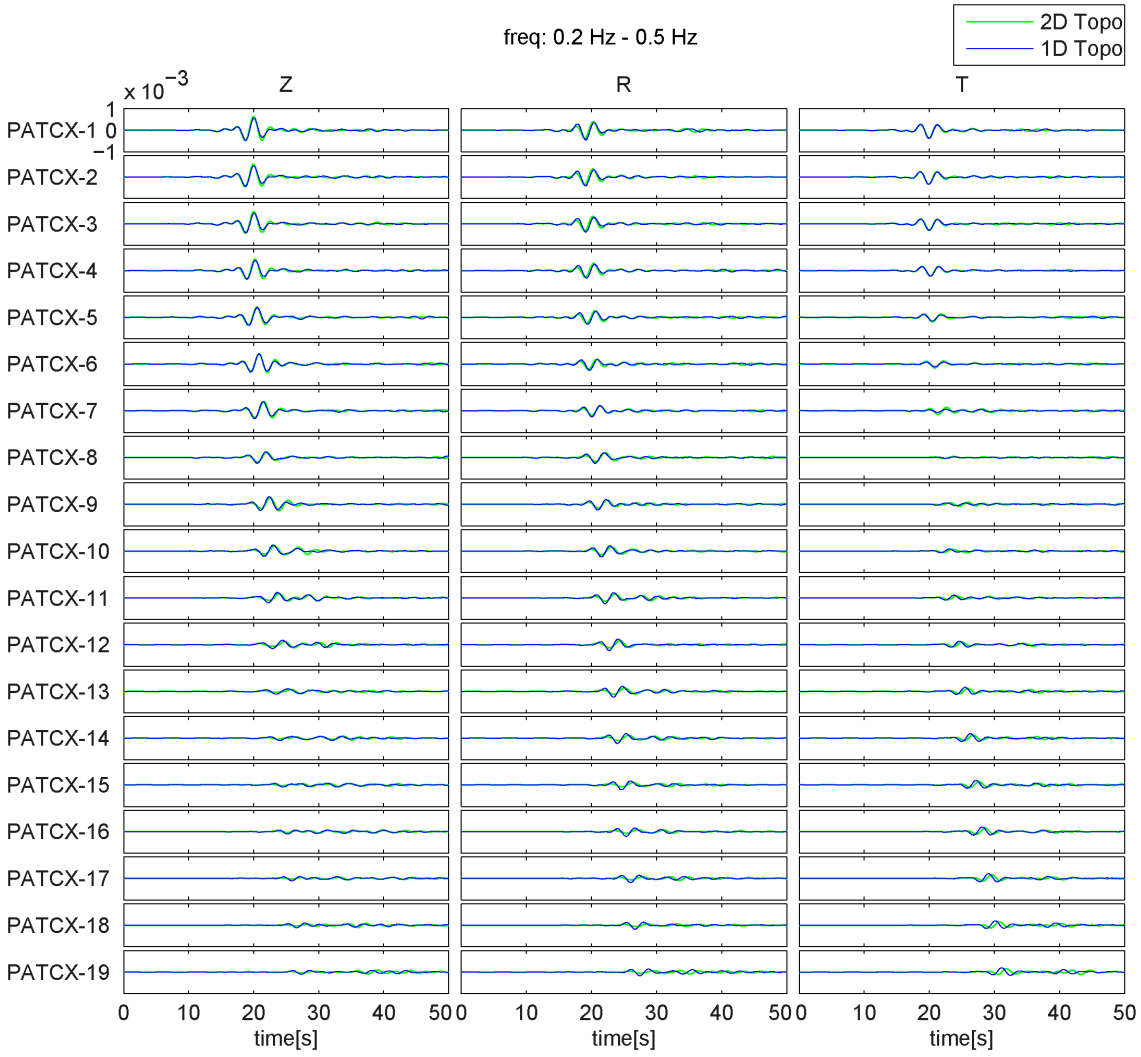

Figure S14: Comparison of synthetic seismograms computed using the 1-D topography model (blue line) and the 2D topography model (blue line). The synthetic seismograms are all bandpass filtered between 0.2 Hz and 0.5 Hz. The processed waveforms for the vertical (left), radial (middle) and transverse (right) components are shown for the 19 stations along profile PATCX (see location in Figure 27).

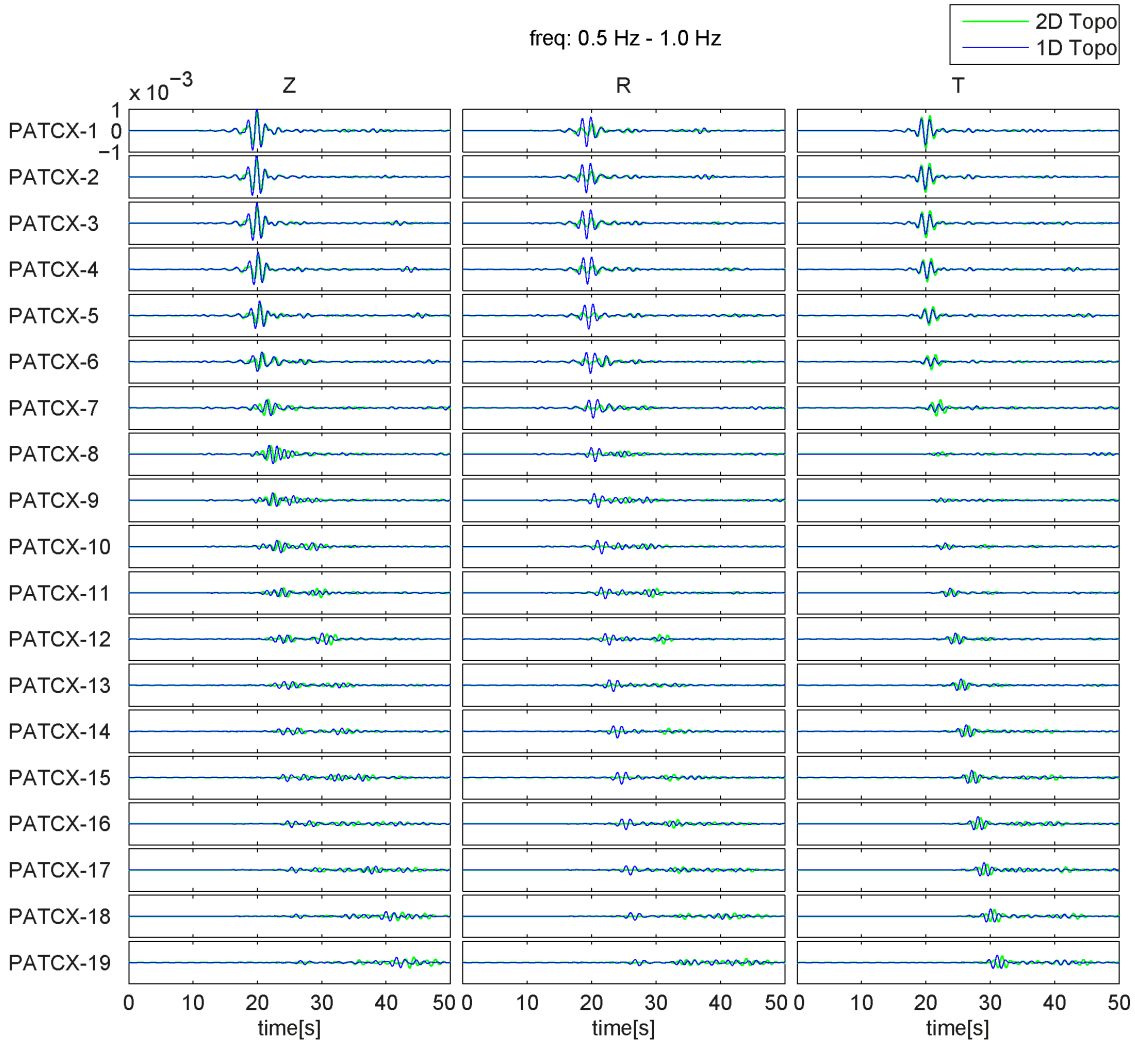

Figure S15: Comparison of synthetic seismograms computed using the 1-D topography model (blue line) and the 2D topography model (blue line). The synthetic seismograms are all bandpass filtered between 0.5 Hz and 1.0 Hz. The processed waveforms for the vertical (left), radial (middle) and transverse (right) components are shown for the 19 stations along profile PATCX (see location in Figure 27).

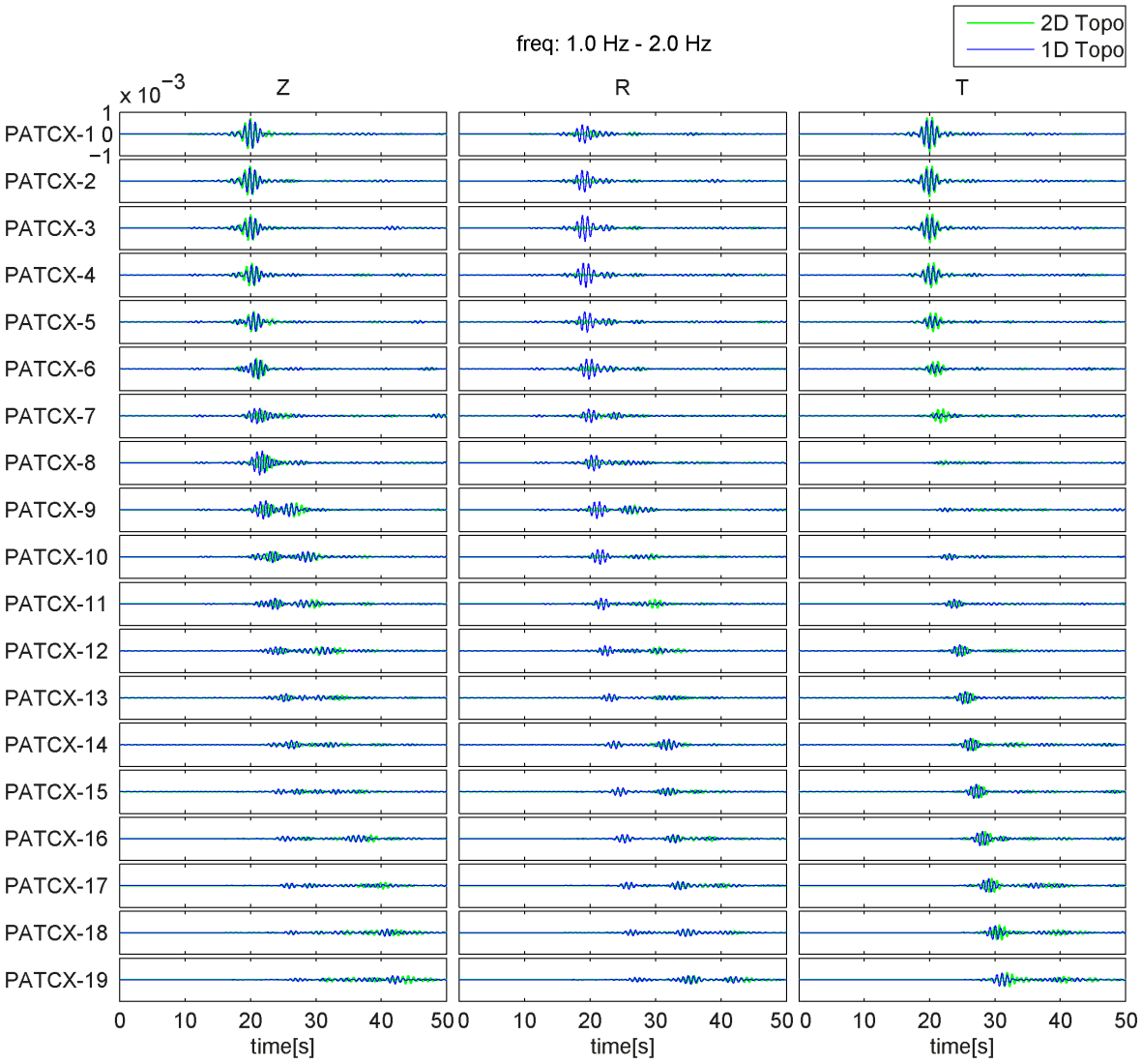

Figure S16: Comparison of synthetic seismograms computed using the 1-D topography model (blue line) and the 2D topography model (blue line). The synthetic seismograms are all bandpass filtered between 1.0 Hz and 2.0 Hz. The processed waveforms for the vertical (left), radial (middle) and transverse (right) components are shown for the 19 stations along profile PATCX (see location in Figure 27).

APPENDIX 4: COMPARISON WITH REAL DATA

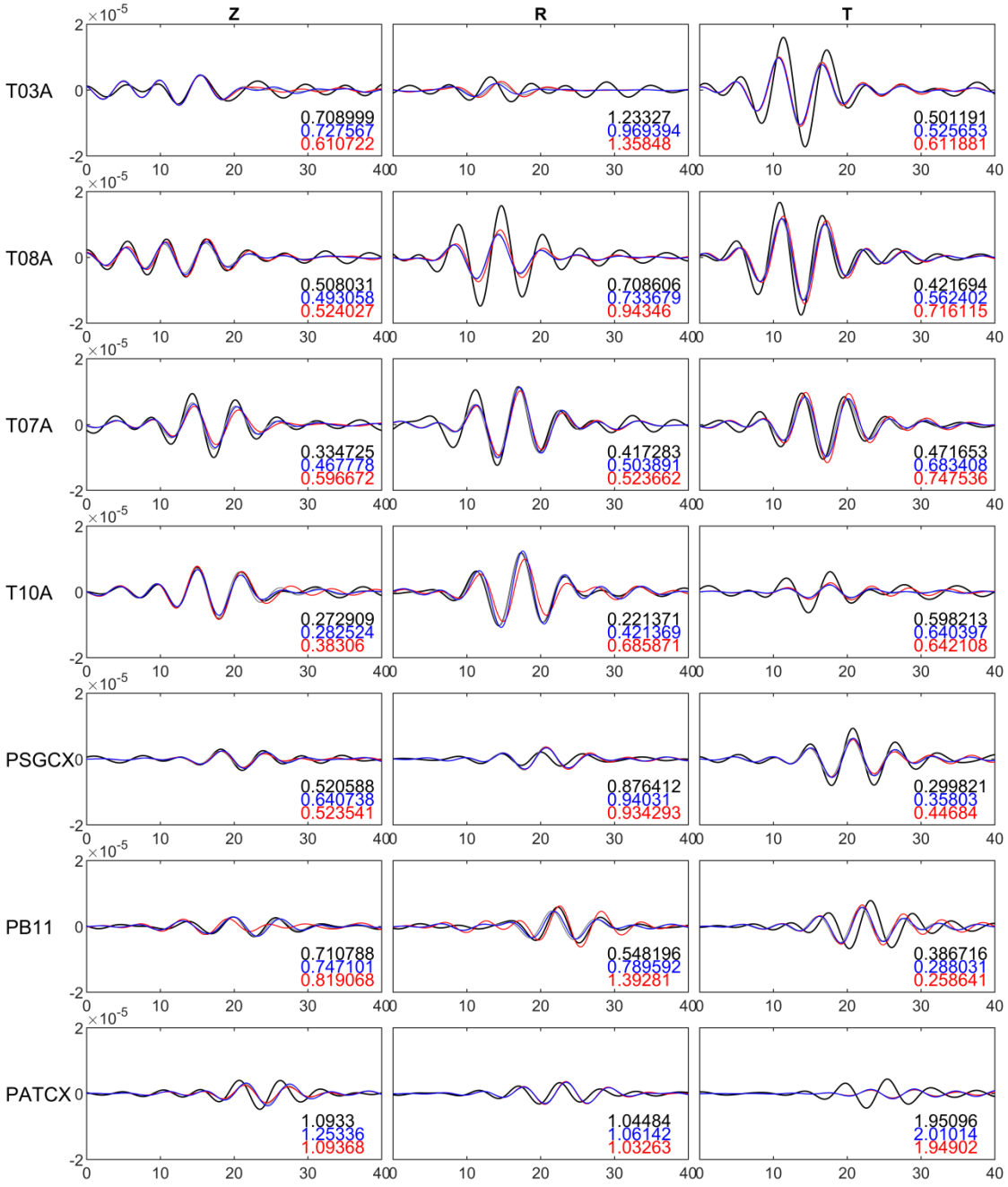

Figure S17: Comparison of real data (black traces) for the 02 April 2014 Mw 4.5 earthquake and synthetic seismograms for this earthquake computed using the 1-D flat model (gray traces), 1-D model with topography (blue traces), and 1-D model with topography and basins (red lines). Synthetic seismograms are double-differentiated to obtain acceleration (in m/s^2) and are all bandpass filtered between 0.1 and 0.2 Hz. The processed waveforms for the vertical (left), radial (middle) and horizontal (right) components are shown for seven stations, whose locations are shown in Figure 27.

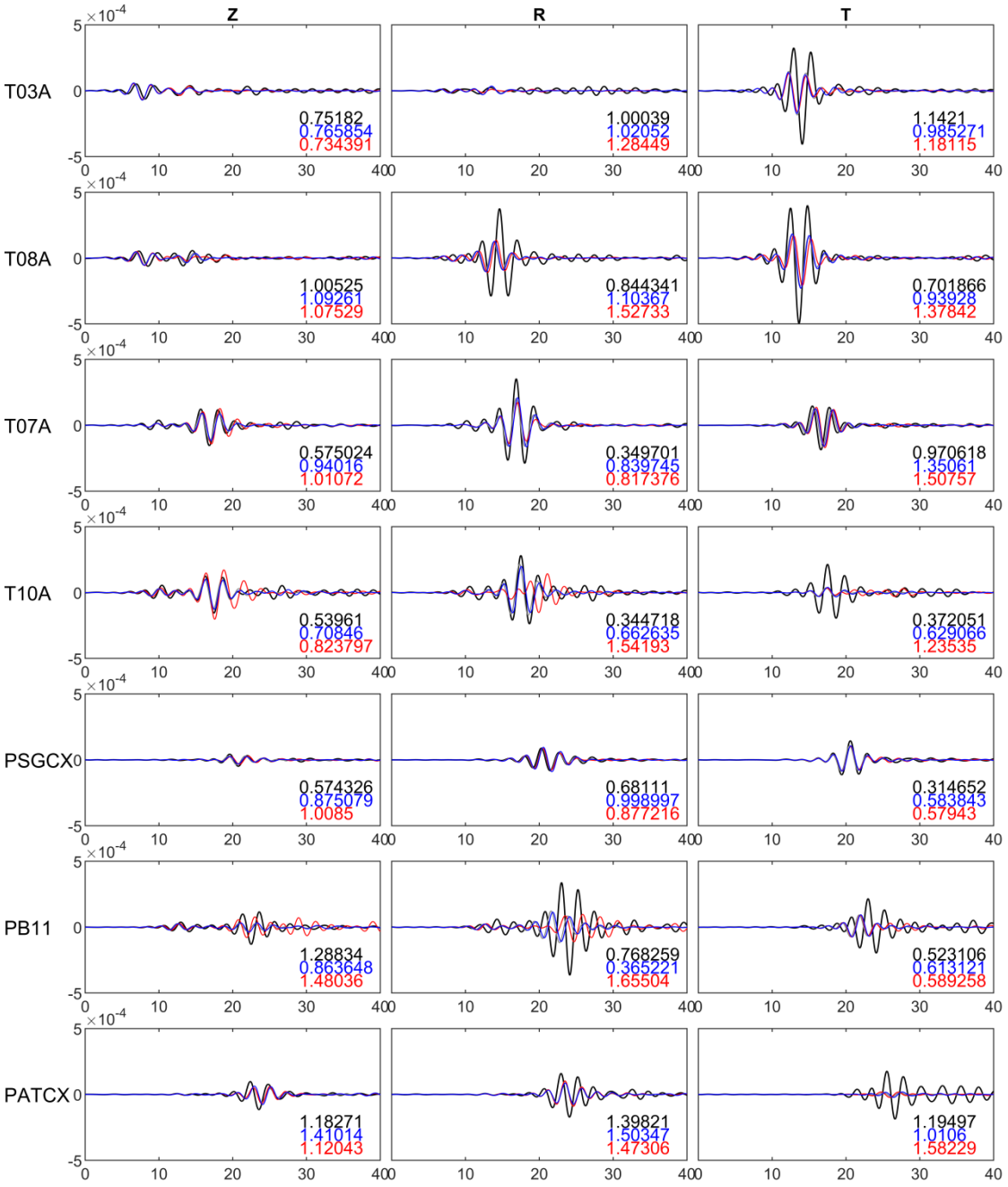

Figure S18: Comparison of real data (black traces) for the 02 April 2014 Mw 4.5 earthquake and synthetic seismograms for this earthquake computed using the 1-D flat model (gray traces), 1-D model with topography (blue traces), and 1-D model with topography and basins (red lines). Synthetic seismograms are double-differentiated to obtain acceleration (in m/s^2) and are all bandpass filtered between 0.2 and 0.5 Hz. The processed waveforms for the vertical (left), radial (middle) and horizontal (right) components are shown for seven stations, whose locations are shown in Figure 27.

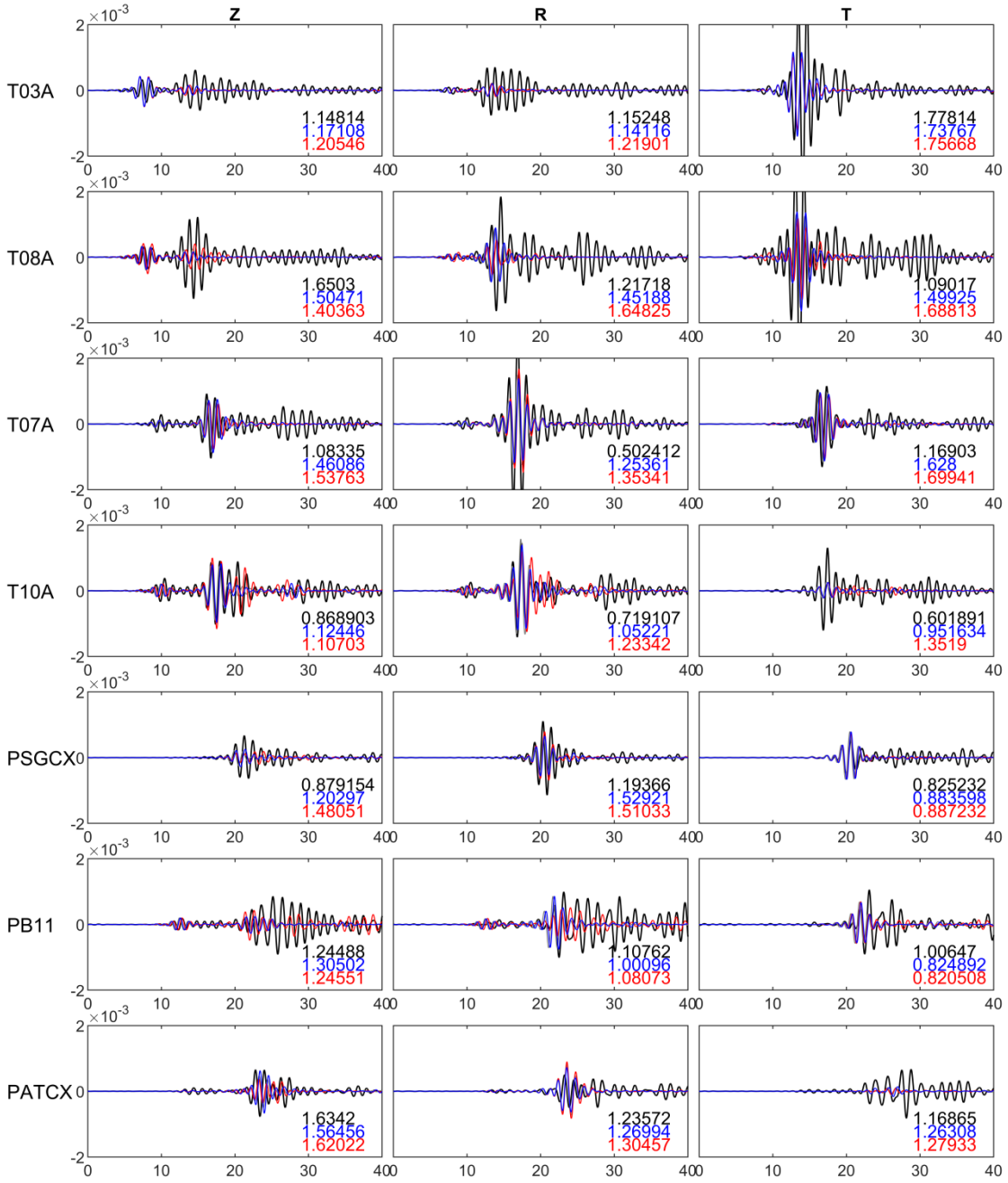

Figure S19: Comparison of real data (black traces) for the 02 April 2014 Mw 4.5 earthquake and synthetic seismograms for this earthquake computed using the 1-D flat model (gray traces), 1-D model with topography (blue traces), and 1-D model with topography and basins (red lines). Synthetic seismograms are double-differentiated to obtain acceleration (in m/s^2) and are all bandpass filtered between 0.5 and 1.0 Hz. The processed waveforms for the vertical (left), radial (middle) and horizontal (right) components are shown for seven stations, whose locations are shown in Figure 27.

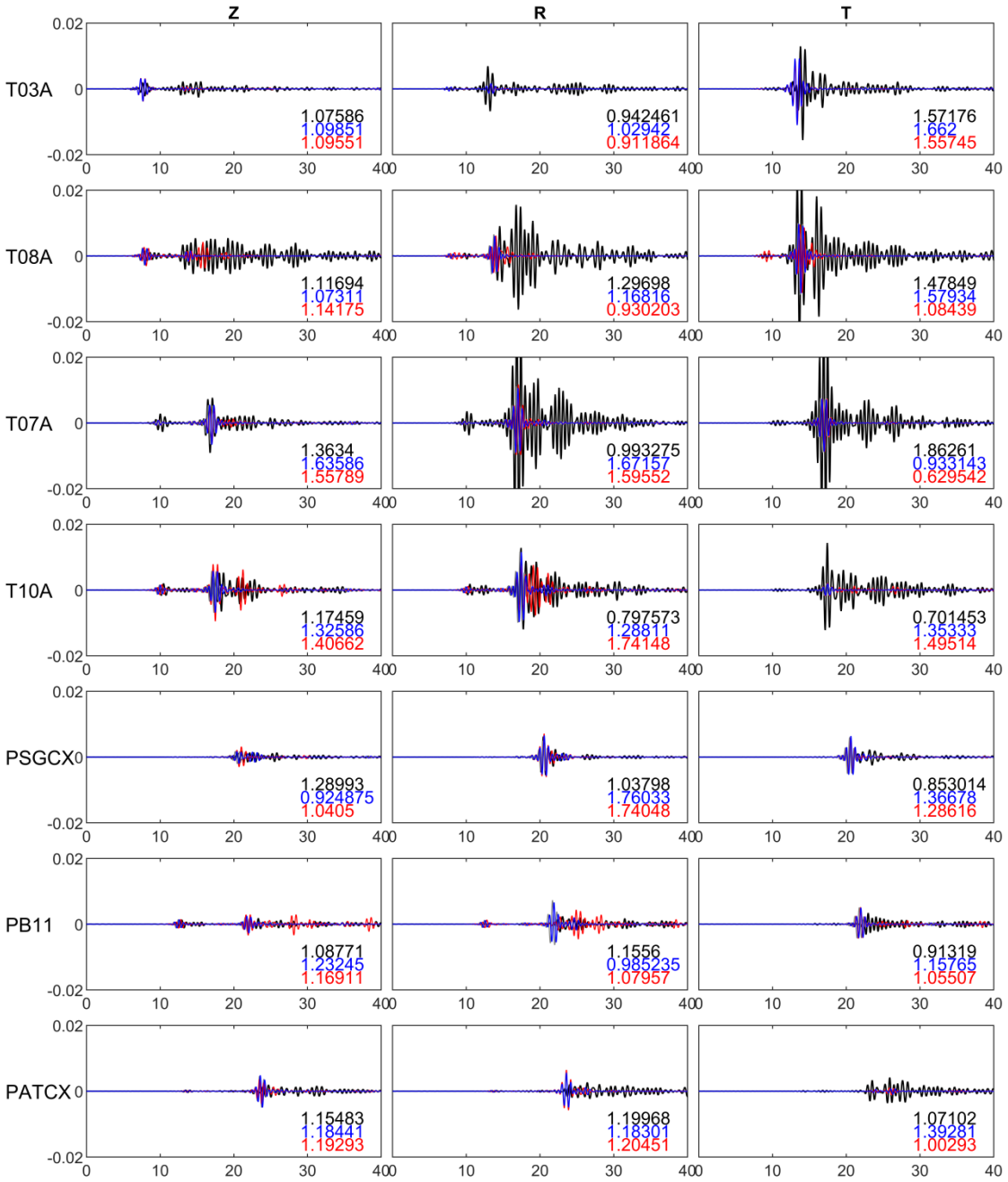

Figure S20: Comparison of real data (black traces) for the 02 April 2014 Mw 4.5 earthquake and synthetic seismograms for this earthquake computed using the 1-D flat model (gray traces), 1-D model with topography (blue traces), and 1-D model with topography and basins (red lines). Synthetic seismograms are double-differentiated to obtain acceleration (in m/s2) and are all bandpass filtered between 1.0 and 2.0 Hz. The processed waveforms for the vertical (left), radial (middle) and horizontal (right) components are shown for seven stations, whose locations are shown in Figure 27.

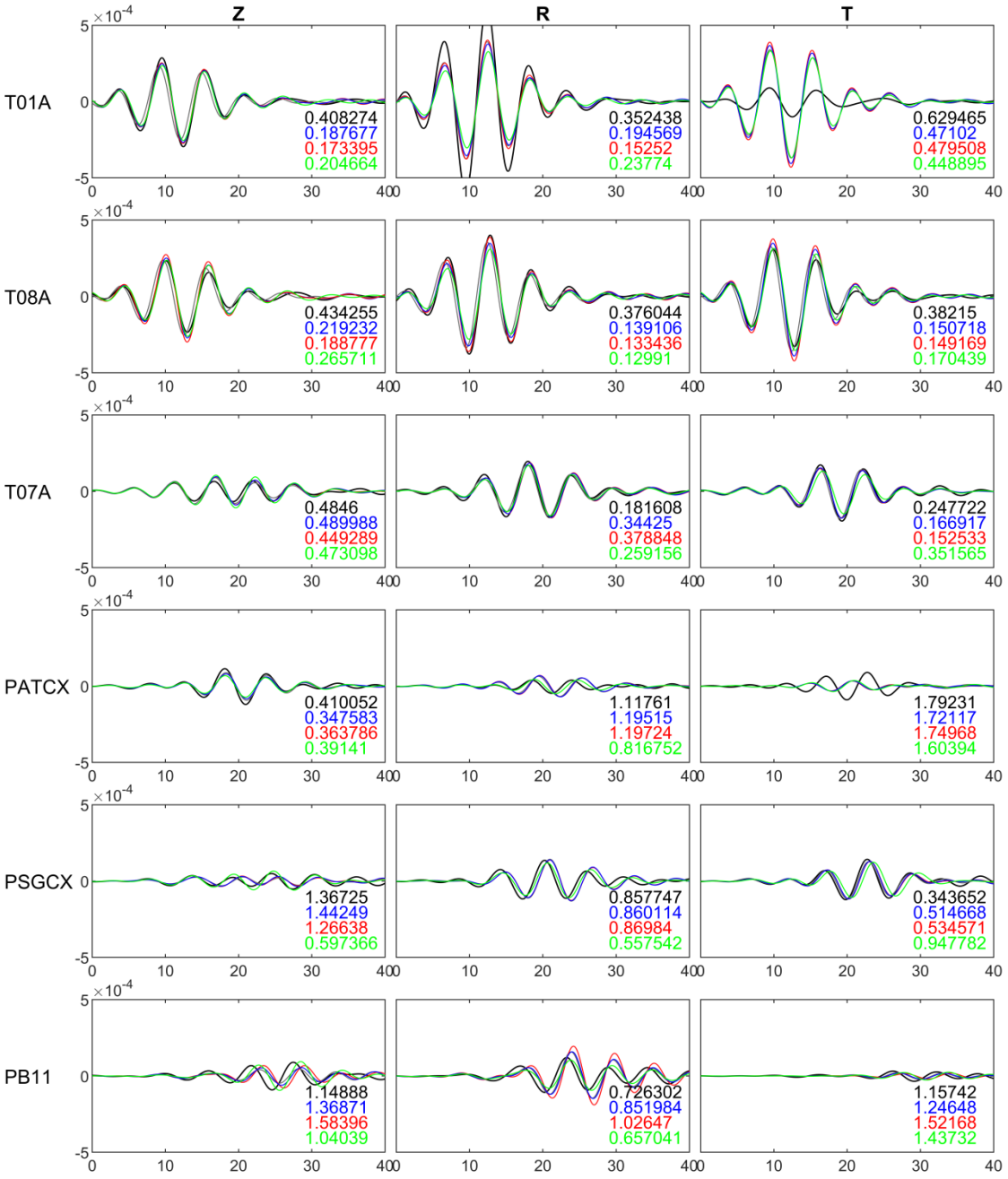

Figure S21: Comparison of real data (black traces) for the 13 July 2014 Mw 5.4 earthquake and synthetic seismograms for this earthquake computed using the 2D model with topography (green traces), 1-D model with topography (blue traces), and 1-D model with topography and basins (red lines). Synthetic seismograms are double-differentiated to obtain acceleration (in m/s^2) and are all bandpass filtered between 0.1 and 0.2 Hz. The processed waveforms for the vertical (left), radial (middle) and horizontal (right) components are shown for seven stations, whose locations are shown in Figure 27.

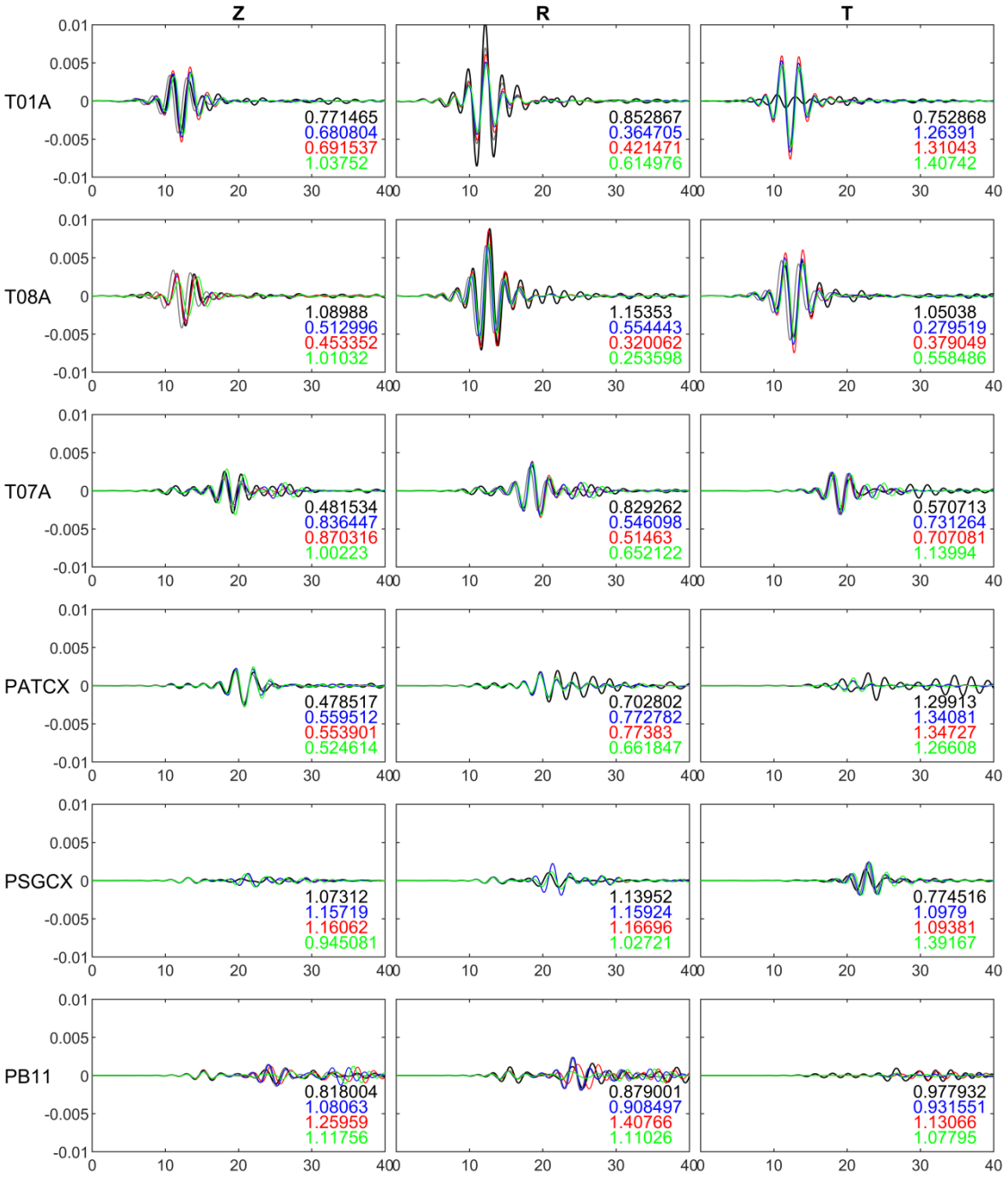

Figure S22: Comparison of real data (black traces) for the 13 July 2014 Mw 5.4 earthquake and synthetic seismograms for this earthquake computed using the 2D model with topography (green traces), 1-D model with topography (blue traces), and 1-D model with topography and basins (red lines). Synthetic seismograms are double-differentiated to obtain acceleration (in m/s^2) and are all bandpass filtered between 0.2 and 0.5 Hz. The processed waveforms for the vertical (left), radial (middle) and horizontal (right) components are shown for seven stations, whose locations are shown in Figure 27.

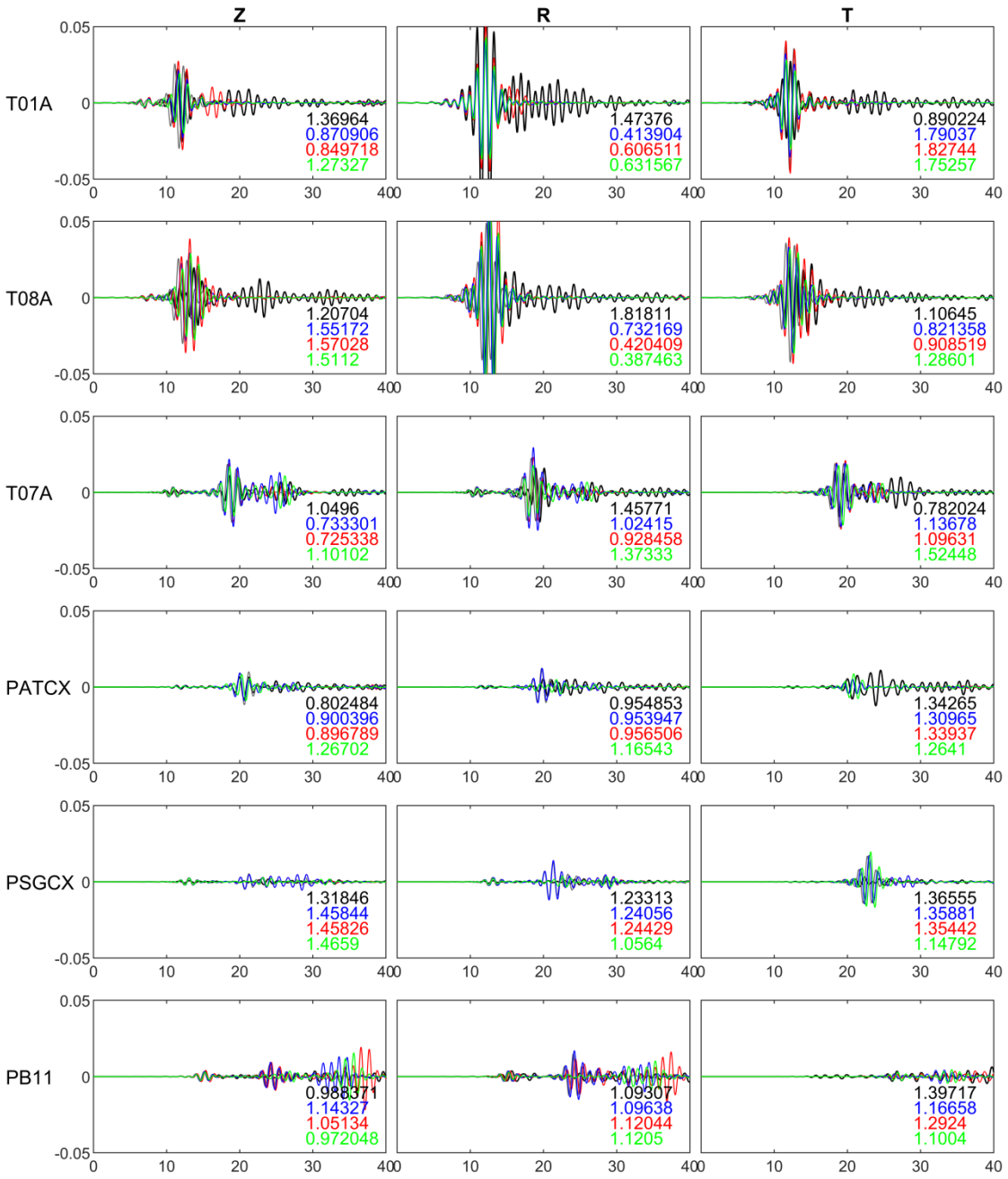

Figure S23: Comparison of real data (black traces) for the 13 July 2014 Mw 5.4 earthquake and synthetic seismograms for this earthquake computed using the 2D model with topography (green traces), 1-D model with topography (blue traces), and 1-D model with topography and basins (red lines). Synthetic seismograms are double-differentiated to obtain acceleration (in m/s^2) and are all bandpass filtered between 0.5 and 1.0 Hz. The processed waveforms for the vertical (left), radial (middle) and horizontal (right) components are shown for seven stations, whose locations are shown in Figure 27.

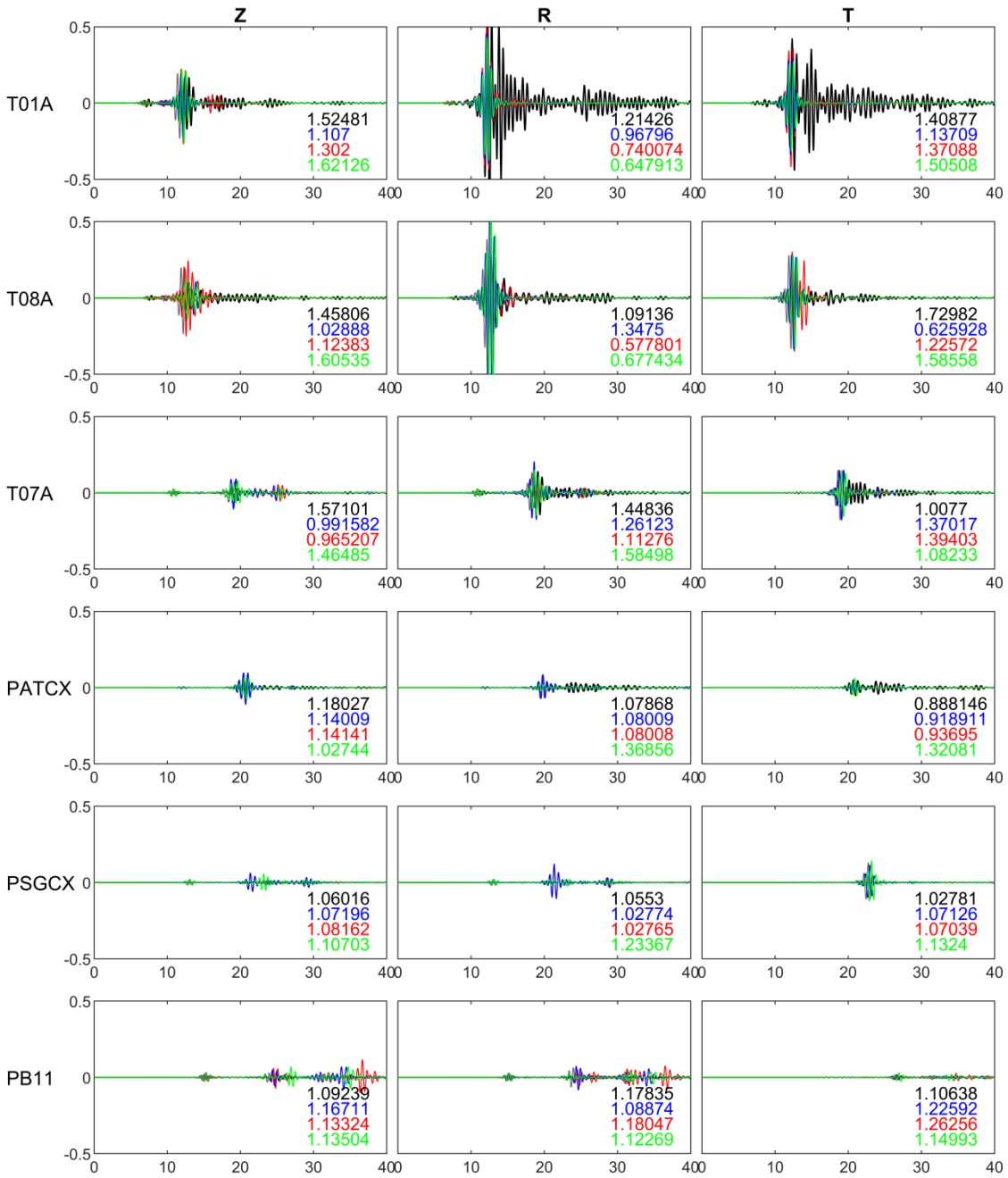

Figure S24: Comparison of real data (black traces) for the 13 July 2014 Mw 5.4 earthquake and synthetic seismograms for this earthquake computed using the 2D model with topography (green traces), 1-D model with topography (blue traces), and 1-D model with topography and basins (red lines). Synthetic seismograms are double-differentiated to obtain acceleration (in m/s^2) and are all bandpass filtered between 1.0 and 2.0 Hz. The processed waveforms for the vertical (left), radial (middle) and horizontal (right) components are shown for seven stations, whose locations are shown in Figure 27